1. AGENCY USE ONLY (Leave blank)	2. REPORT DATE	3. REPORT TYPE AND DATES COVERED
	October 1, 1993	Annual Technical 9/01/92 - 8/31/93

4. TITLE AND SUBTITLE	5. FUNDING NUMBERS
(U) Reaction Zone Models for Vortex Simulation of Turbulent Combustion	PE - 61102F PR - 2308 SA - BS G - F49620-92-J-0445

6. AUTHOR(S)

Ahmed F. Ghoniem

7. PERFORMING ORGANIZATION NAME(S) AND ADDRESS(ES)	8. PERFORMING ORGANIZATION REPORT NUMBER
Massachusetts Institute of Technology 77 Massachusetts Avenue Cambridge, MA 02139	

9. SPONSORING/MONITORING AGENCY NAME(S) AND ADDRESS(ES)	10. SPONSORING/MONITORING AGENCY REPORT NUMBER
AFOSR/NA 110 Duncan Avenue, Suite B115 Bolling AFB DC 20332-0001	

DTIC ELECTE NOV 17 1993 S A

11. SUPPLEMENTARY NOTES

12a. DISTRIBUTION/AVAILABILITY STATEMENT	12b. DISTRIBUTION CODE
Approved for public release; distribution is unlimited	

13. ABSTRACT (Maximum 200 words)

During the first year of this effort, two related issues were investigated: (1) establishing the validity of the thin flame model when used to compute flow-combustion interactions in a turbulent shear layer; (2) developing an efficient methodology to compute the unsteady strained flame structure when the flame thickness is much smaller than the flow scale. In the first effort, the transport element method was applied to compute (a) a reacting flow in which combustion proceeds according to a single-step, temperature dependent Arrhenius reaction, and (b) a mixing-limited model in which Schvab-Zeldovich variables are used to obtain the infinite speed chemistry results. The results of both computations showed that, at high Damkohler numbers, while there is a small error in the prediction of the total burning rate using the second approach, the second model accurately estimates the effect of combustion on the flow dynamics in terms of volumetric expansion and vorticity generation. Work on the second project resulted in a more efficient model to compute the flame structure under conditions of unsteady strain. The computational model is based on a series of mathematical transformations which reduce the governing equations to time-dependent reaction-diffusion equations.

14. SUBJECT TERMS	15. NUMBER OF PAGES
Turbulent Combustion, Numerical Simulation, Vortex Methods, Combustion Models.	112
	16. PRICE CODE

17. SECURITY CLASSIFICATION OF REPORT	18. SECURITY CLASSIFICATION OF THIS PAGE	19. SECURITY CLASSIFICATION OF ABSTRACT	20. LIMITATION OF ABSTRACT
Unclassified	Unclassified	Unclassified	UL

Best Available Copy

ANNUAL TECHNICAL PROGRESS REPORT
ON

REACTION ZONE MODELS FOR VORTEX SIMULATION
OF TURBULENT COMBUSTION

(AFOSR Grant # F49620-92-J-0445DEF)

Principal Investigator: Ahmed F. Ghoniem

Department of Mechanical Engineering
Massachusetts Institute of Technology
Cambridge, MA 02139

SUMMARY

During the first year of this effort, we focused on two related problems: (1) establishing the validity of the thin flame model when used to compute flow-combustion interactions in a turbulent shear layer; (2) developing an efficient methodology to compute the unsteady strained flame structure when the flame thickness is much smaller than the flow scale. In the first effort, the transport element method was applied to compute (a) a reacting flow in which combustion proceeds according to a single-step, temperature dependent Arrhenius reaction, and (b) a mixing-limited model in which Schvab-Zeldovich variables are used to obtain the infinite speed chemistry results. The results of both computations showed that, at high Damkohler numbers, while there is a small error in the prediction of the total burning rate using the second approach, the second model accurately estimates the effect of combustion on the flow dynamics in terms of volumetric expansion and vorticity generation. Thus, implementing a detailed flame sheet model using a flowfield decomposition should yield an accurate simulation for the flowfield while maintaining the overall computational requirements below what is needed in the original analysis. Work on the second project has resulted in a more efficient model to compute the flame structure under conditions of unsteady strain. The computational model is based on a series of mathematical transformations which reduce the governing equations to time-dependent reaction-diffusion equations. Model results have been used to determine the flame characteristic response time and the effect of strain-Lewis number on the burning velocity. The model is currently being extended to multistep chemistry.

Accession For

NTIS CRA&I
DTIC TAB
Unannounced
Justification

By
Distribution /

Availability Codes

Dist	Avail and/or Special
A-1	

DTIC QUALITY INSPECTED 8

93-28079

93 11 10 012

I. OBJECTIVES

The objectives of this work are:

(1) To develop, using methods of asymptotic expansion, a computational framework for the simulation of turbulent combustion phenomena by deriving equations which govern the flow and combustion in different, physically-distinct regions in the domain. This will be independent of the numerical method, or methods, used to integrate these equations and hence will have applications beyond vortex simulations;

(2) To develop subscale fundamentally based models which can be used to obtain large eddy simulations using vortex methods. Subscale models, in this case, will be obtained through the application of the renormalization group theory to the equations governing vorticity stretching and tilting on scales lower than numerically resolvable scales. The application of RNG in physical vorticity space is motivated by our solutions which show that the properties of vortex lines at the small scales follow closely the RNG predictions.

(3) To develop fundamentally based flame structure models using the equations obtained in (1) where flow combustion interactions are represented by the effect of the time-dependent stretch exerted by the outer flow on the flame structure. One important respect of these models will be the incorporation of multistep chemical kinetics algorithms to accurately capture flow combustion interactions when it is dominated by radical concentration and diffusion;

(4) To modify the transport element method; a Lagrangian scheme which we developed to simulate reacting species transport, to act as a "coupling" algorithm between the solutions obtained for the outer flow and the inner flow.

The developed methodology will be applied to study mixing and combustion in reacting shear flow at high Reynolds numbers. Effect of strong density variations, high heat release rates at elevated Damkohler numbers, and high Mach numbers will also be investigated.

II.   PERSONNEL

During the period of 1992-1993, funding was used to support the work of the following students:

(1)   Marios Soteriou who completed his Ph.D. thesis in June 1993 and stayed on as a postdoctor.

(2)   Van Luu, a Ph.D. student working on distributed reaction zone combustion model.

(3)   Constantin Petrov who completed his master's work in June 1993 and stayed on as a Ph.D. student working on the thin flame combustion model.

III.   WORK STATUS

III.1   Flow Combustion Interaction Modeling Using a Flame Sheet Representation.

A numerical methodology has been introduced to enable the study of a post-transitional spacially developing exothermically reacting shear layer over a substantial range of the governing parameters. The Transport Element Method, commonly used in the simulation of non-reacting flows is further developed to accommodate an exothermically reacting flowfield. The scheme is Lagrangian, grid-free and adaptive and solves the unaveraged, time dependent and coupled scalar transport-reaction and Navier-Stokes equations respectively, in their scalar-gradient and vorticity forms. It exploits the Shvab-Zeldovich formulation to provide solutions for both moderately fast and infinitely fast reactions. For finite reaction speeds, Arrhenius kinetics are used.

Numerical results were used in a preliminary study of the effects combustion exothermicity on both the flow and scalar fields. We found that the externally forced flowfield is substantially modified in the presence of combustion and a reduced growth is experienced mainly due to an alteration of the mechanism by which the vortical structures, which characterize the flow, interact. This, together with the decreased density within the mixing region leads to decreased efficiency of combustion.

The simpler, computationally less demanding infinite reaction speed model was found to be an effective model of the detailed finite reaction problem as long as the reactions involved in the latter are fast compared to the flow, the reaction zone is thin, and abrupt transient phenomena such as quenching are avoided. Detail of this study are presented in Appendix I of this report.

III.2   Model of an Unsteady Strained Flame

The transient response of a flame to an unsteady strain rate was analyzed using a series of mathematical transformations. Initially, the flame was located in the stagnation plane. At time $t=0$ the unsteady strain rate was applied. Two basic patterns of the strain rate are considered: a step function, and a sinusoidal wave. The flame response was characterized by two parameters: (1) the burning velocity and, (2) the flame location. The influence of the Lewis number and the strain rate on these two parameters and on the relaxation time was investigated. For unity Lewis number, and within the range of compressive strains characteristic for a turbulent jet flow (200 - 500 1/sec), the shapes of the temperature and mass fraction profiles remain almost unchanged. This leads to a burning velocity which is only slightly dependent on the strain rate. In the case of non-unity Lewis number the profiles are significantly altered even by relatively weak strain rates. This happens due to the interaction of unbalanced heat and concentration diffusion and convection. The changes in the profiles produce significant variation in the burning velocity. Some analytical results are obtained for the relaxation time of flame as a function of the strain rate and thermo-chemical parameters. The analytical derivations are based on the application of the integral approach in the transformed domain. In order to investigate the receptivity characteristics of flame, the periodic strain rate is applied. Over a wide range of frequencies, flame demonstrates periodic response. The average value of the burning velocity is very close to the burning velocity of a flame under the average strain; phase shift between the burning velocity and strain rate fluctuations is approximately constant and equal to -1.3π. This pattern is violated only when the period of the strain rate oscillations is much lower than the

diffusion time scale. The analysis of the flame response suggests that the steady state assumption can be used with a reasonable accuracy in a flamelet modeling, although the phase shift should be taken into account. Extinction strain rate which we define as the strain rate when the steady state flame location crosses the stagnation plane for the first time, is an exponential function of the heat release. This suggests that, in order to get adequate values of the extinction strain using a simplified chemical kinetics mechanism, one should pay particular attention to the chemical reactions which maintain the energetic balance of the system. Detail of this work is presented in Appendix II.

III.3 Stability and Numerical Analysis of Wake Flows

The linear instability of a family of inviscid, two-dimensional, variable-density shear layers and wakes is investigated. Vorticity profiles corresponding to a monotonically increasing velocity profile are first examined. A larger family of initial vorticity distributions which model the merger of two unequal vorticity layers of opposite sign is then considered. The latter is obtained by superimposing on the former a wake component, characterized by a spread, δ, and a velocity deficit, W. The initial density distribution resembles a temperature spike and is described by a thickness, σ, and a temperature ratio, T_r. The stability properties of the layers are interpreted in terms of a four-dimensional parameter space (W, δ, T_r, σ). The non-linear evolution of the flowfield is illustrated using the transport element method.

Flowfield stability exhibits strong sensitivity to the details of the density distribution. In the absence of the wake component, the stability properties of the heated layer are divided into three categories according to the thickness of the density profile, σ, and the vorticity thickness, δ_w. For $\sigma >> \delta_w$, instability of the Kelvin-Helmholtz mode in a uniform-density flow is recovered. When $\sigma \sim \sigma_w$, the shear layer mode is inhibited; while this trend persists for $\sigma < \delta_w$, the layer becomes characterized by the appearance of additional short-wavelength unstable modes which become dominant as σ decreases and T_r increases. Addition of a wake component is shown to alter this behavior, and to oppose the stabilizing effects of heat release. In this case, the shear layer mode always dominates the wake mode, and the presence of heated sublayer has a

5

weak effect on the instability of the vorticity layer when δ is large, but may influence the phase speed of unstable waves whenever the zones of high vorticity and high density gradient coincide. Detail of this work is presented in Appendix III.

IV. PUBLICATIONS DURING 1992-1993.

1. Ghoniem A.F., Soteriou M.C., Knio, O.M. and Cetegen, B., " Effect of Steady and Periodic Strain on Unsteady Flamelet Combustion," *24th Symposium (International) on Combustion,* pp. 223-230, The Combustion Institute, Pittsburgh, PA, 1992.*

2. Knio, O.M. and Ghoniem, A.F.. "The Three-dimensional Structure of Periodic Vorticity Layers under Non-symmetric Conditions," *J. Fluid Mech..,* 243, pp. 353-392, 1992.*

3. Knio, O.M., Shi, X. and Ghoniem, A.F., "Lagrangian Simulation of Flamelet Combustion," AIAA *31st Aerospace Sciences Meeting,* Reno, NV, January 1993.

4. Knio, Omar M. and Ghoniem, Ahmed F., "Stability Analysis of Differentially-heated Asymmetric Vorticity Layers," J.T. Beale et al. (eds), *Vortex Flows and Related Numerical Methods,* pp. 341-372. Kluwer Academic Publishers, The Netherlands, 1993.*

5. Soteriou, M.C. and Ghoniem, A.F., "Mechanism Turbulence-Combustion Interaction in a Spatially-developing Mixing Layer, *14th ICDERS,* Coimbra, Portugal, 1993.

6. Soteriou, M.C. and Ghoniem, A.F., "Vortex-transport Element Simulation of the Exothermically Reacting Spacially Developing Shear Layer," *Second U.S. National Congress on Computational Mechanics,* Washington, D.C., August 1993.

7. Petrov, Constantin and Ghoniem, Ahmed F., "Unsteady Thin Flames as Models of Turbulence-Combustion Interactions," accepted for presentation at the AIAA *32nd Aerospace Sciences Meeting,* Reno, NV, January 1994.

8. Soteriou, Marios C. and Ghoniem, Ahmed F., "Numerical Study of the Mechanisms of Shear Flow Modification by Combustion Related Density Variation," accepted for presentation at the AIAA *32nd Aerospace Sciences Meeting,* Reno, NV, January 1994.

V.   SEMINARS AND LECTURES DELIVERED DURING 1992-1993

1.   Egyptian Environmental Affairs, (by invitation) Cairo, Egypt, 1992

2.   National Institute of Standards and Technology, Gaithersburg, MD, 1992

3.   University of Massachusetts, Amherst, MA, 1993.

4.   Princeton University, Princeton, NJ, 1993

5.   Ford Motor Company, Dearborn, MI, 1993

6.   AIAA Professional Course on Combustion Modeling in Gas Turbine, Ramjet and Scramjet, Monterey, CA, 1993

---

* References marked with * are supplied in the form of reprints under separate covers.

VI. INTERACTIONS WITH INDUSTRIAL AND GOVERNMENT LABORATOR. DURING 1992-1993.

1. General Electric Corporate Research and Development Center, with Dr. Sanjay Correa.

2. Altex Technologies, Los Gatos (small R&D Business), with Drs. M. Namazian and J. Kelly.

3. Ford Motor Company, with Dr. Chris Kent.

4. Advanced Mechanical Technology, Inc. (R&D Business), Newton, MA, with Mr. Sergei Brussovanski.

5. Physical Sciences, Inc., Andover, MA, with Dr. Terry Parker.

6. Tecogen Inc., Waltham, MA with Dr. Kailash Shukla

7. Northwest Fuel Development, Portland, OR, with Dr. Peet Soot.

APPENDIX I

APPENDIX I

VORTEX-TRANSPORT ELEMENT SIMULATION OF THE EXOTHERMICALLY REACTING SPACIALLY DEVELOPING SHEAR LAYER

Marios C. Soteriou and Ahmed F. Ghoniem

Department of Mechanical Engineering
Massachusetts Institute of Technology
Cambridge, MA 02139

ABSTRACT

A numerical methodology is introduced which enables the study of a post-transitional spacially developing exothermically reacting shear layer over a substantial range of the governing parameters. The Vortex-Transport Element Method, commonly used in the simulation of non-reacting flows is further developed to accommodate an exothermically reacting flowfield. The scheme is Lagrangian, grid-free and adaptive and solves the unaveraged, time dependent and coupled scalar transport-reaction and Navier-Stokes equations respectively, in their scalar-gradient and vorticity forms. It exploits the Shvab-Zeldovich formulation to provide solutions for both moderately fast and infinitely fast reactions. For finite reaction speeds, Arrhenius kinetics are used.

Numerical results are used in a preliminary study of the effects combustion exothermicity on both the flow and scalar fields. It is seen that the externally forced flowfield is substantially modified in the presence of combustion and a reduced growth is experienced mainly due to an alteration of the mechanism by which the vortical structures, which characterize the flow, interact. This, together with the decreased density within the mixing region leads to decreased efficiency of combustion.

The simpler, computationally less demanding infinite reaction speed model is found to be an effective model of the detailed finite reaction problem as long as the reactions involved in the latter are fast compared to the flow, the reaction zone is thin, and abrupt transient phenomena such as quenching are avoided.

I. INTRODUCTION

Post-transitional exothermically reacting shear layers are commonly present in many combustion systems. The flow, which is a manifestation of the growth of the instability of the shear region between two reacting fluids at different velocities represents an important mechanism by which reactants mix and burn, in such systems. Experimental [e.g.1] studies indicate that the vortical structures which dominate non-reacting shear layers persist in their reacting counterparts despite the substantial effects of the combusting field on the flowfield. These structures are found to coincide with the region where product exists, thus exemplifying their fundamental importance to the combustion process. Combustion, in turn, strongly influences their evolution and interactions via the release of chemical energy and the resulting variable density field.

The effects of the combustion heat release and of the related variable density field on the flowfield have been the subject of significant interest recently. Even in the absence of reaction the presence of a variable density field substantially alters the properties of the flow, modifying the growth of the mixing region the entrainment from the free streams and the unsteady evolution of the eddies [2]. Experimental studies [3,4,1] have indicated that in the presence of an exothermically combusting field the shear layer growth is reduced, resulting in diminished efficiency of mixing and burning. This was initially a rather surprising finding since combustion was anticipated to increase the size of the mixing region via volumetric expansion. Numerical studies mainly restricted to the simulation of temporally evolving reacting shear layers [5-7], have, to some extend, been able to reproduce this behavior. In this work the applicability of the idealized, temporally evolving flow model, in simulating reacting shear layers is fundamentally questioned. The temporal model aims at approximating the shear layer flow via a Galilean space-time transformation: a computational domain is selected which is moving with the mean flow velocity and which describes a small section of the flowfield. This section is defined by the flow time scale in such a way as to include one or two vortical structures. The small size of the domain, as compared to that necessary in a spacial layer simulation, is the major source of the savings mentioned earlier. The problem with the use of temporal layers lies in the fact that the boundary conditions in the streamwise direction (i.e. at the inlet and exit) of the domain are not explicitly known. For this reason, artificial periodic boundary conditions are imposed. As a result the actual flow cannot be reproduced exactly from such a calculation. For example, the asymmetry imposed by the velocity ratio, which results in the tendency of the uniform density shear layer to intrude more into the slower of the two streams, cannot be captured. Additionally, the streamwise asymmetry in the shape of the vortical structures is also lost. For the reacting field, the limitations are more devastating. The periodic boundary conditions remove any spacial evolution of the combustion-related properties of material which crosses the domain in the

streamwise direction; only temporal evolution is permitted. On the other hand, the same material experiences significant flow-related evolution. This is an uncommon situation since it requires the flow speed to be higher than the combustion speed, i.e. high Karlovitz number. For a real fuel, characterized by a high Damkohler number, such a condition would unavoidably lead to quenching (termination of the reaction due to excessive flow stretch). In the temporal simulations noted above, this problem does not arise due to an additional, and apparently independent, low Damkohler number assumption. What is evident from the above discussion though, is that the applicability of temporal simulations is in fact restricted to low Damkohler number combustion and unphysical solutions would result if higher values of this parameter were to be used.

Spacially evolving shear layer numerical studies [8,9], which attempt a much more physical description of the flow, have, on the other hand, for the most part been restricted to cases where the effects of combustion on the flowfield are negligible (low combustion heat release). Such studies have been used to discern the structure of the reaction zone and the effects of the reaction speed (Damkohler number) on the relative location of the reaction zone with respect to the large structures. It was concluded that at small Damkohler number, the reaction is most intense near the center of the large eddy, while as the Damkohler number increases, the reaction zone moves outwards towards the outer edges of the eddies. It was also found that, under conditions of unity stoichiometry, a strong similarity exists between the products concentration field and the vorticity field.

In contrast, in this work a numerical methodology capable of dealing with significant combustion exothermicity is presented and implemented in the simulation of the forced, spacially developing shear layer.

II. FORMULATION

A two-dimensional, post-transitional reacting shear layer is considered. Gravitational effects are negligible. Compressibility effects are permitted under the low Mach number assumption. According to this assumption, the flow speed is much smaller than the speed of pressure wave propagation. Hence, spacial pressure variations reach equilibrium rapidly when compared to the flow timescale and, thus, for thermodynamic considerations they appear negligibly small. This can easily be seen by considering that the momentum equation for this case, reduces to the statement that spacial gradients of the thermodynamic pressure are equal to zero. But while pressure variations are small when compared to the thermodynamic pressure, they are not negligible when compared to the other forces governing fluid motion. Thus by rescaling them with the flow dynamic pressure one can ascertain their effect on the flowfield. This is expressed in the more traditional momentum equation used herein. (This distinction

between the thermodynamic and dynamic pressure in a low Mach number combusting system was initially proposed in ref.[5] where a detailed derivation of the approximate equations of motion is presented.)

While, under the low Mach number assumption, combustion has an insignificant effect on the spacial thermodynamic pressure variation, it can substantially alter this pressure in time. This is certainly true in a constant volume domain where the overall density is constant and substantial pressure changes take place as combustion heat is released and the fluid temperature is raised. In an open (infinite volume) domain, on the other hand, combustion primarily alters the fluid temperature and density resulting to approximately constant pressure. In this work the flow is partially confined (see Section IV). Nevertheless, constant pressure combustion is still assumed since in the cross-stream direction the confining walls are substantially far from the combusting region and in the streamwise direction the domain is relatively short. The validity of this assumption is further assessed from the results by comparing the streamwise dynamic pressure change of each fluid stream to the corresponding inlet dynamic pressure. Thus, in this formulation the thermodynamic pressure is treated as a constant both in space and time and hence it is absent from the non-dimensionalized equations. The pressure appearing in the momentum equation is the flow dynamic pressure.

Combustion is assumed to take place according to a single step reaction which consumes two reactants, one from each stream, to yield a single product. The chemical kinetics are of the Arrhenius type. The transport properties are constant. All species are assumed to behave as perfect gases with equal molecular weights, specific heats and mass diffusion coefficients. The Lewis number is equal to unity. Diffusion effects are assumed small (high Reynolds and Peclet number flow). This allows higher order diffusion mechanisms to be neglected. Hence, thermal diffusion (Soret effect), second order diffusion terms in the scalar equations arising from products of density and scalar gradients, and heat production due to fluid dynamical viscous dissipation, are all neglected.
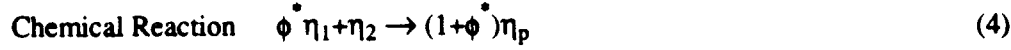
Non dimensionalization is carried out using a length scale, $\tilde{L}_o$, a velocity scale, $\tilde{U}_o$ and temperature, $\tilde{T}_o$, and density, $\tilde{\rho}_o$, scales. (The tildes indicate dimensional variables. In what follows, absence of the tilde denotes a non-dimensionalized variable). The actual values of these scales are specified in Section IV. The simultaneous use of density and temperature scales allows for the different scaling of the thermodynamic pressure as compared to that of the dynamic pressure which is scaled via the density and the velocity scales.

Under the above assumptions the non-dimensionalized governing equations are:

Continuity
$$\frac{d\rho}{dt} + \rho \, \nabla \cdot \mathbf{u} = 0 \tag{1}$$

4

Momentum $\quad \dfrac{d\mathbf{u}}{dt} = -\dfrac{\nabla p}{\rho} + \dfrac{1}{Re}\nabla^2\mathbf{u}$ (2)

Equation of State $\quad \rho\,T = 1$ (3)

Chemical Reaction $\quad \phi^*\eta_1 + \eta_2 \rightarrow (1+\phi^*)\eta_p$ (4)

Temperature-Species $\dfrac{ds_j}{dt} = \dfrac{1}{Pe}\nabla^2 s_j + Q_j\dfrac{\dot{w}}{\rho}$ (5)

with

j	1	2	3	4 (+)
s_j	T	Y_1	Y_2	Y_p
Q_j	$Q_o\phi$	$-\phi$	-1	$1+\phi$

$((+)\ Y_1 + Y_2 + Y_p = 1)$ (6)

and where $\quad \dot{w} = A_f\,\rho^2\,Y_1\,Y_2\,\exp(-\dfrac{T_a}{T})$ (7)

$\mathbf{u} = (u,v)$ is the velocity vector in a right-handed Cartesian coordinate system $\mathbf{x} = (x,y)$ and t is the time. $\nabla = \left(\dfrac{\partial}{\partial x},\dfrac{\partial}{\partial y}\right)$ is the gradient operator and $\dfrac{d}{dt} = \dfrac{\partial}{\partial t} + \mathbf{u}\cdot\nabla$ the Lagrangian-material derivative. p is the dynamic pressure and ρ and T are the fluid mixture density and temperature respectively. η_i denotes species i, i=1,2 being the reacting species and i=p being the product. $Y_i = \dfrac{\rho_i}{\rho}$ is the mass-fraction for species i (ρ_i is the species' partial density) and $\dot{w}$ is the reaction rate. Re is the Reynolds number, $Re = \dfrac{\tilde{U}_o\tilde{L}_o}{\tilde{v}}$, with $\tilde{v}$ being the kinematic viscosity. Similarly, Pe is the Peclet number $Pe = \dfrac{\tilde{U}_o\tilde{L}_o}{\tilde{\alpha}}$. $\tilde{\alpha}$ is the thermal diffusivity, which under the unity Lewis number assumption is equal to the mass diffusivity $\tilde{D}$ which, in turn, is the same for all species. A_f is the frequency factor, $A_f = \dfrac{\tilde{A}_f\tilde{\rho}_o\tilde{L}_o}{\tilde{U}_o}$. ϕ^* and ϕ are the molar and mass stoichiometry ratios respectively ($\phi = \phi^*\dfrac{\tilde{M}_1}{\tilde{M}_2}$, $\tilde{M}_i$ being the molar mass of species i). Q_o is the enthalpy of reaction, $Q_o = \dfrac{\widetilde{\Delta h_f}}{\tilde{c}_p\tilde{T}_o}$, where $\tilde{c}_p$ is the mixture specific heat. T_a is the activation temperature $T_a = \dfrac{\tilde{E}_a}{\tilde{R}T_o}$, where $\tilde{E}_a$ is the activation energy and $\tilde{R}$ the universal gas constant.

For primarily numerical reasons the above equations are recast into non-primitive variable form. For the equations governing fluid motion this is initiated via the use of the Helmholtz decomposition [10],

Helmholtz Dec. $\mathbf{u} = \mathbf{u}_\omega + \mathbf{u}_p + \mathbf{u}_e$ (8)

which recognizes that the velocity can be split into a vorticity induced solenoidal component, $\mathbf{u}_\omega$, ($\nabla \times \mathbf{u}_\omega = \nabla \times \mathbf{u}$, $\nabla \cdot \mathbf{u}_\omega = 0$) and two irrotational components; one induced by volumetric expansion, $\mathbf{u}_e$, and the other by the flow boundary conditions $\mathbf{u}_p$). The vortical component is obtained from the definition of the vorticity $\omega \hat{\mathbf{k}} = \nabla \times \mathbf{u}$ ($\hat{\mathbf{k}}$ is the unit vector normal to the plain of motion) and by the use of the streamfunction (ψ) i.e.

Streamfunction $\nabla^2 \psi = -\omega$ $\mathbf{u}_\omega = \nabla \times (\psi \hat{\mathbf{k}})$ (9a,b)

The irrotational components are obtained from the relevant continuity equation via the introduction of the concept of the velocity potential (ϕ):

Expansion $\nabla^2 \phi_e = -\dfrac{1}{\rho} \dfrac{d\rho}{dt}$ $\mathbf{u}_e = \nabla \phi_e$ (10a,b)

"Potential" $\nabla^2 \phi_p = 0$ $\mathbf{u}_p = \nabla \phi_p$ (11a,b)

The evolution of the vorticity field required in the evaluation of the vortical velocity component is described by the vorticity equation established by taking the curl of the momentum equation :

Vorticity $\dfrac{d\omega \hat{\mathbf{k}}}{dt} + (\nabla \cdot \mathbf{u}) \; \omega \hat{\mathbf{k}} = \dfrac{\nabla \rho \times \nabla p}{\rho^2} + \dfrac{1}{Re} \nabla^2 \omega \hat{\mathbf{k}}$ (12)

Density related quantities in both equations (10a) and (12) are obtained from the temperature field via the equation of state.

To simplify the scalar transport equations, Shvab-Zeldovich (S-Z) non-reacting variables (λ, γ) are introduced:

S-Z Variables $\lambda = Y_1 - \phi Y_2$ $\gamma = T - \dfrac{Q_o \phi}{1+\phi} Y_p$ (13a,b)

These variables are constructed from combinations of the primitive reacting scalars in such a way that the equations governing their transport (obtained from algebraic manipulations of equations (5)) are void of reaction terms, and are hence much simpler to deal with: i.e.

$$\frac{d\beta}{dt} = \frac{1}{Pe} \nabla^2 \beta$$ (14)

6

where $\beta = \lambda$ or γ.

Depending on the application, the particular choice of these variables can also result in further simplifications. A good example of this is illustrated by the γ variable used here. By combining the temperature with the product mass-fraction into one variable, one can capitalize on the fact that if the initial conditions imply that these two properties are initially directly related (i.e. $\gamma(x,0)=1$), then equation (14) above suggests that they will remain related at all later times. This, in essence, reduces the equations to be solved by one, since the solution for γ is trivially known (i.e. $\gamma(x,t)=1$).

The main disadvantage in the use of Shvab-Zeldovich variables is that they impose the substantial limitations on the choice of the transport properties noted earlier. This is because in order to reduce the equations, the mass-diffusion coefficients had to be assumed equal for all species and the Lewis number had to be chosen equal to unity.

In analogy to the treatment of the flow equations, the Shvab-Zeldovich scalar transport equations are recast into gradient form:

S-Z Gradient
$$\frac{dg}{dt} + g \cdot \nabla u + g \times (\omega \hat{k}) = \frac{1}{Pe} \nabla^2 g \qquad (15)$$

where $g = \nabla\beta$

Evidently, integration of the solutions of the gradient equations provides the scalar field only within a constant. This constant is defined by the boundary conditions (β_p). Thus, in an approach similar to the Helmholtz decomposition of the velocity field, the total Shvab-Zeldovich scalar field solutions are obtained by adding these two components.

S-Z Scalar Dec.
$$\beta = \beta_g + \beta_p \qquad (16)$$

In the limiting case of infinite reaction rate combustion, where the reaction zone collapses onto a line and reactant coexistence is prohibited, the Shvab-Zeldovich variable solutions together with the equation of the conservation of the species mass-fractions (eq.6) are able to provide a complete description of the reacting field. i.e.

Infinite reaction: $\quad \lambda \geq 0 \quad Y_1 = \lambda, \ Y_2 = 0, \quad Y_p = 1 - \lambda \qquad (17a)$

$$\lambda \leq 0 \quad Y_1 = 0, \ Y_2 = -\frac{\lambda}{\phi}, \ Y_p = 1 + \frac{\lambda}{\phi} \qquad (17b)$$

The temperature field is obtained using the definition of γ. If the reaction speed is finite, on the other hand, the Shvab-Zeldovich solutions and the mass-fraction conservation equation do not contain all the information necessary to construct the reacting field. At least one reacting scalar

7

must be explicitly obtained. In the formulation presented here, this scalar is chosen to be the product mass fraction, i.e

Product
$$\frac{dY_p}{dt} = \frac{1}{Pe}\nabla^2 Y_p + (1+\phi)\frac{\dot{w}}{\rho}$$
(18)

must be solved. Once the product mass-fraction solution is known, the reacting species solutions can be constructed according to

Finite reaction:
$$Y_1 = \frac{\lambda + \phi(1-Y_p)}{1+\phi} \qquad Y_2 = \frac{-\lambda + (1-Y_p)}{1+\phi}$$
(19)

and the temperature solution by using the definition of γ, to completely describe the reacting scalar field. It should finally be noted that the non-reacting flow case is easily included in the finite reaction speed case by simply specifying $Y_p = 0$.

III. NUMERICAL SCHEME

The numerical scheme by which the flow and scalar field equations of the previous section are to be solved is the Vortex-Transport Element Method. A non-reacting version of this scheme was presented in ref. [11].

The numerical integration of the governing equations is initiated by discretizing the vorticity, "material density derivative" $(-\frac{1}{\rho}\frac{d\rho}{dt})$, Shvab-Zeldovich scalar gradients and product mass fraction via a generic discretization function. It distributes a property ζ over a field of elements which are characterized by a finite area, A_i, and by a strength, ζ_i, locally distributed via a radially symmetric core function, f_δ. The discretization function is also used to reconstruct the discretized quantities at later times and is:

$$\zeta(x,t) = \sum_{i=1}^{N} \zeta_i(t) A_i(t) f_\delta(|x-\chi_i|)$$
(20a)

where $\chi_i = \chi_i(x,t)$ is the element location. The core function which is characterized by the core radius δ within which the most significant contribution of each element is experienced, is a second order Gaussian, i.e.

$$f_\delta(r) = \frac{1}{\pi\delta^2}\exp(-\frac{r^2}{\delta^2})$$
(20b)

and it enables a second order accuracy of discretization under the condition that core overlap between neighboring elements is maintained [12].

The velocity induced by the discretized vorticity field is obtained via a discrete, desingularized Biot-Savart law resulting from the solution of equation (9):

$$u_\omega(x,t) = \sum_{i=1}^{N} \Gamma_i(t) \, K_\delta(x-\chi_i(t)) \qquad (21a)$$

where $\Gamma_i(t) = \omega_i(t)A_i(t)$ is the element circulation and K_δ is the desingularized kernel of the Biot Savart law given by:

$$K_\delta(x) = -\frac{(y,-x)}{2\pi r^2}\left[1 - \exp\left(-\left(\frac{r}{\delta}\right)^2\right)\right] \qquad (21b)$$

The expansion component of velocity is obtained in a similar fashion, i.e. via a discrete, desingularized equivalent of the convolution resulting from the governing Poisson equation (eq.10):

$$u_e(x,t) = -\sum_{i=1}^{N} \left(-\frac{1}{\rho}\frac{d\rho}{dt}\right)_i (t) \, A_i(t) \, \nabla G_\delta(x-\chi_i(t)) \qquad (22a)$$

where ∇G_δ is the desingularized gradient of the Poisson equation and is given by

$$\nabla G_\delta(x) = -\frac{(x,y)}{2\pi r^2}\left[1 - \exp\left(-\left(\frac{r}{\delta}\right)^2\right)\right] \qquad (22b)$$

The component of the velocity field induced by the boundary conditions is obtained by solving the governing Laplace equation (eq.11) under a Schwartz–Christoffel conformal mapping transformation. The total velocity is hence obtained via the Helmholtz decomposition.

The Shvab-Zeldovich scalar solutions are obtained from the corresponding discrete gradient fields in an analogous manner since the two quantities may also be related via a Poisson equation, i.e.

$$\nabla^2\beta = \nabla \cdot g \qquad (23)$$

Hence the Shvab-Zeldovich scalar fields may be expressed as

$$\beta(x,t) = \sum_{i=1}^{N} g_i(t) A_i(t) \cdot \nabla G_\delta(x-\chi_i(t)) + \beta_p \qquad (24)$$

where β_p is the integration constant obtained from boundary conditions. The complete reacting scalar field is obtained by using these solutions in conjunction with the product mass-fraction solutions which are obtained from equation (20).

The time evolution of the flow and scalar fields is established by numerically integrating the governing transport equations locally to each element. This is done in two fractional steps.

The first step, the non-diffusive step, includes all processes other than diffusion. During this step the element locations are updated by numerically integrating

$$\frac{d\chi_i}{dt} = u \qquad (25)$$

that is, the elements are advected with the local velocity vector. This defines element trajectories, as well as material lines. The element vorticity is updated by locally integrating the corresponding circulation equation,

$$\frac{d\Gamma_i}{dt} = -\frac{[\nabla\rho]_i}{\rho} \times \frac{du}{dt} A_i \qquad (26)$$

were the pressure gradient has been substituted by the material acceleration using the relevant momentum equation. Both equations (25) and (26) are integrated via Euler predictor-corrector schemes and the material acceleration in equation (26) is established by a two-step iteration forward-difference scheme.

The direct integration of the corresponding Shvab-Zeldovich scalar gradient transport equation,

$$\frac{dg_i}{dt} + g_i \cdot \nabla u + g_i \times (\omega_i \ \hat{k}) = 0, \qquad (27)$$

is avoided. Recognizing that under the physical requirements of the problem, isoscalar and material lines may coincide and considering the kinematical evolution of the latter (relating the change in length of a material line elemental segment (δl) to the velocity difference at its ends, i.e.

$$\frac{d(\delta l)}{dt} = \delta l \cdot \nabla u \ ) \qquad (28)$$

equation (27) may be transformed into a simpler form [11], i.e.

$$\frac{d}{dt}\left[\frac{g_i}{\rho \ \delta l_i}\right] = 0 \quad \text{with} \quad g_i = g_i \ \hat{n}_i \qquad \delta l_i = |\delta l_i| \qquad (29a,b,c)$$

where $\hat{n}$ is the unit vector normal to the material line. Equation (29) simply implies that along a material-isoscalar line

$$\frac{g_i}{\rho \ \delta l_i} = \text{constant} \qquad (30)$$

The constant is specified by the initial conditions. δl_i as well as $\hat{n}_i$ are readily available due to the Lagrangian nature of the scheme which trivially provides the topology and evolution of material lines.

For the product mass-fraction field evolution (finite reaction speed chemistry) an alternative approach is followed. The concept of product particles is introduced. Such particles

10

are positioned at the center of the computational elements and are convected with the latter by the flow. Product particles directly experience the combustion process. This is accomplished by integrating (via an Euler predictor-corrector scheme) the relevant transport equation, i.e.

$$\frac{dY_p}{dt} = (1+\phi)\,\dot{w} \tag{31}$$

for each particle. The corresponding element strengths are then established from the particle values via the discretization function (eq.20). The effects of any error associated with such a discretization are minimized by correcting the product particle values at the end of the complete numerical integration, i.e. after the diffusion step, via knowledge of their values at the end of the first integration step, i.e. after the convection-reaction process.

In the second fractional integration step diffusion effects are accounted for. This is accomplished via the core expansion scheme [13]. Diffusion is simulated by expanding the element core size according to:

$$\delta_i^2(t+\Delta t) = \delta_i^2(t) + \frac{4\,\Delta t}{C} \tag{32}$$

where $C=Re$ for $\zeta=\omega$ and $C=Pe$ for $\zeta=g$ or Y_p. This expression is arrived at by using the element field, defined by the discretization function (eq.(20)) to analytically solve the governing diffusion equation,

$$\frac{d\zeta}{dt} = \frac{1}{C}\nabla^2\zeta, \tag{33}$$

under the assumptions that the strength and area of the element are constant and that the core radius is only a function of time.

The presence of the baroclinic torque in the evolution of the vorticity field requires knowledge of the density gradient field. This in turn necessitates knowledge of the product mass-fraction gradient field. In the infinite reaction speed case this is trivially established from the S-Z gradients. For the finite reaction speed on the other hand it is established by differentiating the product mass-fraction field given by equation (20) and is

$$\nabla Y_p(x,t) = \sum_{i=1}^{N} Y_{pi}(t)\,A_i(t)\,\nabla f_\delta(x-\chi_i) \tag{34}$$

where

$$\nabla f_\delta(x) = -2\,\frac{(x,y)}{\delta^2}\,f_\delta(x) \tag{35}$$

11

The severe stretching of the Lagrangian mesh used in the discretization of the transported quantities, which increases the distance between neighboring elements, may lead to the deterioration of the accuracy of the solution. To overcome this problem, a scheme of local mesh refinement is adopted whereby elements are continuously introduced and deleted to ensure core overlap. Strong overlap is enforced near the inlet of the domain by allowing a small maximum separation between neighboring elements. This condition is relaxed further downstream by increasing this threshold value, thus allowing for efficient computations without compromising the accuracy of the numerical scheme.

IV. FLOW GEOMETRY, AND BOUNDARY CONDITIONS

The geometry of the computational domain together with some of the boundary conditions are shown in figure 1. The shear layer evolves in a two dimensional channel of height H and length X_{max}, between two parallel streams (1-top, 2-bottom) which mix downstream of a thin splitter plate. The top and bottom walls are modeled as rigid, slip, impermeable and adiabatic planes These conditions are satisfied by mapping the entire channel region on the upper half of a complex plane, and using the appropriate image system of the vortex and transport elements. At the downstream section, a condition of vanishing vorticity and scalar gradient is used as outflow boundary condition, and is applied by removing the elements which cross the $x=X_{max}$ plane. At the inlet section, the velocity-vorticity, Shvab-Zeldovich variables-gradients and product mass fraction (for finite reaction speed simulations) profiles are specified as follows:

Velocity
$$U(x=0,y,t) = \frac{U_1 + U_2}{2} + \frac{U_1 - U_2}{2} \, erf(\frac{y-0.5}{\sigma})$$
(36)

Vorticity
$$\omega(x=0,y,t) = - \frac{U_1 - U_2}{\sqrt{\pi} \, \sigma} \exp(- \frac{(y-0.5)^2}{\sigma^2})$$
(37)

S-Z variables
$$\lambda(x=0,y,t) = \frac{1-\phi}{2} + \frac{1+\phi}{2} \, erf(\frac{y-0.5}{\sigma}) \qquad \gamma(x=0,y,t) = 1$$
(38a,b)

S-Z gradient
$$\nabla\lambda(0,y,t) = (0 \, , \frac{\partial\lambda}{\partial y}(0,y,t)) \qquad \nabla\gamma(0,y,t)=(0,0)$$
(39a,b)

with
$$\frac{\partial\lambda}{\partial y}(x=0,y,t) = \frac{1+\phi}{\sqrt{\pi} \, \sigma} \exp(\frac{(y-0.5)^2}{\sigma^2})$$
(40)

12

Product $\quad \quad \quad \quad Y_p(x=0,y,t) = Y_{p_{max}} \exp(\dfrac{(y\text{-}0.5)^2}{\sigma^2})$ $\quad \quad \quad \quad$ (41)

In the above profiles, as well as in the numerical simulations, the channel height is used as the space non-dimensionalizing scale. σ is the standard deviation of the Gaussian profiles defining the inlet vorticity, gradient of the λ variable and the product mass-fraction. Its relation to the scaling length (H) is obtained by requiring that two wavelengths of the most unstable mode of the uniform density shear layer (obtained from linear stability analysis) fit within the channel height. Finally, it is noted that in the numerical simulations the velocity field is scaled with the top stream velocity (U_1) whereas the density and temperature fields by the common to both streams (see next paragraph) values of these properties (ρ_0, T_0).

The profile for the λ Shvab-Zeldovich variable is obtained by assuming that each of the two fluid streams consists of a single reactant (i.e. $\lambda_1=1$, $\lambda_2=\text{-}\phi$) which at the inlet experiences an errorfunction type profile. Profiles of this type are not unlike the experimentally observed profiles for the two reacting species. For the γ Shvab-Zeldovich variable, the assumption is made that the temperature and product mass-fraction profiles are directly related, yielding a constant value profile. Under the behavior imposed by the governing equations such an assumption is valid for flows which prior to combustion were of uniform temperature and in which no product was present.

In order to avoid having to deal with ignition phenomena at the inlet for the finite reaction speed case (note the temperature dependent nature of the reaction rate (eq.7)), a finite amount of product is introduced there. This is described by the Gaussian profile given above (eq.41) where $Y_{p_{max}}$ is chosen as 0.4. The direct relation of the product mass-fraction and the temperature implies that the temperature at the inlet is raised and hence combustion becomes possible. In the infinite reaction speed case where reactants react on contact, ignition problems do not exist and the inlet product mass-fraction profile is uniquely defined by the Shvab-Zeldovich variables as explained in Section II (eq.17). Hence, the scalar field inlet profiles specified above which are used in the numerical simulation of the flow, specify the inlet species profiles shown in figure 2. The related temperature and density profiles can straightforwardly be deduced from the product mass-fraction profile as earlier explained.

Initialization of the calculation is carried out by assuming that the inlet conditions persist throughout the domain. Hence, the vorticity-S-Z gradient-product layer between the two fluids, defined by the above inlet profiles is discretized by distributing vortex-transport-product elements over nine material layers (lines) lying within the support of vorticity. The elements are of square area of side h=0.0195. The value of the core radius is δ=0.0234 (i.e.δ>h).

Finally, external forcing is implemented at the inlet. The forcing signal, shown in figure 3, consists of in-phase components of the most unstable mode of the uniform density layer and

its subharmonic, both at an amplitude $A_f = A_s = 0.025$. The interaction of the two forcing frequencies gives rise to two types of eddies. The eddy which forms during the part of the cycle which the two components are in phase - the "fundamental" eddy - is larger than the one which forms in the second part of the subcycle - the "subharmonic" eddy - during which the two components are out of phase. The forcing is implemented by displacing elements at the inlet according to the forcing signal.

V. RESULTS

Simulations at both finite and infinite reaction speed were carried out with the double aim of a) establishing a preliminary assessment of the effects of the presence of combustion on both the flow and scalar fields and b) of providing a comparison between the finite and infinite reaction speed models.

The time step for all calculations was $\Delta t = 0.1$ and the length of the domain $X_{max} = 5$. The fluid dynamical parameters were kept constant for all runs. The inlet velocity ratio is $r = \frac{U_2}{U_1} = 0.5$ and the Reynolds number (and Peclet number since Pe=Re) based on the velocity difference across the layer ($\Delta U = U_1 - U_2$) and on the vorticity layer's original thickness ($d = 2\sigma$) is $Re_d = \frac{\Delta U\, d}{\nu} = 500$. It should be noted that the Reynolds number could have also been defined with respect to the channel height H, since, as was earlier explained, H is characteristic of the largest cross-stream scale of the layer. The resulting Reynolds number is $Re_H = \frac{\Delta U\, H}{\nu} = 6400$.

For the finite reaction speed cases the chemical parameters were specified as follows: the activation temperature is $T_a = \frac{E_a}{RT_o} = 10$, the frequency factor $A_{f_d} = \frac{A_f\, d}{\Delta U} = 100$ ($A_{f_H} = \frac{A_f\, H}{\Delta U} = 1280$), the mass stoichiometry ratio $\phi = 1$ and the enthalpy of reaction (referred to in this text as "heat release") $Q_o = \frac{\Delta h_f}{c_p T_o} = 6$. The corresponding Damkohler number ($Da = \frac{\tau_{dif}}{\tau_{che}}$ where $\tau_{dif} = \frac{d^2}{\alpha}$ is the diffusion time scale and $\tau_{che} = \frac{T_f}{A_f} \exp(\frac{T_a}{T_f})$) the chemical reaction time scale) and the Karlovitz number ($Ka = \frac{\tau_{che}}{\tau_{flw}}$ where $\tau_{flw} = \frac{d}{\Delta U}$ is the flow time scale) are $Da_d = 1026$ and $Ka_d = 0.49$, respectively [$Da_H = 168110$, $Ka_H = 0.038$]. The ranges of values of these non-dimensional numbers, which for a given flow are controlled by the chemical time scale, are limited by the available computational resources. This is not only because increases in the reaction speed will, evidently, necessitate increases in the temporal numerical resolution, but also because under these conditions the reaction zone thickness is reduced, thus requiring higher spacial numerical resolution as well. The values of the Damkohler and Karlovitz numbers used here are, nevertheless, not far from physically realistic values, describing a reasonably fast reaction . It

14

should be pointed out though that the same is not necessarily true of the parameters used to create them. Specifically, the values of the activation temperature and the frequency factor, while higher than those used in previous work [7] are still quite low. This is a consequence of the fact that due to the nature of the reaction rate the activation temperature has an independent effect on the reaction zone thickness. Even if the effect of increasing the activation temperature on the reaction time scale, is counterbalanced by an appropriate frequency factor, the reaction zone thickness is, nevertheless, reduced. Hence, spacial resolution limits the range of values of the activation temperature and the limitations on the reaction time scale, in turn, limit the frequency factor.

The infinite reaction speed model requires only one chemical parameter, the heat release. This is specified to be the same as that used in the finite reaction speed simulations, i.e. $Q_o = 6$

To assess the effect of combustion on the flowfield, the reacting calculations were repeated but this time the effects of the variable density field on the fluid dynamical field were ignored. That is, while the density was allowed to vary due to combustion, the density used in the evolution of the flowfield was kept constant and equal to its inlet value. Since, under the earlier noted assumptions, the variation in the density field is the only means by which the reacting field can influence the flowfield, then by keeping the flow density invariant the flowfield remains ignorant of the presence of the reacting field. In what follows, the cases where the flow and combusting fields are decoupled in this manner, will be termed as the "ρ_{flow} uniform" cases. Evidently, as far as the flow is concerned these cases are indistinguishable from uniform density non-reacting calculations. Hence, in the analysis of the flowfield they will be treated as such. For the scalar field on the other hand these cases differ from uniform density calculations and hence they will be properly distinguished.

Figure 4 displays a flowfield comparison between the non-reacting layer (left) and layers reacting at finite (middle) and infinite (right) reaction speeds. The shear layer is depicted using the vortex elements and their local velocity vectors. The velocity is plotted with respect to the inlet mean velocity to highlight the relative motion within the layer. To describe the evolution of the flowfield in time, three sequential time frames are shown. In order to be able to provide a clearer description of the flow, which is partly inhibited by the small size of the flow visualizations of figure 4, the first time frame of each case shown in the figure is reproduced in figure 5 at an enhanced scale.

It is seen that in all cases, and in agreement with experimental evidence, the flow is dominated by large scale coherent vortical structures. The repetitiveness of the flowfield evolution for each case, a manifestation of the external forcing, is also evident. But the flow behavior varies between the different cases and comparison between them yields two major

conclusions: a) Exothermic combustion significantly modifies the flowfield, resulting in reduced layer growth, and b) the flowfield characteristics of the finite and infinite reaction speed cases, while substantially different from those of the non-reacting flow, exhibit striking similarities.

Comparison betwee:. the non-reacting and reacting cases indicates that density variation resulting from the combustion heat release modifies the flowfield by altering the shape, evolution and interactions of the vortical structures. During the initial rollup, the fundamental eddies appear less rolled and larger in overall size (area) than their uniform density, non-reacting, counterparts. This increase in size though, appears to be mainly in the streamwise direction resulting in more elongated, more elliptical structures. Similar features are experienced by the subharmonic eddies which, additionally, appear much less coherent. Further downstream, where the eddies start to interact, major differences are experienced. In the non-reacting flow, each subharmonic eddy interacts with its downstream fundamental eddy. The two, pair (by spiraling towards each other in a clockwise direction) to form a larger, coherent and highly elliptical structure which continues to rotate, exposing its major axis to the streamwise flow. This results in significant growth of the shear layer. In the presence of reaction this process is fundamentally altered. Eddy pairing is resisted and the subharmonic eddy appears to be torn between its two neighboring fundamental eddies (with the downstream eddy absorbing its larger part) in a much more continuous process than pairing. The resulting larger structures appear less elliptic and coherent than before and they tend to keep their major axis more aligned with the streamwise direction. This impairs the layer cross-stream growth significantly. Finally it is noted that the convective speed of the vortical structures is also altered in the presence of reaction. Figure 5 displays this more clearly. Eddies formed during the same subcycle of the forcing function (indicated by arrows) appear to move faster in the reacting flow. This feature is suspected to be primarily a consequence of the volumetric expansion associated with the combustion heat release which in semi-confined flow like the one considered here will cause a streamwise acceleration.

The similarity of the flowfield between the finite and infinite reaction speed cases on the other hand is substantial. The eddy evolution particularly at the earlier parts of the domain is strikingly similar. Eddy interactions are by tearing in both cases and some minor differences can only be detected towards the end of the domain where for the infinite reaction speed case the subharmonic eddy appears to be able to survive longer. The effect of reaction on the eddy speed also appears to be similar for the two cases.

Figures 6 and 7 which describe features of the mean flow indicate that the above noted instantaneous behavior is repetitive and thus biases the mean flow characteristics. Figure 6 presents comparisons of the mean velocity profiles (at a fixed downstream location (x=3)) between the non-reacting flow and the two reacting cases; finite (6a) and infinite (6b). The

characteristics of the profiles shown, are qualitatively typical of most downstream locations within the computational domain. The steepening of the profiles in the presence of reaction, which suggests smaller shear layer growth, is obvious. The similarity between the finite and infinite reaction case profiles is also noted. The shifting of these profiles to higher speeds, which was earlier suggested by the faster moving structures, is evident. It is interesting to note that for the reacting cases the mean velocity profile loses its monotonic nature, typical of uniform density shear layers. Instead, close to the fast free stream an overshoot, and close to the slow free stream an undershoot of the respective neighboring free stream values are experienced. This type of features of the mean velocity profile were also documented in ref.[6] for a reacting temporal shear layer and were attributed to the presence of the baroclinic generation of vorticity. Evidence supporting this argument was also established in our earlier work with non-reacting variable density shear layers [14], where similar types of overshoots and undershoots were experienced.

In figure 7 the vorticity thickness defined with respect to the local free streams as

$$\delta_\omega = \frac{\overline{U}_1(x) - \overline{U}_2(x)}{\left[\left|\left(\frac{\partial \overline{u}}{\partial y}\right)_x\right|\right]_{max}} \qquad (42)$$

(where the overbar indicates a time-averaged property) and is, hence, representative of the spacial cross-stream thickness of the layer is plotted versus the streamwise coordinate. (It should be pointed out that the definition of the vorticity thickness used here is not necessarily impaired by the non-monotonical nature of the velocity profile since the overshoots-undershoots are small ($<2\%\Delta U$). An alternative definition of δ_ω from the points of the mean velocity profiles where the velocity varies by 5% of the free-stream value -i.e. the typical experimental approach- would give rise to similar results since the overshoots-undershoots would not be detected.) As in figure 6 the comparison in each part of figure 7 is between the non-reacting and reacting flow. As expected, a drop in the vorticity thickness growth for the reacting cases is clearly seen. This drop is most significant towards the end of the domain where the effect of the inhibition of eddy pairing is most pronounced. Thus, the alteration of the eddy interactions represents the most important mechanism by which the combustion exothermicity reduces the forced shear layer growth.

Figure 8 displays the instantaneous vorticity fields for the three cases of figure 5. It should be noted that only the $0<x<3$ part of the computational domain is indicated. As expected, the correlation with the vortical structures is evident. The same is also true for the similarity of the finite and infinite reaction speed cases. But the figure makes clear another difference between the non-reacting and reacting cases. The former is characterized by vorticity of a single sign (negative) while the latter by vorticity of both signs; a field of mainly negative vorticity with

17

islands of positive vorticity surrounding the vortical structures. The origin of the uniformly negative vorticity of the non-reacting case and the overwhelmingly negative field of the reacting cases should come as no surprise since the inlet vorticity is negative (top stream is fastest, resulting in clockwise rotation). The positive vorticity of the reacting cases must be a manifestation of the baroclinic generation since from the mechanisms of vorticity modification present here, only this one may change the vorticity sign. The presence of the positive vorticity around the vortical structures must have important effects on the flow and is suspect for a significant number of the differences between the non-reacting and reacting flowfields. It should, for example, with its anticlockwise rotation, be responsible for the overshoots and undershoots of the average velocity profiles as earlier suggested. One could speculate that its location close to the free streams may inhibit entrainment of irrotational fluid inside the vortical structures. By creating a tendency towards counterclockwise rotation on the outskirts of the eddies it may also be responsible for the inhibition of pairing, which as was earlier noted is initiated by a clockwise spiraling of eddies around one another. To be able to clarify these points, a closer scrutiny of all the mechanisms by which combustion and the resulting variable density field modify the vorticity field needs to be carried out. This is currently being accomplished and the results will be presented in a future article (ref. [15]).

The similarity of the vorticity fields of the two reacting cases, which like earlier findings points to the effectiveness of the infinite reaction speed model to reproduce the effect of the actual, finite reaction speed combustion on the flowfield, also provides an internal consistency check of the numerical scheme. As noted in the previous paragraph, the dual sign of the vorticity field of the reacting cases is a manifestation of the baroclinic generation of vorticity. This mechanism of vorticity modification requires knowledge of the density gradient field. As was earlier seen (Section III) due to the different numerical approaches in dealing with the product mass-fraction field in the finite and infinite reaction speed cases, the density gradient is established in quite different ways for the two cases. The qualitative agreement of the vorticity fields of figure 8 points to the validity of both approaches.

As a final tool in the investigation of the effect of the combusting field on the flowfield, statistically averaged quantities are considered. In a variable density field, such as the one resulting from the combustion heat release this is usually done using Favre (density weighted) averaging. The advantage of this type of averaging over the more traditional Reynolds averaging is that it results in simpler averaged equations by avoiding terms involving density fluctuations. Its major disadvantage lies in the fact that the resulting extra terms in the governing equations, while fewer in number, are less physically intuitive. Furthermore, they do not incorporate all the features of the fluctuating (in the Reynolds sense) field, since fluctuating quantities are part of

18

the Favre averaged quantities, while at the same time they involve the effect of the average density.

In direct analogy to Reynolds averaging, the implementation of Favre averaging of the equations of motion results in extra terms formed by the products of the fluctuating quantities. In the two dimensional case considered in this work these quantities are:

$$\overline{\rho \widetilde{u''v''}} \ (= \overline{\rho u''v''}), \quad \overline{\rho \widetilde{u''^2}}, \quad \overline{\rho \widetilde{v''^2}} \tag{43}$$

As pointed out in ref.[16] the first term, the turbulent stress term, represents the rate of transfer of momentum flux. The second and third terms are indicative of the flow's turbulent kinetic energy per unit volume in the streamwise and cross stream directions respectively and are representative of the turbulence intensity. The total flow turbulent kinetic energy can be defined as :

$$KE = \frac{\overline{\rho \widetilde{u''^2}} + \overline{\rho \widetilde{v''^2}}}{2} \tag{44}$$

As noted earlier, due to the presence combustion heat release, the density decreases significantly and this results in decreased Favre turbulent quantities (eqs.43 and 44). It should be clear though that this does not necessarily imply that the oscillating nature of the flow is diminished. It only indicates to the fact that the mean density is reduced. To clarify this point, the ρ_{flow} uniform case with the variable density of its reacting field used in the calculation of the turbulent quantities, will be provided for comparison. Since this latter case experiences the exact same flowfield as the non-reacting case then the corresponding Reynold's turbulent quantities are identical. Hence, any difference in the Favre turbulent quantities between the two cases can only be a consequence of the variable density and will thus provide an indication of the effect of the decreasing mean density.

Figure 9a presents a comparison of turbulent stress profiles between the finite reaction speed case, its corresponding uniform flow-density case (as explained above) and the non-reacting case. Figure 9b presents an analogous comparison for the infinite reaction speed case. Profiles are displayed at a fixed downstream location ($x=2.5$) and are typical of the profiles experienced in the whole field. It is clearly seen that the region of significant fluctuations is related to the shear layer region. This implies that the shear layer represents the prime mechanism of turbulent mixing of the two streams. The bell-Gaussian shape of the profiles, in analogy to those of the Reynolds shear stress in a uniform density flow [17], clearly indicates that turbulent momentum transfer from the free streams to the shear region represents the latter's prime mechanism of growth. But the figure also clearly shows that this transfer is significantly diminished in the presence of combustion heat release. Furthermore, it is seen, that the effect of the decreased mean density, while significant, cannot account for the whole drop in the turbulent stress. This suggests that heat release acts to dampen the oscillating nature of the flowfield. In

agreement with previous analysis the figure also points to the similarity in the characteristics of the finite and infinite reaction speed cases.

A similar picture is seen in the turbulent kinetic energy profiles (figure 10a,b). They are plotted at the same downstream location as those of the turbulent stress. Again, it is seen that the presence of combustion, decreases the kinetic energy of the flow and that only part of this decrease can be attributed to the decrease in the mean density; the fluctuating field is dampened as well. It is interesting to note the change in the shape of the reacting case profile. The single peak profile experienced by the non-reacting flow is transformed into a three peak profile. The fact that the ρ_{flow} uniform case profile experiences a singe peak profile, suggests that the transformation is not due to the mean density or its fluctuation. Rather it is a result of the altered velocity field and it implies, as is the case, significant differences in the field's structure. The shift from a single to a three peak profile invites the speculation that this might be related to the alteration of the vorticity field in the cross-stream direction from an all negative (for non-reacting) to a positive-negative-positive (for reacting) field noted earlier. As was seen this modifies the monotonic nature of the non-reacting flow mean velocity profile to one with a gradient which experiences three peaks instead of one. Thus, it appears that the turbulent kinetic energy could be related to the cross stream gradient of the mean velocity profile.

Finally, a brief assessment of the feedback of the modified flowfield on the reacting field itself is to be attempted. Figure 11 displays two dimensional visualizations of product mass-fraction fields. It should be remembered that under the assumptions imposed on the governing equations these two-dimensional mass-fraction maps are equivalent to temperature maps or inverse density maps. The comparison is between the ρ_{flow} uniform finite reaction case and the corresponding finite and infinite reaction speed cases. The figure clearly shows that product formation is strongly dependent on the evolution of the vortical structures which in turn are dependent on the destabilization of the vorticity-material layer separating the two fluids at the inlet. Because of this dependency figure 11 may also be used to deduce the earlier noted effects of the combusting field on the flowfield. The similarities between the finite and infinite reaction speed cases are evident here as well. This figure provides some of the reasons why the infinite reaction speed model is able to provide such a good approximation of the finite reaction speed simulations. It is noted that the finite reaction speed result clearly indicates features of thin reaction zone combustion rather than of distributed reaction regions. Furthermore, it is seen that even in the braids where the strain is highest the product concentrations are high. This implies that quenching, i.e. the collapse of the reaction zone due to excessive strained and the associated drop in temperature, does not take place. Both of these effects point to the fact that the parameters chosen for the finite reaction speed simulation are such that they result in a fast

reaction (compared to the flow). Thus, it can be concluded that the results presented herein indicate that the infinite reaction speed model is effective at mimicking the behavior of the finite reaction speed case when the latter experiences a fast reaction (i.e. approaches the infinite reaction speed limit) and not necessarily for all other cases.

Figure 12 displays the quantitative effect of the combustion modified flowfield on product formation. This is accomplished by presenting the streamwise evolution of the product thickness defined as

$$\delta_\Phi(x) = \frac{\int_o^1 \overline{\Phi}(x,y)\,dy}{\int_o^1 \overline{\Phi}(0,y)\,dy} \tag{45}$$

where Φ is the product density $\rho_p = \rho Y_p$. Hence the product thickness is representative of the mass of product at a given channel cross-section. In each of the two parts of figure 12 the product thickness of the reacting case is contrasted to two versions of the thickness of the comparison, ρ_{flow} uniform, case. It should be remembered that the comparison case is created by simply decoupling the density of the flowfield from the density of the reacting field which is allowed to vary. It should be recognized though, that using a variable density in the calculation of the mass of product, practically eliminates the effect of the change of volume from this latter quantity. Thus the comparison between the reacting and the ρ_{flow} uniform cases does not necessarily provide a measure of the relative difference in mass of product but rather it is more indicative of the instantaneous relative size of the areas where product exists. For this reason the calculation of the product thickness for the ρ_{flow} uniform case is repeated using the uniform inlet density for the reacting field as well. This thickness is also shown in figure 12. Figure 12a shows this arrangement of thicknesses for the finite reaction speed case and 12b for the infinite reaction speed.

The figure clearly shows that combustion exothermicity reduces product formation by both reducing the area where product exists as well as by reducing the density over this area. The second effect is by far the most dominant. The drop in the area where product is formed is not as significant as that of the vorticity thickness seen earlier because the latter only accounts for the cross-stream thickness of the layer, i.e the cross-stream size of the vortical structures but not their streamwise size. As was seen earlier in the flow visualizations, for the reacting cases the cross-stream size of the eddies is reduced substantially, but their overall size only marginally.

VI. CONCLUSIONS

21

A numerical scheme based on the Vortex-Transport Element Method has been presented which is able to simulate finite as well as infinite reaction speed combustion of significant exothermicity in a post-transitional spacial shear layer.

Numerical results indicate that the presence of combustion heat release strongly modifies the flowfield and, in a forced layer, decreases the layer growth via an alteration of the interaction of the vortical structures from pairing for tearing. The reduced growth in conjunction with the reduced density within the mixing region leads to diminished mass of products formed.

Volumetric expansion resulting from the combustion heat release is seen to accelerate the flow in the streamwise direction. Baroclinic vorticity generation modifies the vorticity field in such a way that positive, counterclockwise vorticity appears at the outskirts of the vortical structures. The presence of this positive vorticity is related to overshoots an undershoots experienced by the the time averaged velocity profiles as well as to the triple peak nature of the Favre-averaged turbulent kinetic energy profiles. It is suggested that a more detailed understanding of the effects of combustion exothermicity on the flowfield can be obtained via a closer scrutiny of the mechanisms by which the combustion related density field interacts with the flow.

The infinite reaction speed model was found to represent an effective, computationally cost efficient approach in analyzing the effects of the combustion heat release on the flowfield as long as the reactions to be replaced by the model are fast compared to the flow.

REFERENCES

1. Hermanson, J.C. and Dimotakis, P.E., Journal of Fluid Mechanics, **199**, 333, (1989).

2. Brown, G.L. and Roshko, A.J., Journal of Fluid Mechanics, **64**, 775 (1974).

3. Keller, J.O., Ph.D. Thesis, University of California, Berkeley, CA, 1982.

4. Mungal, M.G. and Dimotakis, P.E., Journal of Fluid Mechanics, **148**, 349, (1984).

5. McMurtry, P.A., Jou, W.H., Riley, J.J. and Metcalfe, R.W., AIAA Journal, **24**, 962 (1986).

6. McMurtry, P.A., Riley, J.J. and Metcalfe, R.W. Journal of Fluid Mechanics, **199**, 297 (1989).

7. Ghoniem, A.F. and Krishnan, A., 22nd Symposium (International) on Combustion, The Combustion Institute, Pittsburgh PA, p665 (1988).

8. Ghoniem, A.F. and Givi, P., AIAA Journal, **26**, 690 (1988).

9. Ghoniem, A.F. and Heidarinejad, G., Combustion Science and Technology, **72**, 79 (1990).

10. Batchelor, G.K, An Introduction to Fluid Dynamics, Cambridge University Press, Cambridge, 1967.

11. Krishnan, A. and Ghoniem, A.F., Journal of Computational Physics, **99** (1992).

12. Hald, O.H., SIAM Journal of Numerical Analysis, **16**, 726 (1979).

13. Leonard, A., Journal of Computational Physics, **37**, 289 (1980).

14. Soteriou, M.C., Knio, O.M. and Ghoniem A.F., AIAA Paper 91-0081

15. Soteriou, M.C. and Ghoniem A.F., "Numerical Study of the Mechanisms of Shear Flow Modification by Combustion Related Density Variation", to be presented in 32nd Aerospace Sciences meeting, Januay 1994, Reno, NV.

16. Libby, P.A. and Williams, F.A., Turbulent Reacting Flows, Libby, P.A. and Williams, F.A. eds., Springer-Verlage, Berlin, p1, 1980.

17. Ghoniem, A.F. and Ng, K.K., Physics of Fluids, **30**, 706 (1987).
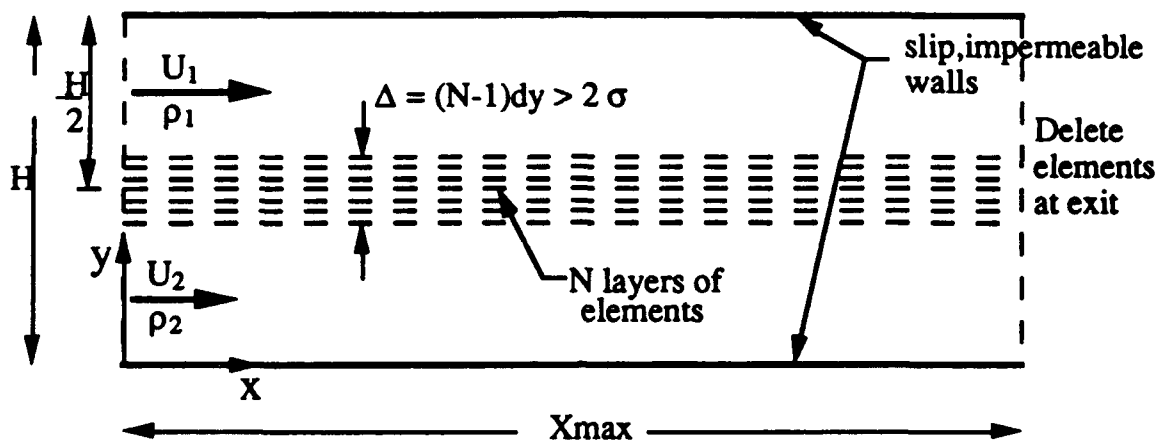
Figure 1. The geometry of the computational domain together with initial element configuration and some of the boundary conditions

(a)

Finite reaction speed inlet species profiles

(b)

Infinite reaction speed inlet species profiles
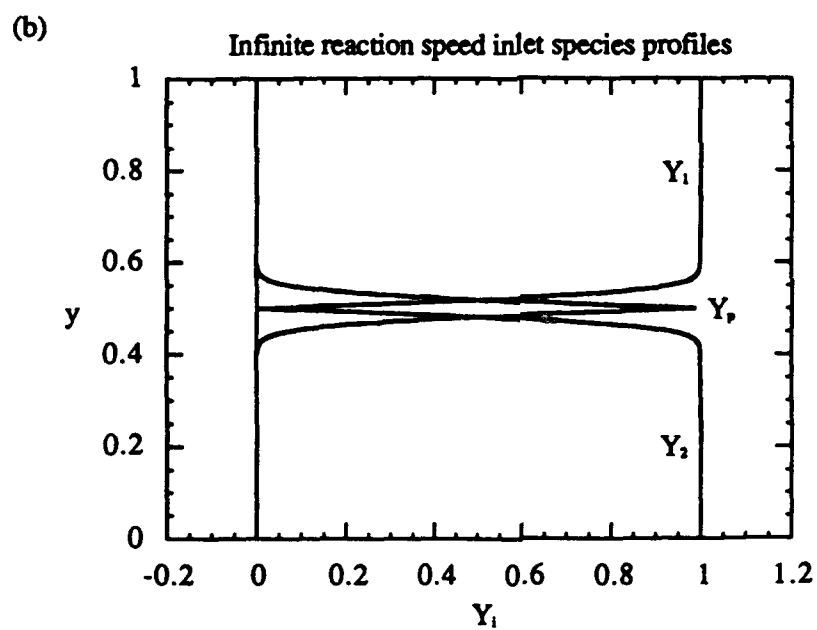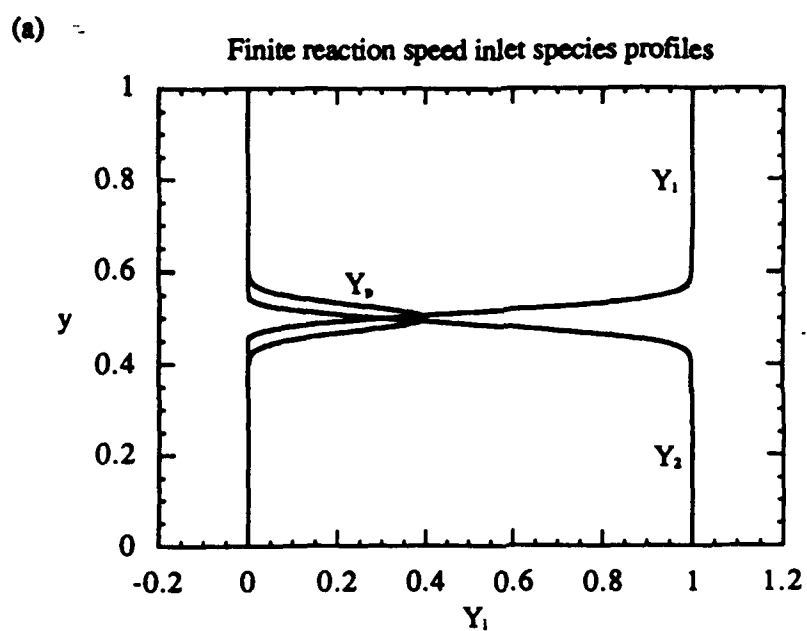
Figure 2. The inlet mass-fraction profiles for (a) the finite,
and (b) the infinite speed of reaction cases.
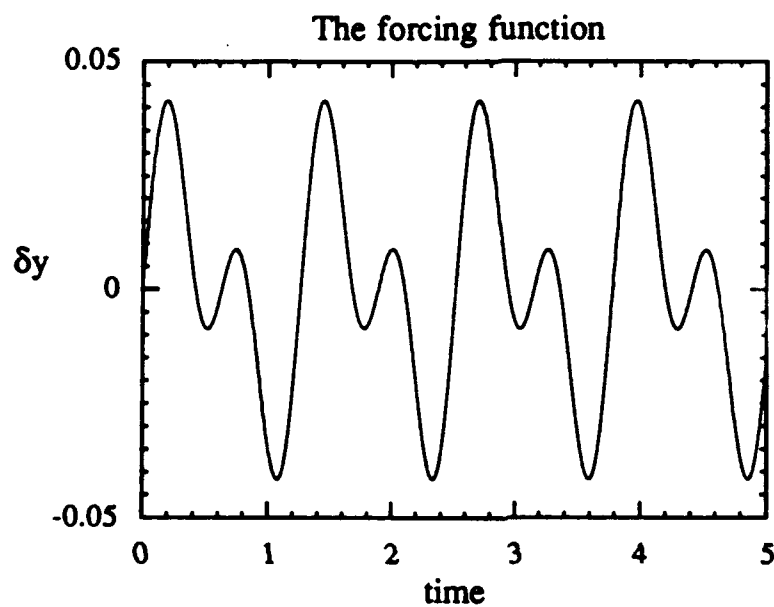
Figure 3. The forcing function used to destabilize the flow and to promote eddy interactions. It represents the cross-stream distance by which the elements are displaced at the inlet
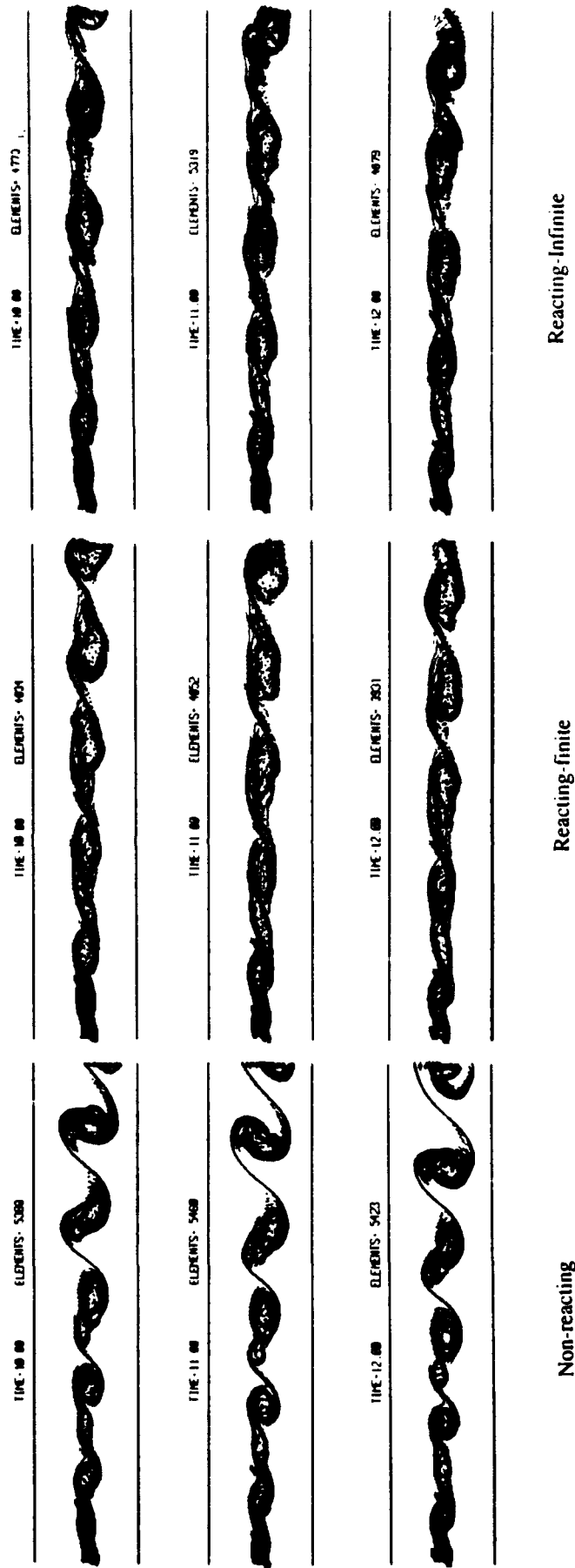
Figure 4 Flowfield comparison between the non-reacting (left) and reacting at finite (middle) and infinite (right) reaction speed shear layers. The layer is depicted using the vortex elements and their local velocity vectors. Three sequential time frames (increasing from top to bottom) are shown.
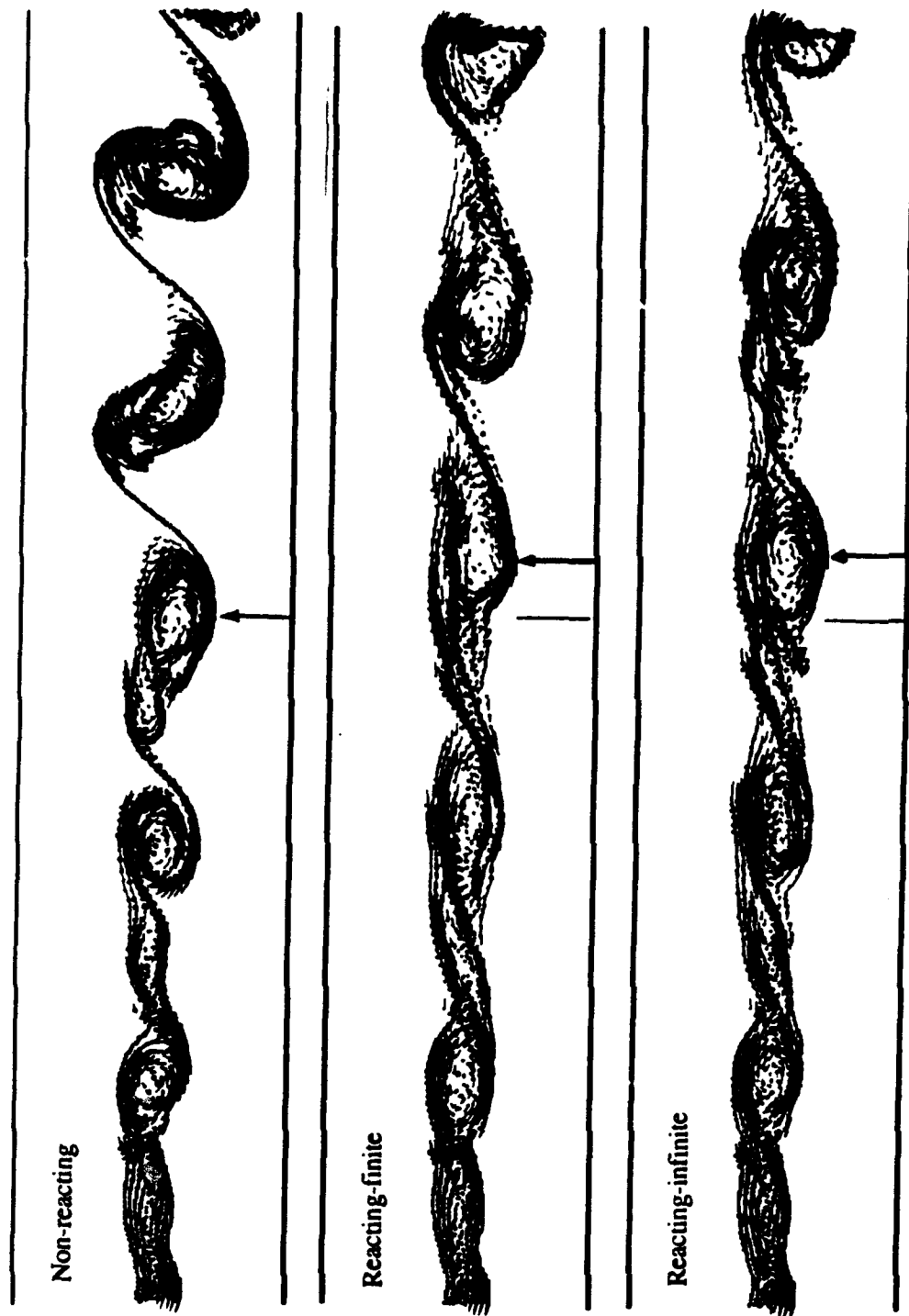
Figure 5. Flowfield comparison (vortex element plots) for non-reacting (top) and reacting at finite (middle) and infinite (bottom) reaction speed shear layers. The time is t=10.

(a)

Time-averaged velocity profiles

x	Non-reacting
o	Reacting-finite

(b)

Time-averaged velocity profiles

x	Non-reacting
o	Reacting-infinite
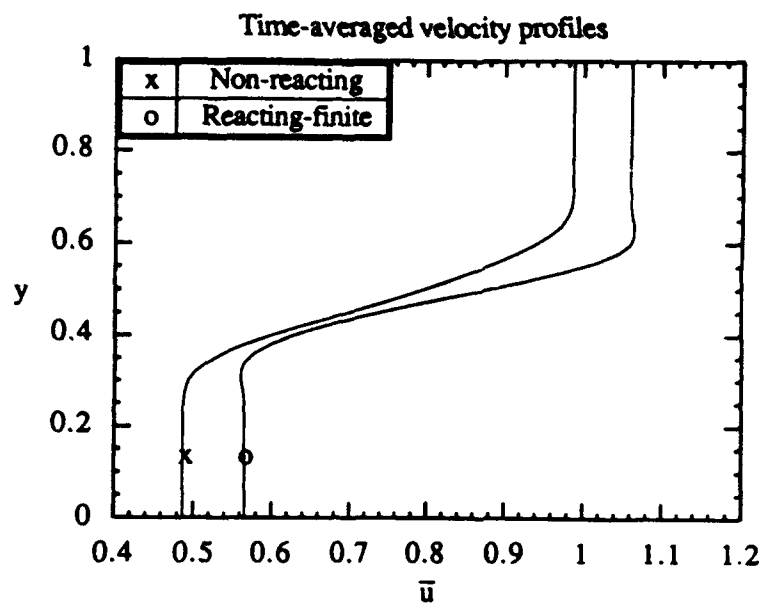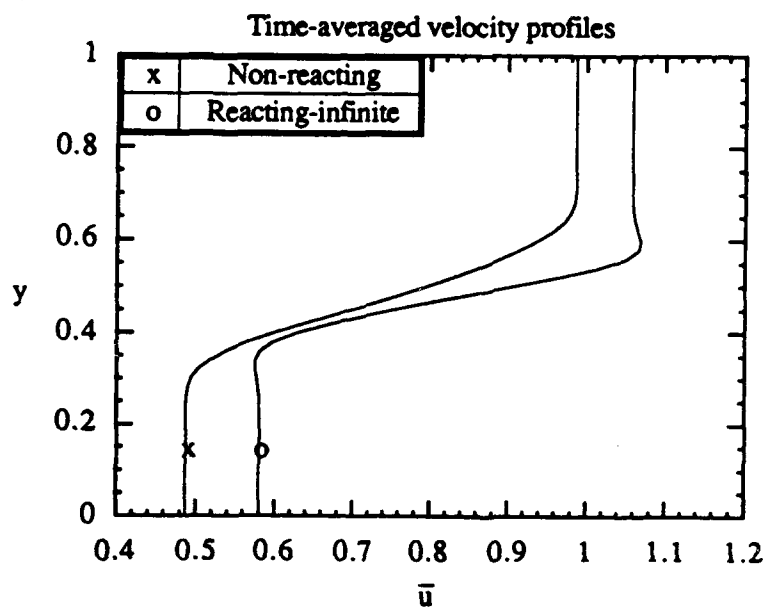
Figure 6. Comparison between the non-reacting and reacting time averaged velocity profiles for (a) the finite and (b) the infinite reaction speed cases. Streamwise location x=3
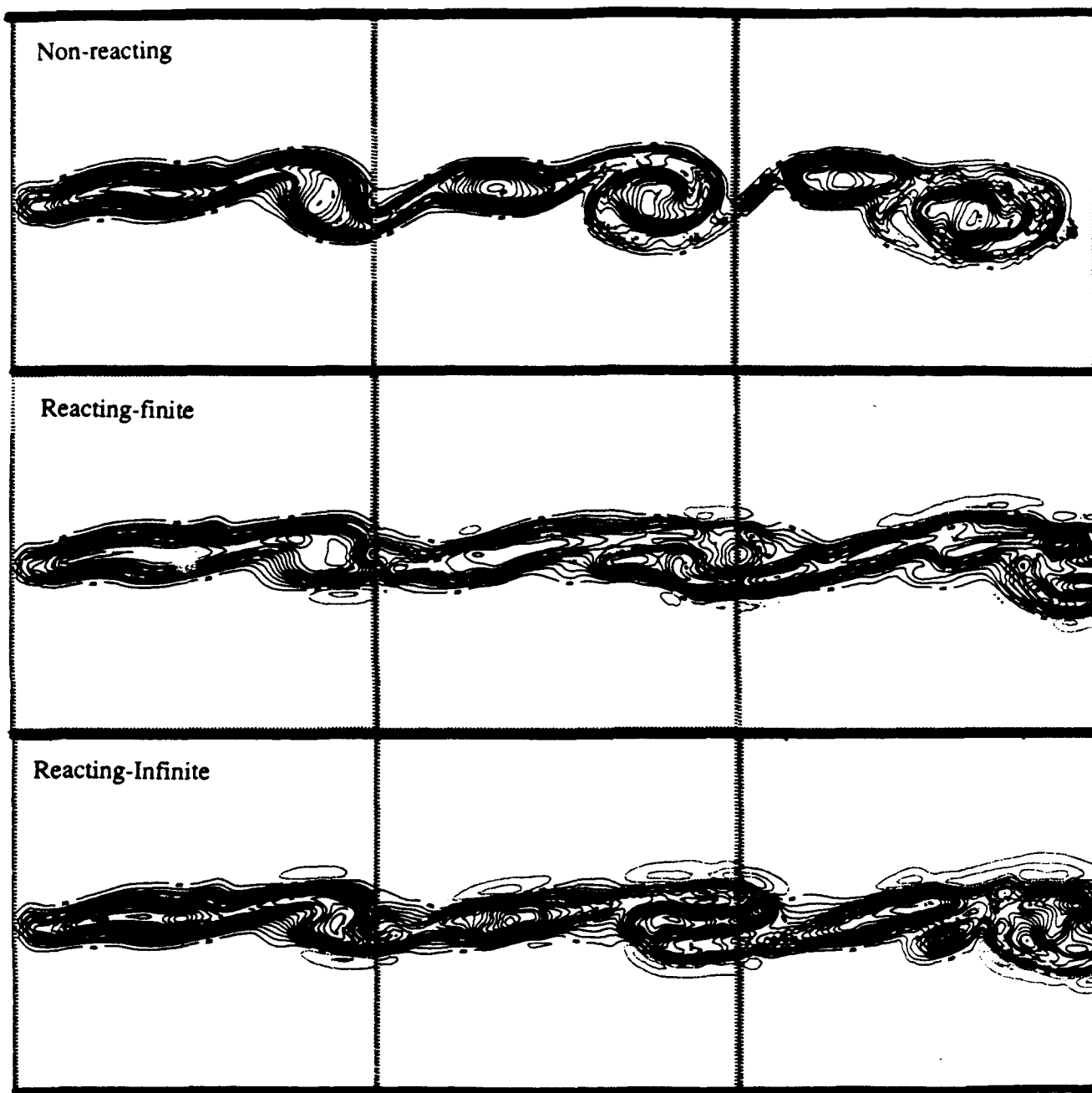
Figure 8. Vorticity contours comparison between the non-reacting (top) and reacting at finite (middle) and infinite (bottom) reaction speed shear layers. The time is t=10. 0<x<3 part of domain displayed.

(a)

(b)
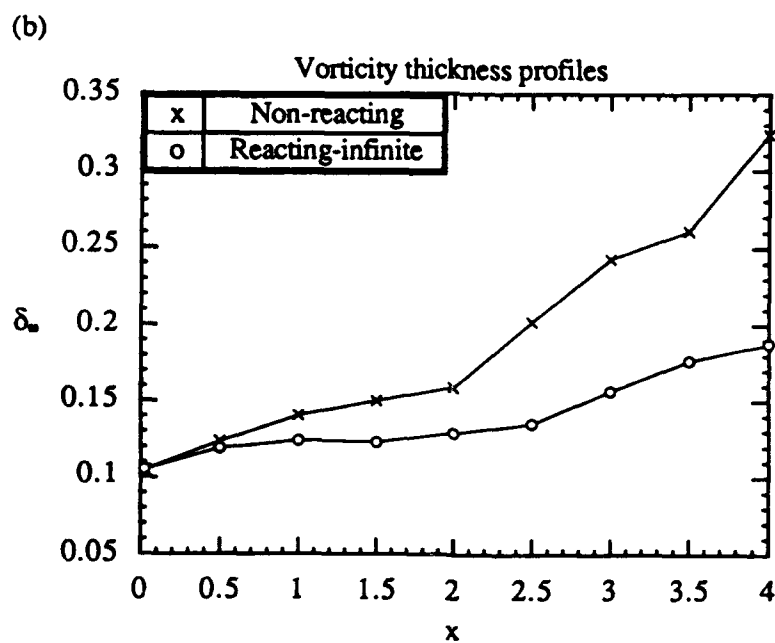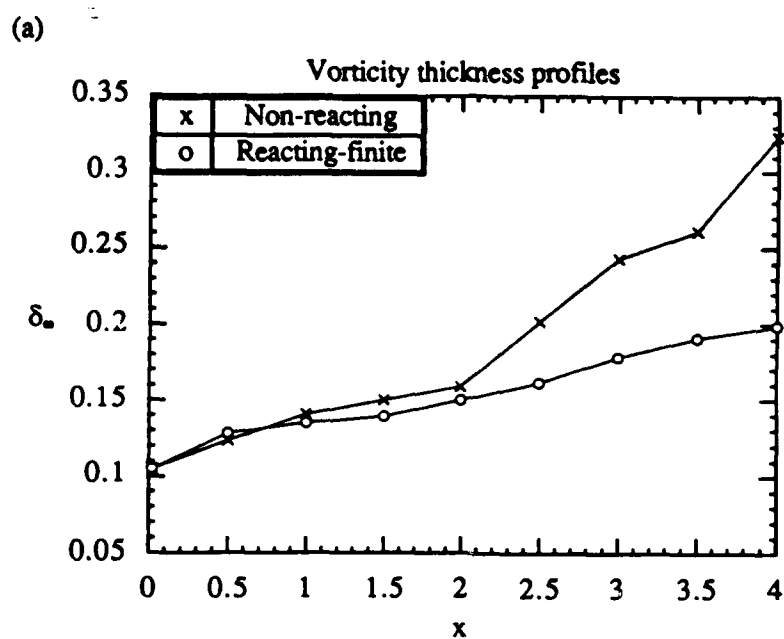
Figure 7. Comparison between the non-reacting and reacting vorticity thickness profiles for (a) the finite and (b) the infinite reaction speed cases.

(a)

Favre turbulent stress profiles

x	Non-reacting
Δ	Reacting-finite
+	Reacting-finite,ρ_{flow} uniform

$\overline{\rho u'' v''} \times 10^{-3}$

(b)

Favre turbulent stress profiles

x	Non-reacting
Δ	Reacting-infinite
+	Reacting-infinite,ρ_{flow} uniform

$\overline{\rho u'' v''} \times 10^{-3}$
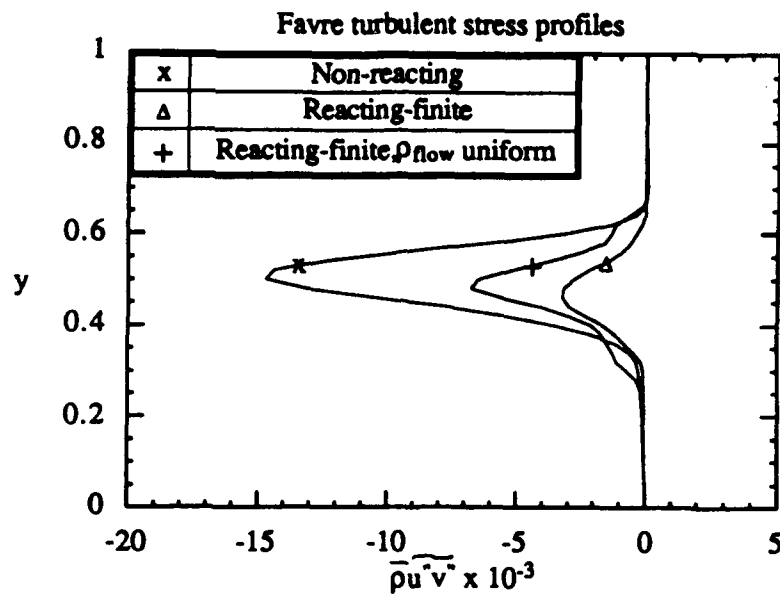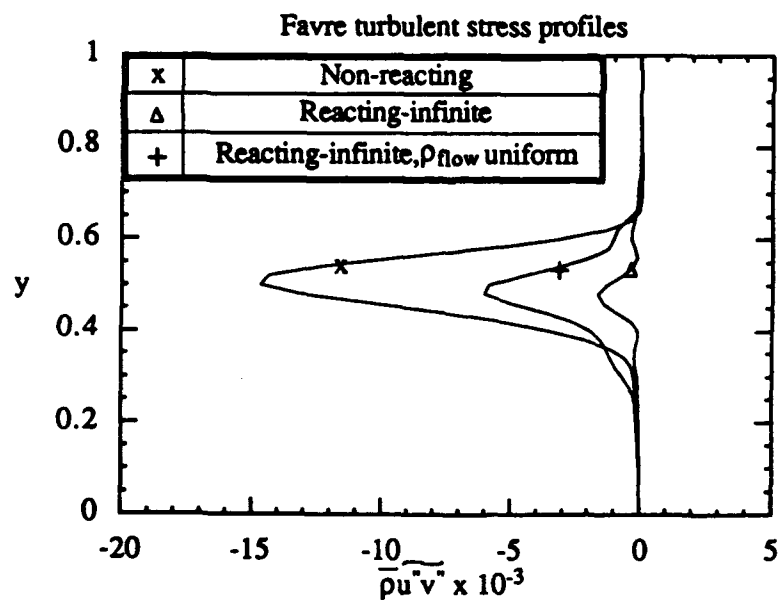
Figure 9. Comparison of the Favre turbulent stress profiles between the non-reacting, reacting, and reacting with uniform density imposed on the flow but not in the calculation of the stress. (a) is the finite and (b) the infinite reaction speed case. Streamwise location x=2.5

(a)

Favre turbulent kinetic energy profiles

x	Non-reacting
Δ	Reacting-finite
+	Reacting-finite, ρ_{flow} uniform

$KE \times 10^{-3}$

(b)

Favre turbulent kinetic energy profiles

x	Non-reacting
Δ	Reacting-infinite
+	Reacting-infinite, ρ_{flow} uniform

$KE \times 10^{-3}$
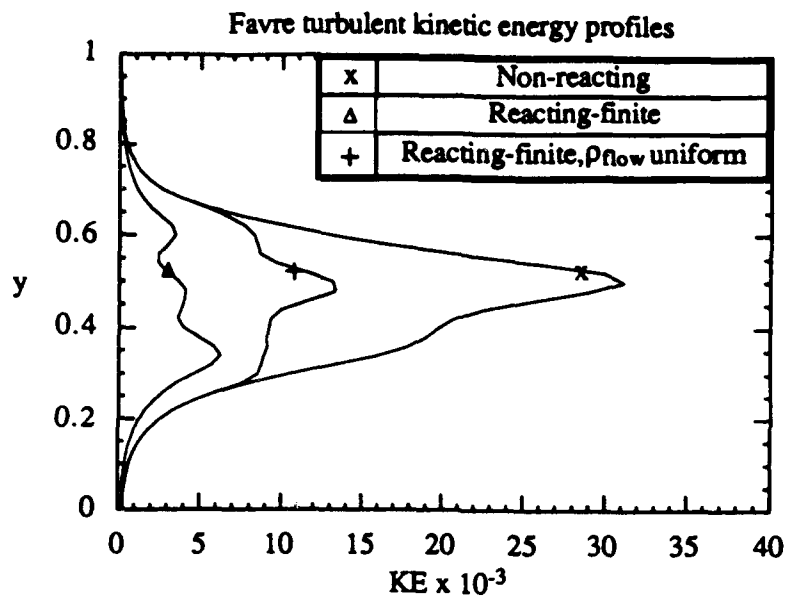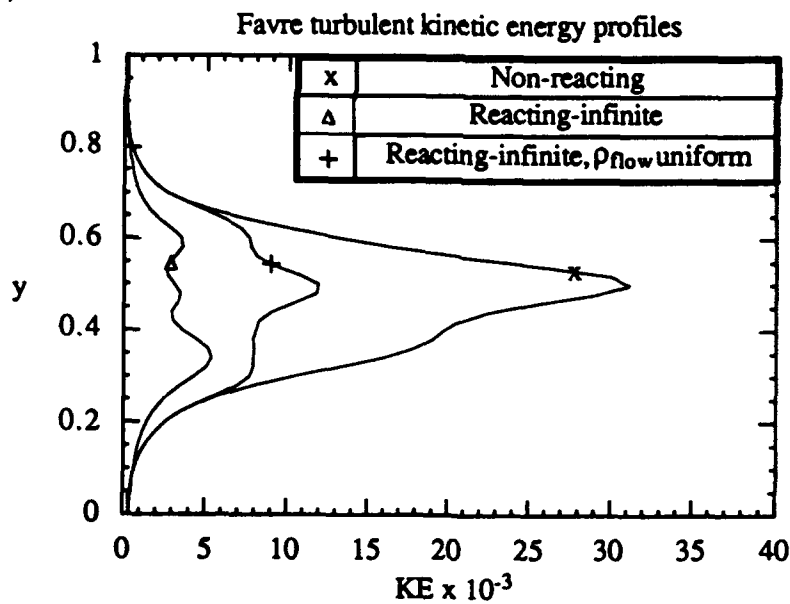
Figure 10. Comparison of the Favre turbulent kinetic energy profiles between the non-reacting, reacting, and reacting with uniform density imposed on the flow but not in the calculation of the stress. (a) is the finite and (b) the infinite reaction speed case. Streamwise location x=2.5
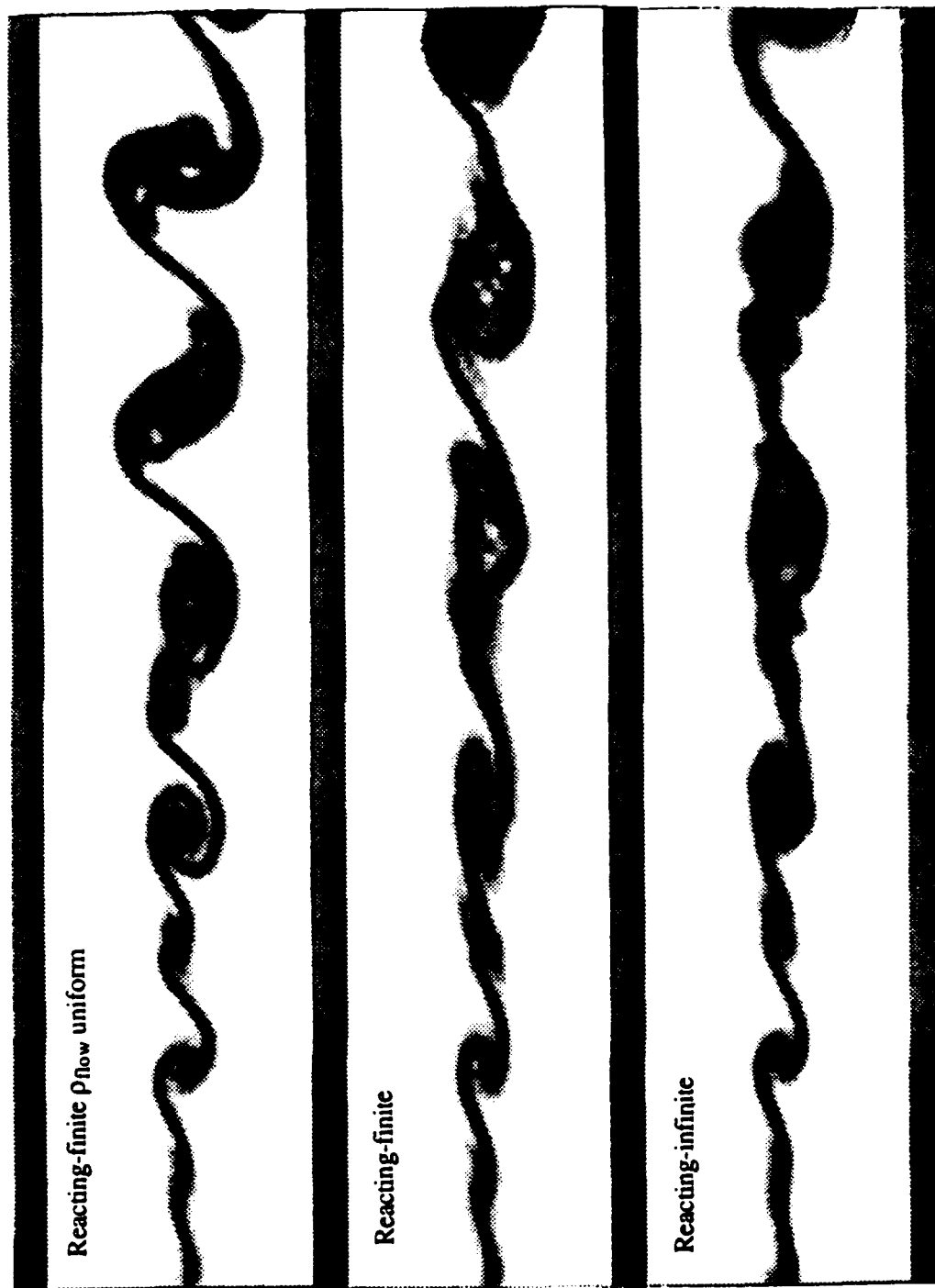
Figure 11. Comparison of product mass-fraction fields between the non-reacting (top) and reacting at finite (middle) and infinite (bottom) reaction speed shear layers. The time is t=10. Ten shade intensities (white to black) equally subdivide the plotting scale of $0 < Y_P < 1$.

(a)

Product thickness profiles

o	Reacting
ı	Reacting-finite,ρ_{flow} uniform
x	Reacting-finite,ρ uniform

δ_{p_r} vs x

(b)

Product thickness profiles

o	Reacting
ı	Reacting-infinite,ρ_{flow} uniform
x	Reacting-infinite,ρ uniform

δ_{p_r} vs x
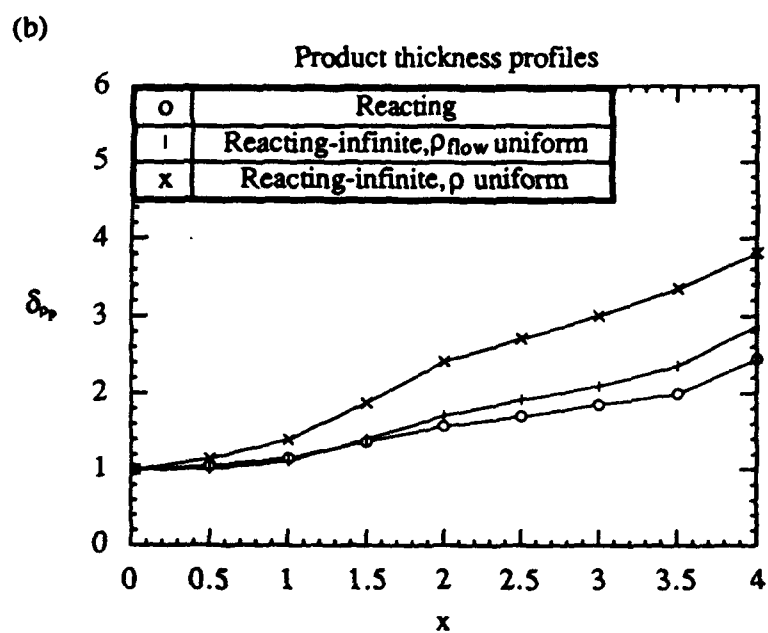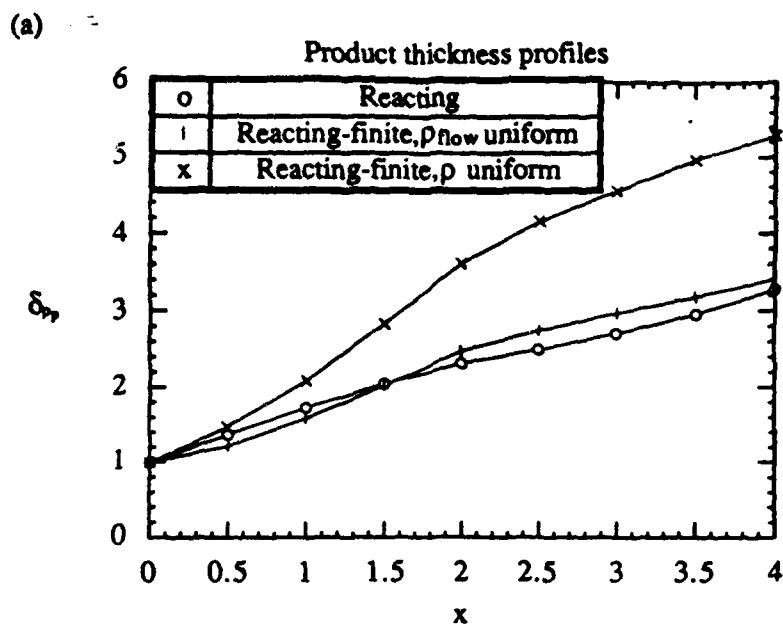
Figure 12. Comparison of the product thickness profiles between the reacting, reacting with uniform density imposed only on flow and reacting with uniform density cases for (a) finite reaction and (b) infinite reaction speeds.

APPENDIX II

Dynamics of Unsteady Strained Flame

Abstract

Transient response of flame to an unsteady strain rate is analyzed using a
series of mathematical transformations. Initially, the flame is located in the
stagnation plane. At time $t=0$ the unsteady strain rate is applied. Two basic
patterns of the strain rate are considered: a step function, and a sinus wave. Flame
response is characterized by two parameters: (1) burning velocity and, (2) flame
location. The influence of the Lewis number and the strain rate on these two
parameters and on the relaxation time is investigated. For unity Lewis number,
within the range of compressive strains characteristic for a turbulent jet flow (200
- 500 1/sec), the shapes of the temperature and mass fraction profiles remain
almost unchanged. This leads to the burning velocity that only slightly varies
with the strain rate. In the case of non-unity Lewis number the profiles are
significantly altered even by relatively weak strain rates. This happens due to the
interaction of unbalanced heat and concentration diffusion and convection. The
changes in the profiles produce significant variation in the burning velocity. Some
analytical results are obtained for the relaxation time of flame as a function of the
strain rate and thermo-chemical parameters. The analytical derivations are based on
the application of the integral approach in the transformed domain. In order to
investigate the receptivity characteristics of flame, the periodic strain rate is
applied. In the wide range of frequencies flame demonstrates periodic response.
The average value of the burning velocity is very close to the burning velocity of
flame under the average strain; phase shift between the burning velocity and strain
rate fluctuations is approximately constant and equal to -1.3π. This pattern is
violated only when the period of the strain rate oscillations is much lower than the
diffusion time scale. The analysis of the flame response suggests that the steady
state assumption can be used with a reasonable accuracy in a flamelet modeling,
although the phase shift should be taken into account. Extinction strain rate which
we define as the strain rate when the steady state flame location crosses the
stagnation plane for the first time, is an exponential function of the heat release.
This suggests that, in order to get adequate values of the extinction strain using a

simplified chemical kinetics mechanism, one should pay particular attention to the chemical reactions which maintain the energetic balance of the system.

Nomenclature

k - pre-exponential factor

c_p - specific heat of mixture at constant pressure in J/kg K

λ - thermal conductivity of mixture in W/ m K

ρ - mixture density kg/ m^3

ε - strain rate of the flow in 1/s

U - velocity of the imposed stagnation point flow in m/s

u' - velocity induced by the density drop at the reaction front

Y_{ox}, Y_n, Y_f - mass fractions of oxidizer, dilutant and fuel

C_{ox}, C_n, C_f - molar concentrations of oxidizer, dilutant and fuel in mole/ m^3

T - thermodynamic temperature in K

x - physical coordinate normal to the flame front in m

Q - heat release per mole of fuel in J/ mole

$\dot{W}$ - reaction rate in mole/ m^3 s

R_u - universal gas constant

E_a/R_u - activation temperature, in K

p - pressure in Pa

H - enthalpy of mixture in J/ kg

W_{ox}, W_n, W_f - molecular weights of oxidizer, dilutant and fuel in kg/ mole

W_{mix} - molecular weight of mixture in kg/mole

m - laminar flame eigenvalue

μ - non-dimensional heat release

Z_e - Zeldovich number

u_n - laminar steady flame velocity

θ - non-dimensional temperature

η - position coordinate in the transformed domain, non-dimensional

$\Delta_\theta, \Delta_Y, \Delta_r$ - thicknesses of the temperature, mass fraction and reaction rate profiles, respectively, in the transformed domain, non-dimensional

o - subscript denoting values in the cold mixture far ahead of the flame

b - subscript denoting values in the products region far behind the flame

$*$ - subscript denoting characteristic values

Introduction

A lot of attention in the last decade has been paid to the investigation of flame located in the stagnation point flow. It was due to the relative simplicity of the configuration, an opportunity to study flame/ flow interaction and to compare the numerical results with the experiment. This configuration is interesting not only from the fundamental point of view, but also it might be used in the modeling of a turbulent combustion flow. The idea is to split the flame front in a turbulent flow into a collection of small planar flamelets. Each of these flamelets propagates into the unburned mixture with the velocity dependent on the local parameters (effective flow strain rate etc.). Combustion affects the flow field mainly through the change in density near the reaction front and through the heat release. These characteristics depend on the amount of fuel consumed in the flame. The effect of flow on the flame manifests itself primarily through the increase of flame area which is characterized by a parameter called stretch (Law C. K. 1988). This characteristic has two components: due to the strain rate and due to the flame curvature. Study of flame in a stagnation point flow helps to understand the influence of the strain rate on flame characteristics, while the effect of curvature is accounted for on the global level considering the flame front as a collection of small planar flamelets.

Previous studies (Law C.K. 1988) demonstrated that in a *unity Lewis number* mixture and in the range of strain rates typical for turbulent flows (< 1000 1/sec.) the flame structure and burning velocity are almost unaffected by the strain rate and conserve the values corresponding to the unstrained flame. This leads to the suggestion that only the evolution of the flame area should be tracked in a turbulent combustion flow while the burning rate should be kept constant and equal to the unstrained flame burning rate (Meneveau C. et. al. 1991).

In this paper we are studying a flame in *non-unity Lewis number* mixture. Interaction of the unbalanced heat and concentration fluxes with the strain rate could have a profound effect on the burning velocity. In many cases this characteristic of flame can not be assumed to be equal to the unstrained value. We utilize numerical calculations to study the response of flame to the different patterns of the strain rate. We are interested in the range of strain rates typical for a turbulent flow and not considering rates much higher than the partial extinction strain (Darabiha et. al. 1986) when the steady state location of flame is crossing the stagnation plane for the first time.

Another important assumption that is usually made in turbulent combustion flow simulations is the instantaneous response of flame to the strain rate fluctuations. In many papers it has been pointed out that this assumption is very crude (Rutland 1990) and a transient model should be applied in a turbulent flow simulation. In this paper we are investigating the receptivity of flame to the strain rate fluctuations. The measure of receptivity is the ratio of the averaged burning rate to the burning rate under the averaged strain. If this ratio is equal or close to one in a realistic range of strains then the steady state assumption can be safely used although the correction on the delay of the burning velocity fluctuations should be made. We found that in a practically important range of strain rate frequencies the flame demonstrates good receptivity. Thus, for engineering purposes, the steady state assumption can be used.

In Chapter 1 steady and unsteady problems are formulated and the solution procedures for both of them are described in detail. Solution of the steady problem is used to initialize the unsteady problem. An approach by Zeldovich (1985) is applied. Solution of the unsteady problem is based on the method described by Rutland (1990). This approach is extended to include the non-unity Lewis number case. In Chapter 2 an integral method is developed in order to obtain the functional dependence of the flame response time on the thermo-chemical and flow parameters. The idea of the method is to apply the regular integral approach in the transformed domain where the governing equations have a simple form and to use an assumption that the ratio of the heat zone thickness to the mass fraction zone thickness is a weak function of time. In Chapter 3 a numerical procedure used to solve the unsteady problem is described in detail. In Chapter 4 we discuss the results of calculations obtained using a set of Lewis numbers and typical thermo-chemical parameters . Chapter 5 contains conclusions.

1. Formulation

In this paper a plane flame is located in the stagnation point flow produced by two colliding jets of reactants and products (Figure 1). X-axis is directed

perpendicular to the flame, y-axis - along the flame. We assume that the externally imposed stagnation point flow is inviscid and irrotational. The distribution of the x-velocity component in this flow is given by the following equation

$$U(x) = - \varepsilon(t) \, x \qquad (1)$$

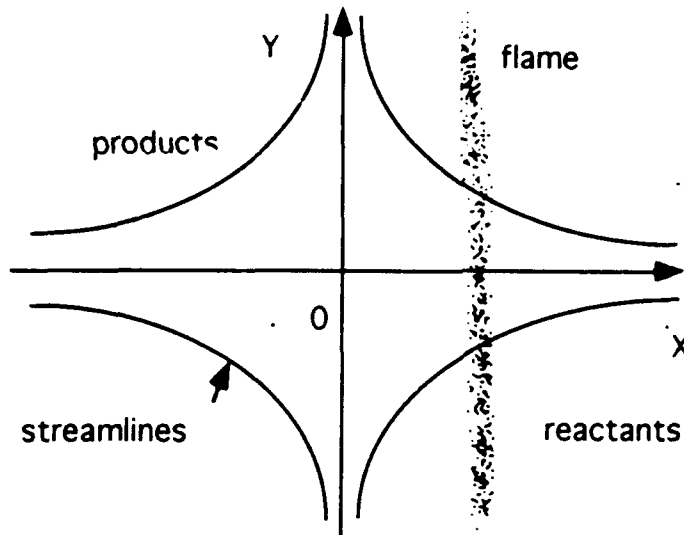In this expression ε is the diagonal component of the strain rate tensor.

Figure1 Flame located in the stagnation point flow

Also, we assume that the strain rate ε is a function of time.

Initialization

Initial temperature and deficient mass fraction profiles are obtained by solving the problem of steady propagating premixed flame. The flame propagation is governed by the following set of equations:
Continuity:

$$\frac{d}{dx} (\rho u) = 0 \qquad (2)$$

Enthalpy:

$$\rho u \frac{dH}{dx} = \frac{d}{dx} (\frac{\lambda}{c_p} \frac{dH}{dx}) + Q \, \dot{W}(Y, H) \qquad (3)$$

Deficient mass fraction:

5

$$\rho u \frac{dY}{dx} = \frac{d}{dx}(\rho D \frac{dY}{dx}) - W_f \ W(Y, H) \tag{4}$$

Equation of state:

$$p = \rho R_u T/W_{mix} \tag{5}$$

In this problem one-step chemical kinetics mechanism is assumed. Our numerical simulations using full-scale chemical kinetics mechanism demonstrate that the bulk details of the flame/ flow interactions can be described using a simple chemistry mechanism.

Reaction rate:

$$\dot{W} = k \, C_{ox} \, C_f \, exp(-E_a/RT) \tag{6}$$

In this paper we assume that fuel is deficient. The concentration of the oxidizer is almost constant and equal to the initial concentration:

$$C_{ox} \cong C_{ox}^o$$

Using the relationship between the mass fraction of fuel and its concentration, we can rewrite reaction rate expression as follows:

$$\dot{W} = \frac{k \, C_{ox}^o}{W_f} \rho \, Y_f \, exp(-E_a/RT) \tag{7}$$

Boundary conditions for these equations are:

$$x = -\infty \quad H = H_0, \quad x = +\infty \quad H = H_b, \quad dH/dx = 0 \quad \text{and}$$

$$x = -\infty \quad Y = Y_f^{\ o}, \quad x = +\infty \quad Y = 0 \tag{8}$$

Since two second order ODE have five boundary conditions, one of the parameters of the problem, namely mass flux per unit area ρu can not be specified independently and is becoming an eigenvalue.

First, the continuity equation is solved. The result of integration is:

$$\rho(x) \, u(x) = \rho_o \, u_n = const$$

It means that the mass flux per unit area is constant along the axis perpendicular to the flame front in a steady propagating flame. Introduction of the following new variables (Zeldovich et. al. 1985) reduces the order of the system:

$$\theta = \frac{H-H_0}{H_b-H_0} \qquad y = \frac{\lambda}{c_p} \left[Q \, (H_b-H_0) \, (\dot{W}\frac{\lambda}{c_p})_* \right]^{-1/2} \frac{dH}{dx} \tag{9}$$

$$m = \rho_o \, u_n \left[\frac{Q}{H_b-H_0} \, (\dot{W}\frac{\lambda}{c_p})_* \right]^{-1/2} \tag{10}$$

Here θ is reduced temperature, y is non-dimensional heat flux. m is non-dimensional mass flux, an eigenvalue. Subscript * denotes characteristic values of the parameters. We have used

$$\lambda_* = \lambda_o, \quad c_{p,*} = c_{p,o} = const \qquad \dot{W}_* = \frac{k \, C_{ox}^o}{W_f} \rho_o \, Y_f^{\ o} \, exp(-E_a/RT_b)$$

Enthalpy equation written in terms of the new variables takes the form:

$$y \frac{dy}{d\theta} - m y + \varphi(\theta) = 0 \qquad (11)$$

Here $\varphi(\theta)$ is defined as:

$$\varphi(\theta) = (W\lambda/c_p)/(W\lambda/c_p)_. = \frac{\lambda}{\lambda_o} \frac{c_{po}}{c_p} \overline{Y_f} exp(Z_e (\theta-1)/(1+\mu(\theta-1)))$$

and $Z_e = \frac{E}{RT_b^2}(T_b{-}T_0)$ is Zeldovich number, $\mu = \frac{T_b - T_0}{T_b}$ is non-dimensional heat release, $\overline{Y_f} = Y_f/ Y_f{}^o$ is non-dimensional mass fraction of the fuel. Another equation can be obtained by multiplying original enthalpy equation by W_f, original mass fraction equation - by Q, adding them together and integrating the resulting equation. This operation results in equation

$$\rho u (W_f (H - H_b) + Q Y) = \frac{\lambda}{c_p} W_f \frac{dH}{dx} + \rho D Q \frac{dY}{dx} \qquad (12)$$

which can be transformed into

$$m (\theta - 1 + \overline{Y}) = y + \frac{y}{L_e} \frac{d\overline{Y}}{d\theta}, \quad L_e = \frac{\lambda}{\rho c_p D} \qquad (13)$$

Here L_e is Lewis number. Boundary conditions are

$$@\theta = 0 \; y = 0 \;\; \overline{Y} = 1 \;; \;\; @\theta = 1 \; y = 0 \;\;\; \overline{Y} = 0 \qquad (14)$$

Equations for reduced temperature (11) and mass fraction (13) are solved numerically using damped Newton algorithm and a shooting procedure. Runge-Kutta integration starts from the hot side of the flame. The initial values of the derivatives at this point are obtained by approximating the functions y and $\overline{Y}$ using the first terms in the corresponding Taylor expansions:

$$y = k_1 (1-\theta) \quad \overline{Y} = k_2 (1-\theta)$$

and substituting these expressions into the governing equations to find the values of k_1 and k_2.:

$$\frac{dy}{d\theta} (\theta = 1) = - k_1 = \frac{m L_e}{2} \left[1 - \sqrt{1 + \frac{4}{m^2 L_e}} \right]$$

$$\frac{d\overline{Y}}{d\theta} (\theta = 1) = - k_2 = - \left((k_1)^2 + m k_1\right)$$

The Runge-Kutta integration proceeds up to the point where non-dimensional reaction rate function $\varphi(\theta)$ is equal to zero (reduced ignition temperature). At this point the numerical value of the heat flux y is compared with the analytical solution of equation (11) for y where $\varphi(\theta)$ is put to zero and a correction to the eigenvalue m is made. The integration continues up to the point where the analytical and numerical solutions match. The equation for the mass fraction is satisfied automatically (Zeldovich et. al. 1985). Once the solutions for $y(\theta)$ and

7

$\overline{Y}(\theta)$ are obtained, the temperature profile in the real domain is recalculated using the definition of the non-dimensional heat flux y:

$$ x_i = \sqrt{\lambda_b/(k\ C_{ox}\ exp(-E_a/RT_b)\ c_p\ \rho_o)} \int_o^{\eta_i} (\mu\theta/(1-\mu)+1)d\theta/y(\theta) \qquad (15) $$

Solution of the unsteady problem

The reduced temperature and mass fraction profiles obtained from the solution of the steady problem are used as initial profiles for the solution of the unsteady problem. Transient dynamics of one-dimensional flame is governed by the following set of unsteady equations:

Continuity
$$ \frac{\partial \rho}{\partial t} + \frac{\partial(\rho u)}{\partial x} = 0 \qquad (16) $$

Mass Fraction
$$ \rho\frac{\partial Y}{\partial t} + \rho u\frac{\partial Y}{\partial x} = \frac{\partial}{\partial x}\left(\rho\ D\ \frac{\partial Y}{\partial x}\right) - \dot{W}(Y, T)\ W_f \qquad (17) $$

Enthalpy
$$ \rho\ c_p\ \frac{\partial T}{\partial t} + \rho\ u\ c_p\ \frac{\partial T}{\partial x} = \frac{\partial}{\partial x}\left(\lambda\frac{\partial T}{\partial x}\right) + Q\ \dot{W}(Y, T) \qquad (18) $$

Also, the same equation of state (5) and reaction rate expression (7) are used.

Boundary conditions:
$$ @\ x = -\infty\ Y = Y_0, T = T_0,\ @\ x = +\infty\ \ Y = 0, T = T_b \qquad ,\ (19) $$
Subscript 0 denotes the values of the mass fraction and enthalpy in the cold mixture.

In this paper we adopted an approach of C. Rutland (1990). Stagnation point flow $U(x)$ is externally imposed on the flame. Due to combustion, a drop in density occurs in the flame zone. This density change induces a velocity component $u'(x)$. This velocity perturbation vanishes far away from the flame zone and is non-zero in its vicinity. The x-component of the total velocity can be approximated as
$$ u(x) = U(x) + u'(x). $$
Also, the following boundary layer approximations can be made :

8

$$\frac{\partial}{\partial x} >> \frac{\partial}{\partial y}; \frac{\partial}{\partial z}$$

The density drop in the flame occurs mainly along the x-axis. Hence

$$u'(x) >> v', w'$$

Here v' and w' are perturbations of the velocity field in y and z directions, respectively. Using these assumptions, we can rewrite equations (16), (17) and (18) as follows:

$$\frac{\partial \rho}{\partial t} + U(x)\frac{\partial(\rho)}{\partial x} + \frac{\partial(\rho u')}{\partial x} = 0 \tag{20}$$

$$\rho \frac{\partial Y}{\partial t} + \rho (U+u') \frac{\partial Y}{\partial x} = \frac{\partial}{\partial x}\left(\rho D \frac{\partial Y}{\partial x}\right) - \dot{W}(Y, T) W_f \tag{21}$$

$$\rho c_p \frac{\partial T}{\partial t} + \rho c_p (U+u') \frac{\partial T}{\partial x} = \frac{\partial}{\partial x}\left(\lambda \frac{\partial T}{\partial x}\right) + Q \dot{W}(Y, T) \tag{22}$$

These equations are simplified and translated into a system of reaction-diffusion equations using two transformations. The main ideas behind the transformations are described in detail by Rutland (1990) for the premixed flames and by A.Ghoniem and M. Soteriou (1992) for the diffusion flames.

First, the unsteady equations are non-dimensionalized. In the following subscript 's' denotes some characteristic scale value, bar on the top of a variable means that the variable is non-dimensional. The non-dimensional governing equations are:

$$\frac{\partial \overline{\rho}}{\partial \overline{t}} + \frac{t_s u_s}{x_s} \overline{U}(x) \frac{\partial(\overline{\rho})}{\partial \overline{x}} + \frac{t_s u_s}{x_s} \frac{\partial(\overline{\rho u'})}{\partial \overline{x}} = 0$$

$$\frac{\partial \overline{Y}}{\partial \overline{t}} + u_s (\overline{U}+\overline{u'}) \frac{t_s}{x_s} \frac{\partial \overline{Y}}{\partial \overline{x}} = \frac{t_s}{x_s^2} \frac{1}{\rho} \frac{\partial}{\partial \overline{x}}\left(\rho D \frac{\partial \overline{Y}}{\partial \overline{x}}\right) - \frac{t_s}{\rho Y_s} \dot{W}(\overline{Y}, \overline{T}) W_f$$

$$\frac{\partial \overline{T}}{\partial \overline{t}} + u_s (\overline{U}+\overline{u'}) \frac{t_s}{x_s} \frac{\partial \overline{T}}{\partial \overline{x}} = \frac{t_s}{x_s^2} \frac{1}{\rho_s \overline{\rho}} \frac{\partial}{\partial \overline{x}}\left(\frac{\lambda}{c_p} \frac{\partial \overline{T}}{\partial \overline{x}}\right) + \frac{t_s}{\rho_s \overline{\rho}} \frac{Q}{c_p T_s} \dot{W}(\overline{Y}, \overline{T})$$

The first transformation $(\overline{t}, \overline{x}) \rightarrow (\widetilde{t}, \widetilde{x})$

$$\widetilde{t} = \overline{t}, \ \widetilde{x} = \left[exp\left(\int_0^{\overline{t}} \varepsilon(t') dt'\right)\right] \overline{x} \tag{23}$$

translates the non-dimensional equations into a domain moving the applied strain rate:

$$\frac{\partial \overline{\rho}}{\partial \widetilde{t}} + \frac{t_s u_s}{x_s} B(\overline{t}) \frac{\partial(\overline{\rho u'})}{\partial \widetilde{x}} = 0$$

9

$$\frac{\partial \overline{Y}}{\partial t} + u_* \overline{u'} \frac{t_*}{x_*} B(t) \frac{\partial \overline{Y}}{\partial \widetilde{x}} = \frac{t_*}{x_*^2} \frac{1}{\rho} B^2(t) \frac{\partial}{\partial \widetilde{x}}\left(\rho D \frac{\partial \overline{Y}}{\partial \widetilde{x}}\right) - \frac{t_*}{\rho Y_*} \dot{W}(\overline{Y}, \overline{T}) W_f$$

$$\frac{\partial \overline{T}}{\partial t} + u_* \overline{u'} B(t) \frac{t_*}{x_*} \frac{\partial \overline{T}}{\partial \widetilde{x}} = \frac{t_*}{x_*^2} \frac{B^2(t)}{\rho_* \overline{\rho}} \frac{\partial}{\partial \widetilde{x}}\left(\frac{\lambda}{c_p} \frac{\partial \overline{T}}{\partial \widetilde{x}}\right) + \frac{t_*}{\rho_* \overline{\rho}} \frac{Q}{c_p T_*} \dot{W}(\overline{Y}, \overline{T})$$

The part of the convective term related to the imposed velocity $U(x)$ is eliminated in the $(t, \widetilde{x})$ domain. The next (Howarth) transformation is used to eliminate the part of the convective term which contains velocity u' .

To apply the Howarth transformation, we integrate continuity equation with respect to $\widetilde{x}$ from $-\infty$ to $\widetilde{x}$ and take into account that on the products side, far away from the flame $u'(-\infty) = 0$.
The result of the integration is

$$\int_{-\infty}^{\widetilde{x}} \frac{\partial \overline{\rho}}{\partial t} d\widetilde{x'} + \frac{t_* u_*}{x_*} B(t) \, (\overline{\rho u'}) = 0 . \tag{24}$$

Second (Howarth) transformation $(\widetilde{t}, \widetilde{x}) \rightarrow (\hat{t}, \eta)$ is defined as:

$$\eta = \int_{-\infty}^{\widetilde{x}} \overline{\rho} \, d\widetilde{x'}, \qquad \hat{t} = \widetilde{t} \tag{25}$$

Application of the second transformation and equation (24) translates mass fraction and temperature equations as follows:

$$\frac{\partial \overline{Y}}{\partial \hat{t}} = \frac{t_*}{x_*^2} B^2(t) \frac{1}{\rho_*} \frac{\partial}{\partial \eta}\left(\overline{\rho} \rho D \frac{\partial \overline{Y}}{\partial \eta}\right) - \frac{t_*}{\rho Y_*} \dot{W}(\overline{Y}, \overline{T}) W_f \tag{26}$$

$$\frac{\partial \overline{T}}{\partial \hat{t}} = \frac{t_*}{x_*^2} \frac{B^2(t)}{\rho_*} \frac{\partial}{\partial \eta}\left(\frac{\lambda}{c_p} \overline{\rho} \frac{\partial \overline{T}}{\partial \eta}\right) + \frac{t_*}{\rho} \frac{Q}{c_p T_*} \dot{W}(\overline{Y}, \overline{T}) \tag{27}$$

We can make further simplification, assuming that $\lambda(x) \rho(x) = const$
Now we can rewrite equations (26-27) as:

$$\frac{\partial \overline{T}}{\partial \hat{t}} = \frac{t_*}{x_*^2} \alpha_* B^2(t) \frac{\partial}{\partial \eta}\left(\frac{\partial \overline{T}}{\partial \eta}\right) + \frac{t_*}{\rho} \frac{Q}{c_p T_*} \dot{W}(\overline{Y}, \overline{T}), \quad \alpha_* \equiv \frac{\lambda_*}{c_p \rho_*} \tag{28}$$

$$\frac{\partial \overline{Y}}{\partial \hat{t}} = \frac{t_*}{x_*^2} \alpha_* B^2(t) \frac{\partial}{\partial \eta}\left(\frac{1}{L_e(\eta)} \frac{\partial \overline{Y}}{\partial \eta}\right) - \frac{t_*}{\rho Y_*} \dot{W}(\overline{Y}, \overline{T}) W_f, \quad L_e \equiv \frac{\alpha}{D} \tag{29}$$

The convective terms are absent in the $(\hat{t}, \eta)$ domain.
Chemical time scale is used as the time scale of the problem and heat diffusion length scale is utilized as the length scale of the problem :

$$t_* = C_f^o \, /W(Y_f^o, T_b) \quad x_* = \sqrt{\alpha_0 \, t_{flow}} = \sqrt{\alpha_0 / |\varepsilon|} , \quad C_0 = \rho_0 Y_f^o /W_f$$

Initial mass fraction of fuel Y^0 scales mass fraction; the difference between the flame and 'cold' temperatures scales temperature $T_f = T_b - T_0$. Then equations (28) and (29) are rewritten in terms of the following reduced variables:

$$\bar{Y} = \frac{Y}{Y_0}, \quad \bar{T} = \theta = \frac{T - T_0}{T_b - T_0}$$

and have the form

$$\frac{\partial \theta}{\partial \hat{t}} = Ka\, B^2(t)\frac{\partial}{\partial \eta}\left(\frac{\partial \theta}{\partial \eta}\right) + \frac{\rho_0}{\rho}\frac{\dot{W}(\bar{Y}, \theta)}{\dot{W}(1, 1)}, \quad Ka = t_{chem}\,|\varepsilon| \tag{30}$$

$$\frac{\partial \bar{Y}}{\partial \hat{t}} = Ka\, B^2(t)\frac{\partial}{\partial \eta}\left(\frac{1}{Le(\eta)}\frac{\partial \bar{Y}}{\partial \eta}\right) - \frac{\rho_0}{\rho}\frac{\dot{W}(\bar{Y}, \theta)}{\dot{W}(1, 1)} \tag{31}$$

Here we introduced Karlovitz number to measure the strain rate and used energy conservation equation $W_f(H_b - H_0) = Q\, Y_f^0$ which can be derived from equation (12). Boundary conditions are:

$$@\eta = 0 \quad \bar{Y} = 0,\ \theta = 1\ ; \quad @\eta = +\infty \quad \bar{Y} = 1,\ \theta = 0 \tag{32}$$

Expression for the non-dimensional reaction rate is:

$$\frac{\rho_0}{\rho}\frac{\dot{W}(\bar{Y}, \theta)}{\dot{W}(1, 1)} = \bar{Y}\exp(Z_e(\theta-1)/(1+\mu(\theta-1))) \tag{33}$$

Parameters Z_e and μ have been introduced earlier for the steady propagating flame problem.

2. An integral solution in the transformed domain

Before solving numerically equations (30), (31) we will analyze them using an integral approach and several assumptions. The purpose of this analysis is to find the thickness of the preheat zone as a function of time. This result gives us the characteristic time scale of the flame response as a function of Lewis number L_e, Zeldovich number Z_e , Karlovitz number K_a and heat release parameter μ.

We assume that the reduced temperature θ and normalized mass fraction $\bar{Y}$ profiles in the transformed domain can be approximated as:

$$\theta(\eta) = 1 - \frac{3}{2}\frac{\eta}{\Delta_\theta} + \frac{1}{2}\left(\frac{\eta}{\Delta_\theta}\right)^3, \ \eta \le \Delta_\theta \qquad \bar{Y}(\eta) = \frac{3}{2}\frac{\eta}{\Delta_Y} - \frac{1}{2}\left(\frac{\eta}{\Delta_Y}\right)^3, \ \eta \le \Delta_Y \tag{34}$$

$$\theta(\eta) = 0, \ \eta > \Delta_\theta \qquad\qquad\qquad \bar{Y}(\eta) = 1, \ \eta > \Delta_Y$$

The profiles are plotted in Figure 2. We are considering the case when $L_e > 1$ and the thickness of the reduced temperature profile in the transformed domain Δ_θ is

11

larger than that of the mass fraction profile. The analysis for the case of $L_e < 1$ is similar.
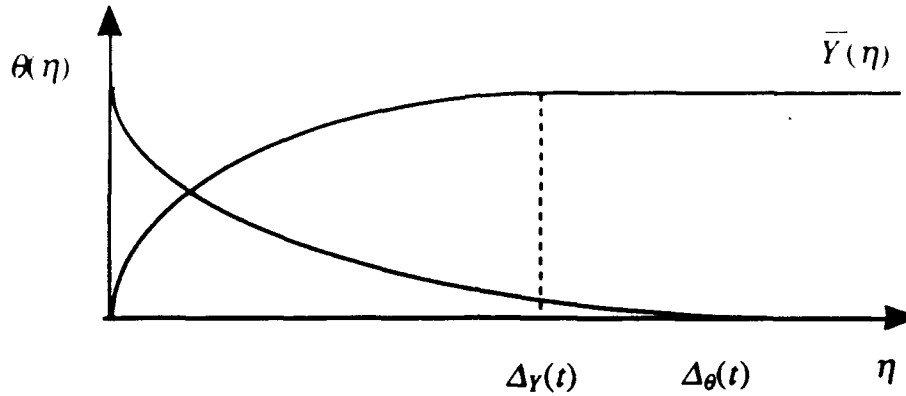
Figure 2. Reduced temperature and mass fraction profiles as functions of transformed coordinate η, $L_e > 1$

We assume that reaction rate expression (33) can be approximated as

$$\frac{\rho_0}{\rho} \frac{\dot{W}(\overline{Y}, \theta)}{\dot{W}(1, 1)} \approx \overline{Y} exp(Z_e (\theta - 1)) \tag{35}$$

since the heat release parameter μ is of the order of 0.8 and the reaction rate has maximum close to the point $\theta = 1$. Integrating equations (30) and (31), we obtain:

$$\int_0^{+\infty} \frac{\partial \theta}{\partial \hat{t}} d\eta = K_a B^2(t) \int_0^{+\infty} \frac{\partial}{\partial \eta} \left(\frac{\partial \theta}{\partial \eta} \right) d\eta + \int_0^{+\infty} \frac{\rho_0}{\rho} \frac{\dot{W}(\overline{Y}, \theta)}{\dot{W}(1, 1)} d\eta \tag{36}$$

$$\int_0^{+\infty} \frac{\partial \overline{Y}}{\partial \hat{t}} d\eta = \frac{K_a B^2(t)}{L_e} \int_0^{+\infty} \frac{\partial}{\partial \eta} \left(\frac{\partial \overline{Y}}{\partial \eta} \right) d\eta - \int_0^{+\infty} \frac{\rho_0}{\rho} \frac{\dot{W}(\overline{Y}, \theta)}{\dot{W}(1, 1)} d\eta \tag{37}$$

Integration of the reaction term yields

$$\int_0^{+\infty} \frac{\rho_0}{\rho} \frac{\dot{W}(\overline{Y}, \theta)}{\dot{W}(1, 1)} d\eta = \int_0^{\Delta_Y} \frac{\rho_0}{\rho} \frac{\dot{W}(\overline{Y}, \theta)}{\dot{W}(1, 1)} d\eta = \int_0^{\Delta_Y} \overline{Y} exp(Z_e(\theta - 1)) d\eta =$$

$$\frac{2}{3} \frac{\Delta_\theta}{\Delta_Y} \frac{\Delta_\theta}{Z_e^2} (1 - exp(-\frac{3}{2} Z_e \frac{\Delta_Y}{\Delta_\theta}) (1 + \frac{3}{2} \frac{\Delta_Y}{\Delta_\theta})) \tag{38}$$

Integration of the unsteady and diffusion terms in equations (36), (37) is straightforward:

12

$$\int_{-\infty}^{+\infty} \frac{\partial \theta}{\partial t} d\eta = \frac{3}{8} \frac{d\Delta_\theta}{dt} \qquad \int_0^{+\infty} \frac{\partial \overline{Y}}{\partial t} d\eta = -\frac{3}{8} \frac{d\Delta_Y}{dt} \qquad (39)$$

$$\int_0^{+\infty} \frac{\partial}{\partial \eta} \left(\frac{\partial \theta}{\partial \eta} \right) d\eta = \frac{3}{2 \Delta_\theta} \qquad \int_0^{+\infty} \frac{\partial}{\partial \eta} \left(\frac{\partial \overline{Y}}{\partial \eta} \right) d\eta = -\frac{3}{2 \Delta_Y}$$

Combining all terms together, we get two expressions from equations (36), (37):

$$\frac{3}{8} \frac{d\Delta_\theta}{dt} = \frac{3}{2} \frac{K_a B(t)^2}{\Delta_\theta} + \Delta_\theta \, f(Z_e, \mu, \frac{\Delta_\theta}{\Delta_Y}, \frac{\Delta_r}{\Delta_\theta}) \qquad (40)$$

$$\frac{3}{8} \frac{d\Delta_Y}{dt} = \frac{3}{2} \frac{K_a B(t)^2}{L_e \Delta_Y} + \Delta_\theta \, f(Z_e, \mu, \frac{\Delta_\theta}{\Delta_Y}, \frac{\Delta_r}{\Delta_\theta}) \qquad (41)$$

Here we denote

$$f(Z_e, \mu, \frac{\Delta_\theta}{\Delta_Y}, \frac{\Delta_r}{\Delta_\theta}) \equiv \frac{2}{3} \frac{\Delta_\theta}{\Delta_Y} \frac{1}{Z_e^2} (1 - exp(-\frac{3}{2} Z_e \frac{\Delta_r}{\Delta_\theta}) (1 + \frac{3}{2} \frac{\Delta_r}{\Delta_\theta})).$$

Equations (41) and (40) are ordinary differential equations. In order to solve them analytically we are making an assumption that $\Delta_\theta / \Delta_Y \approx const$. Actually, the ratio of two thicknesses is a weak function of time. Now we can rewrite equation (40) as follows:

$$\frac{d\Delta_\theta^2}{dt} = 8 K_a B(t)^2 + \frac{16}{3} \Delta_\theta^2 f \qquad (42)$$

The solution of this equation with initial condition $t = 0$, $\Delta_\theta(0) = \Delta_o$ is

$$\Delta_\theta^2(t) = A_5 e^{2K_a t} + (\Delta_o^2 - A_5) e^{A_4 t} \qquad (43)$$

Here

$$A_5 \equiv \frac{8 K_a}{2 K_a - 16 f/3}, \quad A_4 = 16 f/3 \quad .$$

Now, using transformation (25), temperature distribution $\theta(\eta)$ (34) and equation of state (5), we can obtain an expression for the thickness of the reduced temperature profile in the real domain $\delta_\theta^2(t)$ as a function of time

$$\delta_\theta = \int_0^{\Delta_\theta} e^{-K_a t} d\eta / \overline{\rho}(\eta) = \int_0^{\Delta_\theta} e^{-K_a} \left(\theta \mu / (1-\mu) + 1 \right) d\eta = e^{-K_a t} \Delta_\theta (1 + \frac{3}{8} \frac{\mu}{1-\mu}) \qquad (44a)$$

For the mass fraction profile thickness we have

$$\delta_Y = \int_0^{\Delta_Y} e^{-K_a t} d\eta / \overline{\rho}(\eta)) = \Delta_\theta e^{-K_a} \left\{ z + \frac{\mu}{1-\mu} (z - 3z^2/4 + z^4/8) \right\}, \quad z = \Delta_Y / \Delta_\theta \qquad (44b)$$

Now we can use an approximation

13

$$\frac{\delta_\theta}{\delta_Y} \approx \sqrt{L_e} \qquad (45)$$

and assume that temperature and mass fraction profiles in the transformed domain are not very much different from each other, i.e.

$$z = \Delta_Y / \Delta_\theta = 1 + \varepsilon, \quad |\varepsilon| << 1. \qquad (46)$$

Here we implicitly assumed that Lewis number is close to unity. Now we can substitute expression (46) into equation (44b) and, retaining the first terms in the Taylor expansion series, obtain:

$$\delta_Y = \Delta_\theta e^{-K_a t}\left\{1 + \frac{3}{8}\frac{\mu}{1-\mu} + \varepsilon\right\}.$$

Substitution of this expression and equation (44a) into equation (45) yields:

$$\frac{\Delta_\theta}{\Delta_Y} = 1 + \frac{1}{2}(L_e - 1)(1 + \frac{3}{8}\frac{\mu}{1-\mu}). \qquad (47)$$

Here we also used Taylor expansion for Lewis number, assuming that it is close to unity.

In a similar way the ratio of the reaction zone thickness to the preheat zone thickness in the transformed domain, Δ_r / Δ_θ, can be evaluated. Denoting the reaction zone thickness as δ_r, we obtain:

$$\delta_r = \int_0^{\Delta_r} e^{-K_a t}d\eta/\overline{\rho}(\eta)) = \Delta_\theta e^{-K_a t}\left\{z + \frac{\mu}{1-\mu}(z - 3z^2/4 + z^4/8)\right\}, \quad z = \Delta_r/\Delta_\theta << 1$$

Here z can be used as small parameter. Taking this into account, we obtain:

$$\delta_r \approx \Delta_\theta e^{-K_a t} z \left\{1 + \frac{\mu}{1-\mu}\right\}, \quad z = \Delta_r/\Delta_\theta << 1. \qquad (44c)$$

In this equation only linear in z terms were retained. On the other hand, reaction and preheat zone are related by the following equation (Law C.K. 1988):

$$\frac{\delta_r}{\delta_\theta} \approx \frac{\mu}{Z_e}. \qquad (49)$$

Using together equations (44a), (44c) and (49), we obtain

$$\frac{\Delta_r}{\Delta_\theta} = \frac{1 + \dfrac{3\mu}{8(1-\mu)}}{1 + \dfrac{\mu}{1-\mu}}\frac{\mu}{Z_e} = g(\mu)\frac{\mu}{Z_e} \qquad (50)$$

Taking into account equation (43), we rewrite equation (44a) as follows:

$$\delta_\theta^2 = e^{-2K_a t}\Delta_\theta^2(1 + \frac{3}{8}\frac{\mu}{1-\mu})^2 = e^{-2K_a t}(A_5 e^{2K_a t} + (\Delta_o^2 - A_5)e^{-A_4 t})(1 + \frac{3}{8}\frac{\mu}{1-\mu})^2 \text{ or}$$

$$\delta_\theta^2 = (A_5 + (\Delta_o^2 - A_5)e^{-(2K_a - A_4)t})(1 + \frac{3}{8}\frac{\mu}{1-\mu})^2.$$

14

In this equation the time scale of the thickness variation is located in the exponential term and is equal to

$$\tau = 2K_l \cdot \Lambda_3 = 2K_a \cdot \frac{16 f}{3} = 2K_a \cdot \frac{32}{9} \frac{\Delta_\theta}{\Delta_Y} \frac{1}{Z_e^2} (1 - exp(-\frac{3}{2} Z_e \frac{\Delta_r}{\Delta_\theta} (1+\frac{3}{2} \frac{\Delta_r}{\Delta_\theta}))$$

Using equations (47) and (50) to substitute for Δ_r / Δ_θ and Δ_θ / Δ_Y , we obtain the time scale of the flame thickness variation

$$\tau = \left[2K_a \cdot \frac{32}{9 Z_e^2} (1 + \frac{1}{2}(L_e - 1)(1+\frac{3}{8}\frac{\mu}{1-\mu}))(1 - exp(-\frac{3}{2}\mu g(\mu))(1+\frac{3}{2}\mu g(\mu))) \right]^{-1} \quad (51)$$

The right-hand side of this equation consists of two terms: Karlovitz number and a combination of Lewis number, Zeldovich number and heat release parameter. It is easy to demonstrate that for typical chemical and thermal parameters the second term is usually smaller than the first. This suggests :

    (1) Lewis number has minor influence on the flame thickness relaxation time

    (2) Relaxation time is inversely proportional to the applied strain rate (Karlovitz number).

This conclusions of the integral approach will be checked by the numerical solution.

3 . Numerical Procedure.

    Equations (30), (31) with boundary conditions (32) are solved numerically using Crank-Nicholson integration scheme. The source term is linearized in order of to make the scheme implicit.

    In the following discussion, the upper index denotes the time level, the lower index is the grid point number in $(\hat{t}, \eta)$ domain. The computational grid is uniform. Discretization of equation (30) according to the Crank-Nicholson scheme can be written as follows:

$$\frac{\theta_i^{n+1} - \theta_i^n}{\Delta\tau} = \frac{1}{2}(RHS_i^{n+1} + RHS_i^n), \quad (52)$$

$\Delta\tau$ is the time step, RHS is the notation for the right-hand-side of equation (30)

$$RHS_i^n = K_a B^2(t^n)\frac{\partial}{\partial\eta}\left(\frac{\partial\theta}{\partial\eta}\right)_i^n + \left(\frac{\rho_0}{\rho}\right)_i^n \left(\frac{\dot{W}(\bar{Y}, \theta)}{\dot{W}(1, 1)}\right)_i^n \quad (53)$$

The equation is written for n-th time level and i-th grid point. We introduce the following notation for the non-dimensional reaction rate:

$$\Omega \equiv \frac{\rho_0}{\rho} \frac{W(Y, \theta)}{W(1, 1)} \qquad (54)$$

and use an approximation of this term on the (n+1) time level:

$$\Omega_i^{n+1} \cong \Omega_i^n + (d\Omega/d\tau)_i^n \, d\tau = \Omega_i^n + (d\Omega/d\theta)_i^n \, d\theta \cong \Omega_i^n + (d\Omega/d\theta)_i^n \, (\theta_i^{n+1} - \theta_i^n) \qquad (55)$$

Substituting equations (53) - (55) into equation (52), we obtain a finite difference approximation of equation (30):

$$\frac{\theta_i^{n+1} - \theta_i^{n+1}}{\Delta\tau} = \frac{1}{2} \{ K_a B^2(t^{n+1}) \frac{\partial}{\partial\eta}\left(\frac{\partial\theta}{\partial\eta}\right)_i^{n+1} + \Omega_i^n + (d\Omega/d\theta)_i^n (\theta_i^{n+1} - \theta_i^n) + K_a B^2(t^n) \frac{\partial}{\partial\eta}\left(\frac{\partial\theta}{\partial\eta}\right)_i^n + \Omega_i^n \} \qquad (56)$$

Finite-difference approximation of mass fraction equation (31) can be obtained in a similar manner.

Grid in the computational domain $(\hat{t}, \eta)$ remains uniform. Every time step the thickness of flame is compared with the distance from the flame to the upstream and downstream boundaries of the computational domain. If either of these distances is smaller than two flame thicknesses, the computational domain is regridded by doubling the $\Delta\eta$. This procedure is similar to that used by Rutland (1990). Physical coordinate x_i corresponding to the computational coordinate η_i is moving with time according to equations (23) and (25). Each time step a new location of x_i is recalculated in such a way that the origin of the stagnation point flow, $x_i = 0$, remains motionless. For the second derivative of θ in the computational domain the following formula is used:

$$\frac{\partial}{\partial\eta}\left(\frac{\partial\theta}{\partial\eta}\right)_i^{n+1} \cong \frac{\theta_{i+1}^{n+1} - 2*\theta_i^{n+1} + \theta_{i-1}^{n+1}}{(\Delta\eta)^2} \qquad (57)$$

We use equation (57) to rewrite equation (56) in the form suitable for the application of Thomas tri-diagonal matrix inversion algorithm :

$$A_{i+1}^{n+1} \theta_{i+1}^{n+1} + A_i^{n+1} \theta_i^{n+1} + A_{i-1}^{n+1} \theta_{i-1}^{n+1} = C_i^n. \qquad (58)$$

Expressions for the coefficients $A_{i+1}^{n+1}, A_i^{n+1}, A_{i-1}^{n+1},$ and C_i^n are:

$$A_{i+1}^{n+1} = A_{i+1}^{n+1} = -\frac{1}{2(\Delta\eta)^2} K_a B^2(t^{n+1})$$

$$A_i^{n+1} = \frac{1}{(\Delta\eta)^2} K_a B^2(t^{n+1}) + \frac{1}{\Delta\tau} - \frac{1}{2} (d\Omega/d\theta)_i^n \qquad (59)$$

$$C_i^n = \frac{1}{2} K_a B^2(t^n) \frac{\partial}{\partial\eta}\left(\frac{\partial\theta}{\partial\eta}\right)_i^n + \frac{\theta_i^n}{\Delta\tau} + \Omega_i^n - \frac{1}{2} (d\Omega/d\theta)_i^n \, \theta_i^n$$

In this formulation we use boundary conditions (32), corresponding to the one-flame configuration. The derivative $(d\Omega/d\theta)$. is evaluated analytically using equation (33).

4. Results and discussion

Set of parameters

In the numerical simulation we used a set of parameters typical for one-step methane/air combustion:

Activation temperature T_a	$2.0e+04\ K$	
Pre-exponential factor k	$5.0e+08$	
Heat release parameter μ	0.83	
Initial temperature T_0	$300\ K$	(60)
Mixture density ρ_0	$1.11\ kg/m^3$	
Mixture specific heat c_p	$1.12e+03\ J/kg\ K$	
Mixture thermal conductivity λ	$0.04\ W/m\ K$	
Mixture Lewis numbers Le	$0.9, 1, 1.1$	

These parameters were used also in the solution of the steady problem.

Response of flame to a stepwise variation of the strain rate

An important information about the flame transient characteristics is obtained considering the response of flame to the stepwise variation in the strain rate. Initial profiles of temperature and concentration are provided by the code which simulates steady propagating premixed flame. It is described in detail in the previous chapters. Strain rate $\varepsilon(t)$ is changing at time $t = 0$ from zero to some constant value. The response of flame is characterized by two parameters: (1) burning velocity :

$$S_b(t) = \frac{1}{\rho_0} \int_{-\infty}^{+\infty} \dot{W}\ W_{mix}\ dx \tag{61}$$

17

and, (2) integral flame location :

$$x_f \equiv \int_{-\infty}^{-\infty} W x \, dx / \int_{-\infty}^{-\infty} W \, dx \qquad (62)$$

Several remarks can be made about the burning velocity (61). In one dimensional tube flow this integral is equal to the consumption and propagation velocity of the premixed flame. In the stagnation point configuration the interpretation of this integral is less clear. If we assume that after some time flame has stabilized near some location x_f, then we can write mass conservation equation as follows

$$S_u(x) A(x) = S_{b,ss}(\varepsilon) A(x_f(\varepsilon)) \qquad (63)$$

In this equation $A(x)$ is the area between two chosen streamlines at position x where the density is equal to the initial density ρ_0, 'ss' denotes steady state value of integral (58), $S_u(x)$ is consumption velocity with respect to the unburned gases. Equation (63) can be rewritten as

$$S_u(x) = S_{b,ss}(\varepsilon) A(x_f(\varepsilon)) / A(x) > S_{b,ss}(\varepsilon) \qquad (64)$$

for compressive strains. In the case of 2D plane stagnation point flow streamlines are given by equation

$$y(x) = C(\psi) / x \qquad (65)$$

The area $A(x)$ is reduced to $2*y(x)$ and equation (64) can be written as

$$S_u(x) = S_{b,ss}(\varepsilon) x / x_f(\varepsilon) \qquad (66)$$

Thus, in the stagnation point configuration S_u is not only a function of the strain rate ε but also of location x. In the hydrodynamic calculations the thickness of the preheat zone of flame is of the order of 5 mm, which is on the verge of resolution of a regular numerical scheme. In this case the flame front virtually collapses in one infinitely thin surface. To calculate the evolution of this surface one should find: (1) how much of the mixture is consumed per unit area and, (2) how the area of this surface is changing with time. In the following we are trying to address the first question.

Response of flame to the step strain rate have been obtained for parameters (60) and Lewis numbers $Le = 0.9, 1.0, 1.1$. In Figures 3a and 3b strained flame burning velocity S_b and flame location x_f are plotted as functions of dimensional time for different values of stepwise strain rate and unity Lewis number. The range of strain rates is from 700 to 1600 1/sec. When the strain rate is increasing, steady
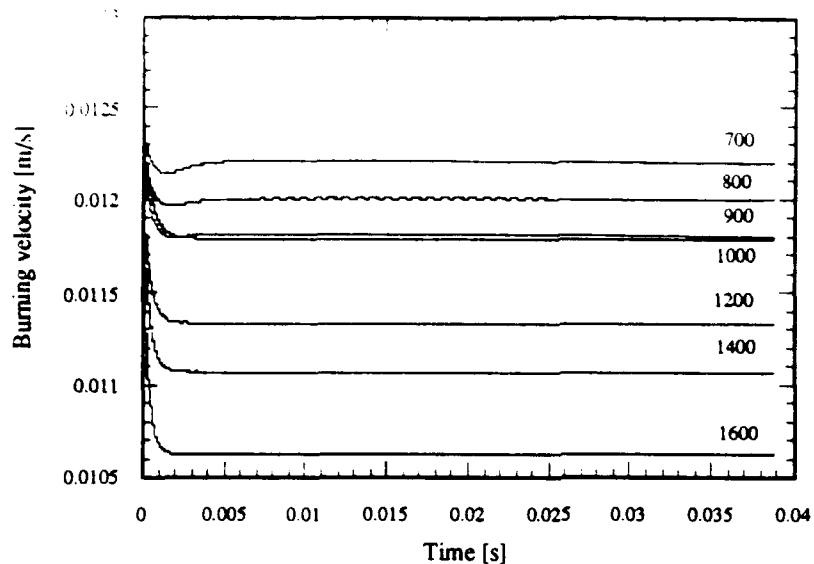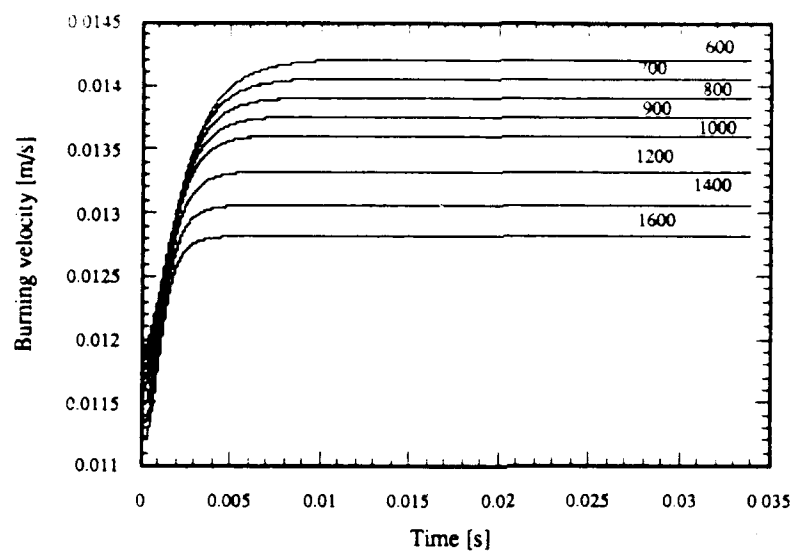
(a) Burning velocity as a function of time, Le=1
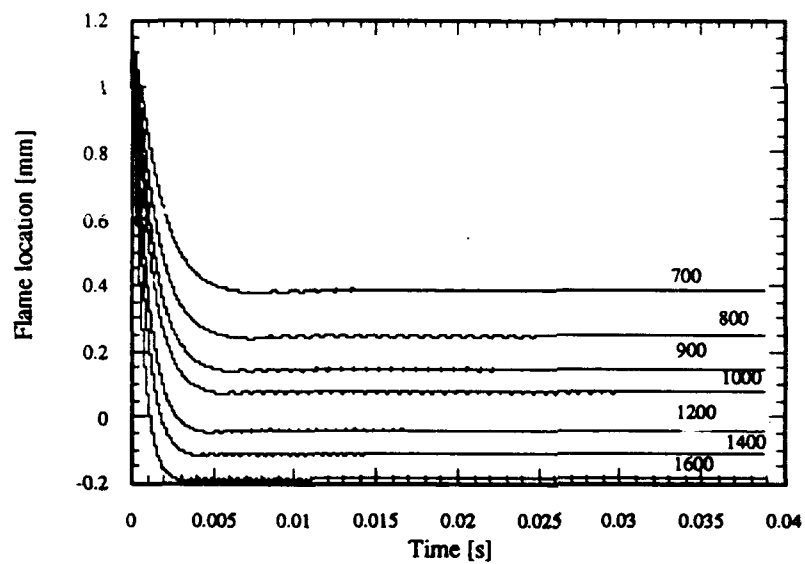
(b) Flame location as a function of time, Le=1

Figure 3 Burning velocity and flame location as functions of time, Le=1

19

state flame location is approaching stagnation plane and, at some value of strain, crosses it. This value is another characteristic of flame. Rather loosely, we will call this value of the strain rate the "extinction strain". Actually, the real extinction doesn't happen at this strain, but the negative burning velocities which occur after the crossing of the stagnation plane are of little interest for us here since they are absent in a typical turbulent flow. For unity Lewis number, when the flame crosses the stagnation plane, burning velocity is lower than the unstrained value only by 8 %. This happens when the strain rate is equal to 1,100 1/sec. Strains higher than 1,100 1/sec cause the flame to move further into the products side until it reaches the location -0.2 mm (see Figure 3b). An additional increase in the strain rate makes the profiles steeper while the flame itself starts to move backward.

In Figures 4 and 5 the same data is plotted for $Le = 1.1$ and $Le = 0.9$, respectively. Now the flame response is substantially different. When Le is lower than unity (see Figure 5), steady state burning velocity is actually higher than the corresponding unstrained value although the flame itself is still moving into the stagnation plane. The extinction strain for $Le < 1$ case is 1,400 1/sec., i.e. 21 % higher than the value of the $Le=1$ case. The flame is "stronger" and more resistant to external disturbances. From the profile point of view this is explained by the particular structure of the preheat zone in the $Le < 1$ case. The flow is modifying the preheat zone in such a way that the maximum of the reaction rate $\dot{W}$ increases while the thickness of the $\dot{W}$ profile decreases only slightly. The situation is reversed in all aspects when $Le = 1.1$ (see Figure 4). Now the extinction strain is approximately 900 1/sec. Burning velocity decreases due to the drop in the maximum of the reaction rate $\dot{W}$.

In a realistic turbulent jet the values of the instantaneous strain rates rarely exceed several hundreds 1/sec. Thus, for example, for very high strain rate of 700 1/sec. steady state burning velocity in a $Le = 1$ mixture will change by - 2.4 %, in $Le = 0.9$ mixture it will increase by +15%, and, finally, in $Le=1.1$ mixture it will drop by 18% from the respective unstrained flame values.

We can conclude that even for low values of strain in the case of non-unity Lewis number burning velocity is significantly modified due to the convection/ preferential diffusion interaction. It is not safe to assume that the strained flame burning velocity is approximately equal to the unstrained value, as it was in the case of $Le = 1$. In a flamelet model, burning velocity has to be considered as a
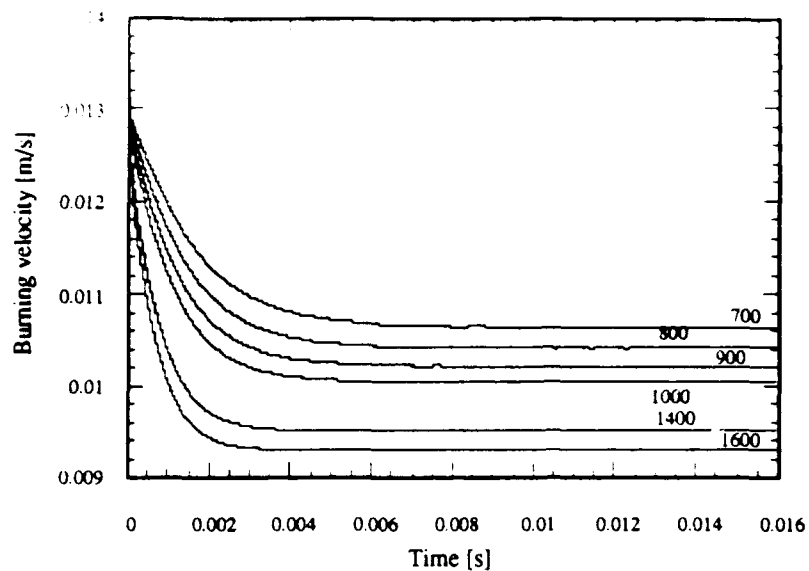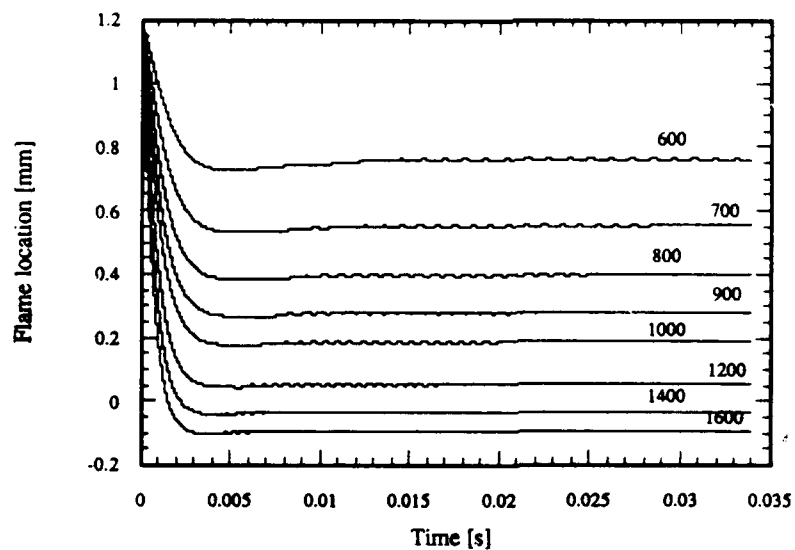
(a) Burning velocity as a function of time, Le=1.1
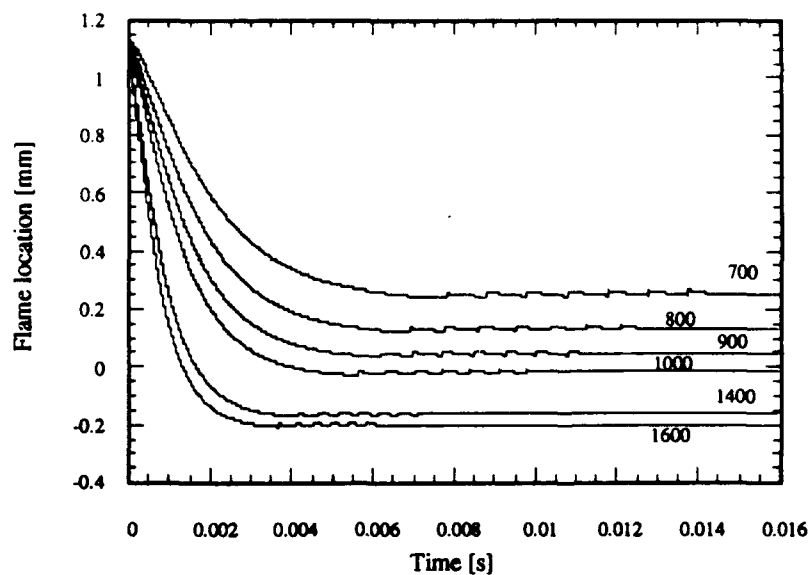
(b) Flame location as a function of time, Le=1.1

Figure 4 Burning velocity and flame location as functions of time, Le=1.1

21

(a) Burning velocity as a function of time, Le=0.9

(b) Flame location as a function of time, Le=0.9

Figure 5. Burning velocity and flame location as functions of time, Le=0.9

22

function of Le and ε. In the next part of this chapter we will try to answer the question of whether this function should depend on time.

The receptivity of flame can be characterized by a relaxation time. This time can be introduced in several different ways but, of course, the functional dependence of it on the thermal and chemical parameters shouldn't be influenced by the way of introduction. Rutland (1990) interpolated burning velocity S_b as the following function of time:

$$S_b = C_0 + C_1 \, exp \, (-t/ \, \tau) \qquad (67)$$

and used the time scale τ as a characteristic of flame response. Figure 3 ($Le = 1$) demonstrates that this type of interpolation produces good result only when the strain rate is higher than the partial extinction strain rate, i.e. $\varepsilon > 1100 \, s^{-1}$. These high values of strain rate were mostly used in the Rutland's paper. For lower values of strain (see Figure 3) flame demonstrates fluctuating response pattern typical for almost critically damped system. In this case we characterize the flame response by the settling time, i.e. the time where the amplitude of the burning velocity fluctuations around the steady state value is becoming less than 0.5 % of the steady state value.

In Figure 6 the settling time is plotted as a function of strain rate in log-log coordinates for several values of the Lewis number. The purpose here is compare the results of numerical simulations with analytical expression (51) for the relaxation time as a function of strain rate (or Karlovitz number K_a), Lewis number L_e, and other parameters obtained from the integral analysis performed in the transformed domain (τ, η). It is clear from the Figure that unity Lewis number (Figure 6b) is a special case as far as the relaxation time is concerned. Close to the partial extinction the restructuring of the preheat zone is taken place and the slope of $\tau_{0.5 \, \%} = \tau_{0.5 \, \%}(\varepsilon)$ curve increases almost two times: from -2.4 before the extinction strain to -0.8 after. The latter value is close to -0.724 reported by Rutland et.al. (1990). In his case I he used mainly the strain rate values higher than the partial extinction value. Hence, only one slope has been reported.

Equation (51) contains Zeldovich number Z_e in the denominator. The typical value of this number is 8. The second term in the sum on the right-hand side of (51) is small compared to the used Karlovitz numbers . This manifests itself in the weak dependence of the relaxation time τ on the Lewis number. The conclusion is supported by the data of Figures 6 (a), (c) and (d). In these Figures the relaxation time is plotted as.a function of strain rate for $Le = 1.2, \, 0.9 \, , \, 0.8$. The slopes of the curves are almost identical, although the curves themselves are
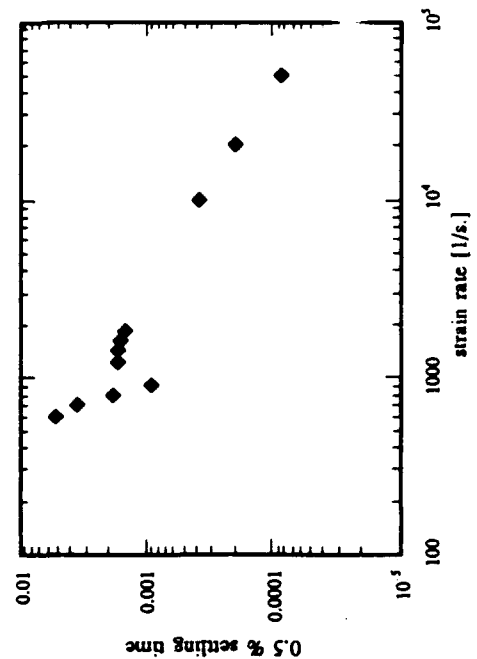
23
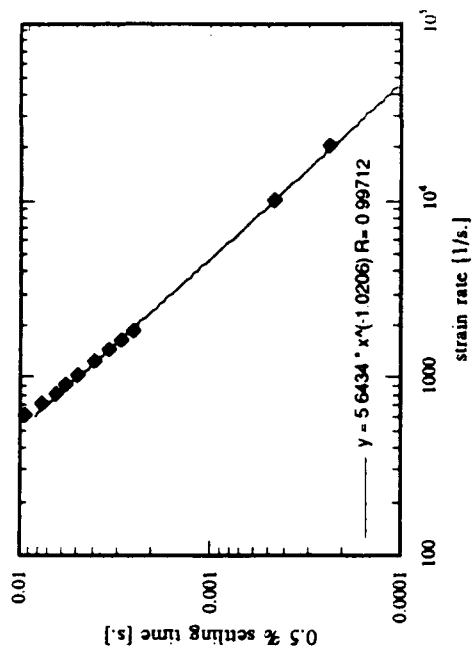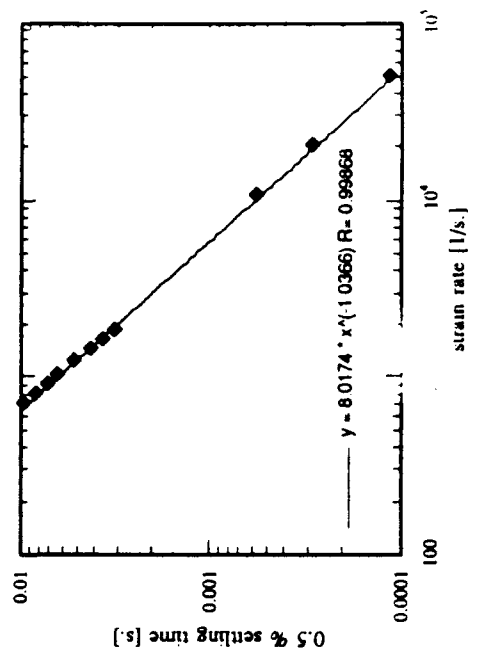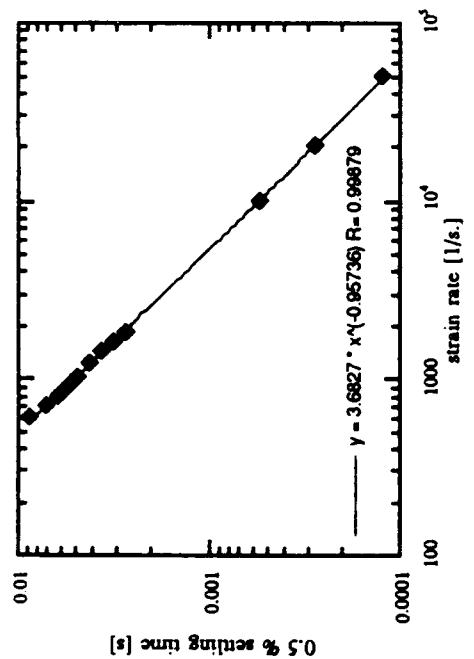
Figure 6. 0.5 % settling time as a function of strain rate and Lewis number

slightly shifting to the right when Lewis number is dropping. A remark should be made here that the relaxation time mentioned in this chapter is the time related to the burning velocity variation while in Chapter II the time scale of the flame thickness variation has been calculated. These time scales do not exactly correspond to each other since not only the reaction zone thickness is changing under the strain, but also the maximum of the reaction rate is usually varying.

Response of flame to the periodic strain rate

Other aspects of the flame transient behavior can be investigated studying flame response to the periodic strain rate. In the previous chapter we obtained that if the strain rate is changing in a stepwise manner it takes some time for the flame to adjust to the new strain. The higher is the strain the lower is the relaxation time. For our set of parameters the relaxation time was of the order of 10^{-2} sec. (see Figure 3). As far as the period of the strain rate fluctuations is concerned, one could guess that in a turbulent flow the smallest period (the highest frequency) of velocity fluctuation is associated with the diffusion time scale. Flow structures with higher frequencies will dissipate due to the diffusion. The diffusion time scale is also critical for the flame phenomena since it characterizes the process of "feeding" the flame. We used a set of the periods of strain oscillations proportional to the diffusion time scale. In the code periodic strain

$$\varepsilon(t) = \varepsilon_{av} + \varepsilon_{amp} \sin(\omega(t - t_{ss})) \tag{68}$$

is applied after the burning velocity reaches its steady state. In this expression ε_{av} is the average value of strain, ε_{amp} is the amplitude value of the oscillations, t_{ss} is the time it takes to reach the steady state. For the set of parameters (60) we choose the average strain ε_{av} to be equal to $700\ s^{-1}$, amplitude of strain oscillations - $0.5*\varepsilon_{av}$ and frequency corresponding to the periods of 5, 2, 1 and 0.3 diffusion times. In Figure 7 burning velocity of flame is depicted as a function of time for this set of parameters. In Figure 7a the period of strain oscillations is 0.3 diffusion time. The diffusion time scale is approximately 10^{-3} sec. Thus the period of oscillations is only slightly higher than the chemical time scale 10^{-5} sec. Flame initially demonstrates periodic response which later becomes irregular. The amplitude of fluctuations is very low since flame relaxation time 10^{-2} sec. is much higher than the period of oscillations $0.3*10^{-3}$ sec. and when the flame starts to
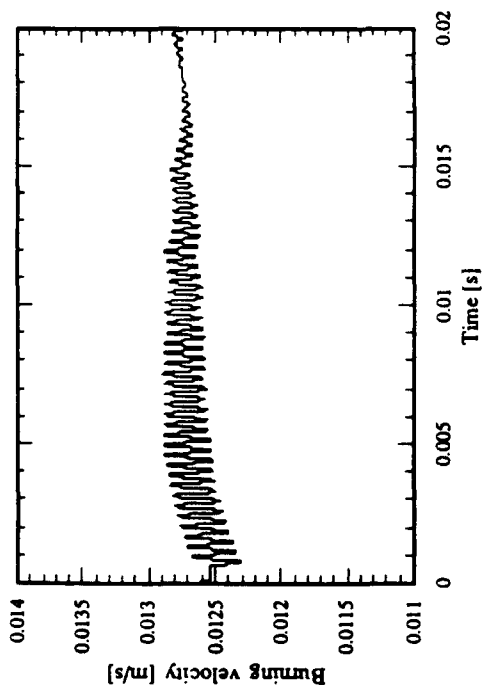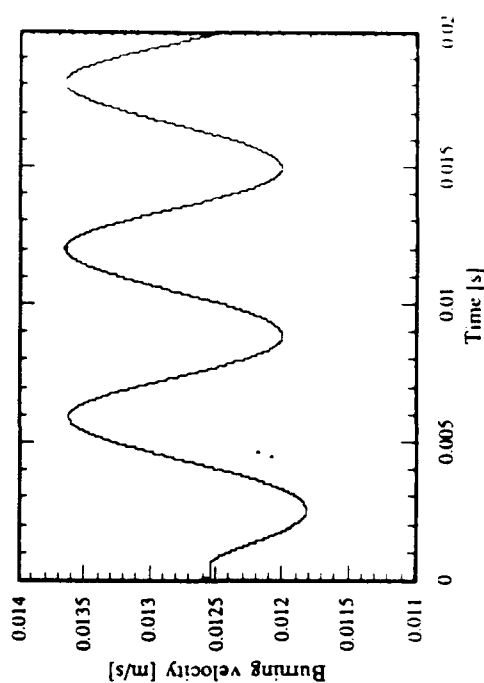
(a) Period of oscillations is 0.3 of the diffusion time scale

(b) Period of oscillations is 1.0 diffusion time scale

(c) Period of oscillations is 2.0 diffusion time scales

(d) Period of oscillations is 5.0 diffusion time scales

Figure 7 Flame response to periodic strain rate, amplitude of oscillations 0.05, Le=1, frequency = var

respond to the flow fluctuation the fluctuation already has changed direction. From Figure 7b ($T = 1$ t_{dif}) to Figure 7c ($T = 2$ t_{dif}) the amplitude of the burning velocity oscillations is increasing and the oscillations themselves are becoming more and more periodic and regular. Fluctuations of the strain rate with the period $T = 5$ t_{dif} induce burning velocity oscillations with the extremum values corresponding to the extremum values of the strain rate. For our set of parameters the average strain is 700 1/sec. and the amplitude is 0.5. It means that the extremum values of the strain rate are 1050 and 350 1/sec. The steady state burning velocity, corresponding. for example. to the strain rate 1050 1/sec. is approximately equal to 0.0118 m/s (see Figure 3). The minimum of the burning velocity fluctuations in Figure 7d is also equal to this value. It means that now flame has enough time to respond fully to the strain rate variations. For the peak strain rate of 1050 1/sec. flame relaxation time is 0.002 sec. (see Figure 3) which is now comparable with the period of oscillations $5*t_{dif} = 5 * 10^{-3}$ sec. For the lower frequencies flame demonstrates fairly good receptivity to the strain rate oscillations. The phase shift between the burning velocity and strain rate fluctuations is constant and close to - 1.3 π.

Another way to characterize the receptivity of a flamelet is to average the instantaneous burning velocity over the significant amount of time T until it does not change any more, and to compare it with the steady state value corresponding to the average strain ε_{av}, i.e.

$$R(\omega, \varepsilon_{av}, \varepsilon_{amp}) \equiv \frac{1}{T} \int_{t_{ss}}^{T} S_b(t, \varepsilon(t)) \, dt \, / \, S_{b, ss}(\varepsilon_{av}) \qquad (69)$$

If the burning velocity oscillations have the average value equal to the corresponding steady state value, then the ratio R is equal to one. In Figure 8 R is plotted as a function of frequency for $\varepsilon_{amp} = 0.5$ ε_{av}. The value of R is very close to 1.02 for a wide range of frequencies.
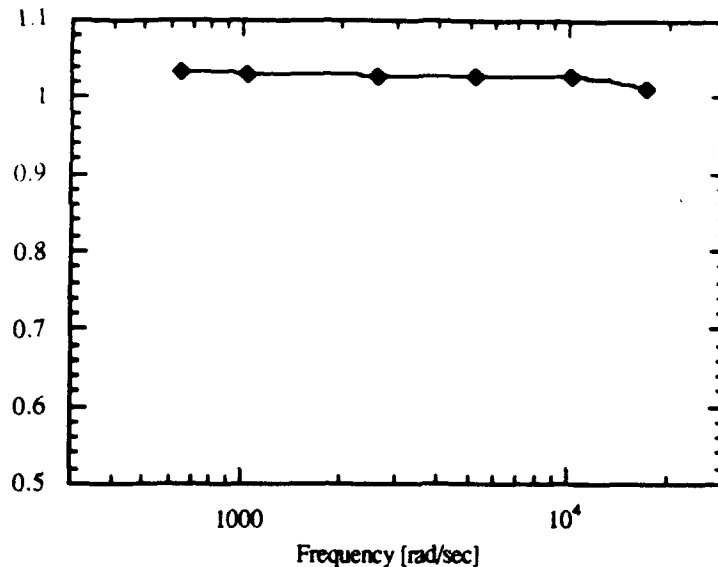
Figure 8. Flame response to periodic strain rate. Ratio of averaged burning velocity
to the burning velocity at the averaged strain rate. Le=1, amplitude = 0.5

It demonstrates that if one is interested in the average burning velocity over a
time period, he can replace the averaging of the instantaneous burning velocity by
the averaging of the strain rate and using the burning velocity at this average strain.
The regular, periodic pattern of the flame response to the sinusoidal strain rate
oscillations demonstrates that the flame relaxation time is a function of the
magnitude of change of the strain rate, but not of the *direction* of this change,
i.e. flame behavior doesn't show significant hysteresis.

Influence of Heat Release on the Extinction Strain

In this paper a simple one-step chemistry mechanism is used. In reality
many chemical reactions are taken place at the same time and the important
question is to establish which chemical reactions should be taken into account, or
where equilibrium or steady-state assumptions can be used. A step in this direction
is to determine how chemical (pre-exponential constant, activation energy),
thermo-chemical (heat release), transport (Lewis number) and flow (strain rate)
parameters influence flame transient characteristics. The influence of Lewis
number and strain rate was described in the previous chapters. In this chapter we
are considering the effect of the heat release on the extinction strain.

28
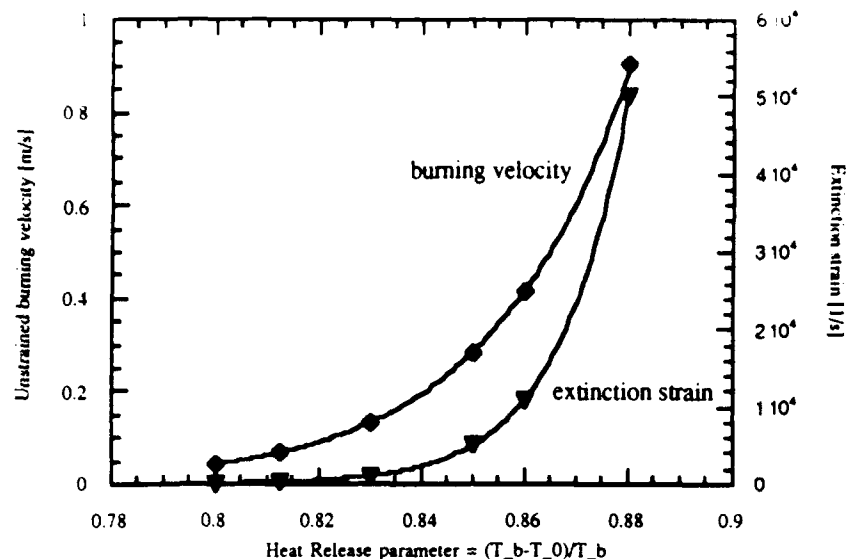
Figure 9 Extinction strain and unstrained burning velocity as functions of heat release parameter, Le = 1; interpolation of the extinction strain :
$\varepsilon_{ex}(\mu) = 3.8704e\text{-}025 * exp(76.18* \mu)$; interpolation of the unstrained burning velocity :
$S_b(\mu) = 2.973e\text{-}015 * exp(37.877* \mu)$

Extinction strain is by our definition the strain when the steady state flame location crosses the stagnation plane for the first time. For a given value of the heat release parameter μ ($\mu = (T_b - T_o)/ T_b$), the value of the extinction strain was determined numerically by trial and error approach, keeping all other parameters (60) the same. The results of these calculations are depicted in Figure 9. In this figure we also plotted the unstrained flame burning velocity. Both functions are strongly dependent on the heat release and are very well interpolated by exponential functions. While the exponential dependence of the unstrained flame burning velocity on the heat release is clear from, say, equation (15), the exponential growth of the extinction strain is somewhat a less expected result.

In a regular flame, thickness of the reaction zone is about ten times smaller then the thickness of the preheat zone. The flow "feels" the flame only through the

29

heat release which takes place in the reaction zone and through the accompanied temperature rise and density drop. The obtained exponential dependence of the extinction strain on the heat release demonstrates that while simplifying chemical kinetics mechanism special attention should be paid to the chemical reactions which determine the energetic balance of the system. For example, for hydrocarbons this means that one shouldn't expect reliable dimensional results from the flame model unless he will take into account energetically important *CO oxidation reactions.*

5. Conclusions

A series of mathematical transformations was used to simplify the equations governing one-dimensional unsteady flame/stagnation point flow interaction. Influence of flow and thermodynamical parameters on the transient response of flame was studied. It was found that:

(1) even for a low value of strain in the case of non-unity Lewis number burning velocity is significantly modified by the convection/ preferential *diffusion interaction.* Strained flame burning velocity is not even approximately equal to the unstrained value, which was the case when $Le = 1$.

(2) under the periodic strain, in the range of frequencies and amplitudes, corresponding to the typical turbulence flow, the ratio of the averaged instantaneous burning velocity to the burning velocity under the averaged strain is close to one. It proves that in this range of frequencies the flame possess a high degree of receptivity to the strain rate fluctuations. The phase shift between the strain rate and burning velocity fluctuations was approximately $-1.3\,\pi$. To evaluate the instantaneous value of the burning velocity, steady state assumption can be used *if* the characteristic time of the strain rate change is greater or equal to the relaxation time of flame when it is affected by constant strain rate with the amplitude equal to the strain rate variation (see Figure 6d). The correction should be made on the phase shift. Flame relaxation time depends mainly on the magnitude of the strain rate change, but not on the direction of this change.

(3) the fact that the extinction strain is an exponential function of the heat release parameter dictates the simplifications of the chemical kinetics mechanism

in such a way, that the most important reactions from the energetic point of view should be preserved.

(4) For non-unity Lewis number 0.5 % settling time is inversely proportional to the applied strain rate for all range of Lewis numbers. The graph of unity Lewis number settling time plotted versus strain rate has pre- and post-extinctional branches with the slopes of -2.4 and -0.8 in log-log coordinates. In this sense, in terms of the relaxation time, unity Lewis number comprises a special case .

References

Candel S. Poinsont T.J. (1990) Flame Stretch and the Balance Equation for the Flame Area. *Combust. Sci. and Tech.*, vol. 70, pp 1-15

Darabiha N. Candel S.M. Marble F.E. (1986) The Effect of Strain on a Premixed Laminar Flame. *Combustion and Flame* 64: 203-217

Ghoniem A. Soteriou M. Cetegen B. Knio O.(1992) " Effect of Steady and Periodic Strain on Unsteady Flamelet Combustion", *24-th Symposium (International) on Combustion,* The Combustion Institute, pp. 223-230

Law C.K. (1988) Dynamics of Stretched Flames . *22nd Symposium (International) on Combustion/ The Combustion Institute*, pp. 1381-1402

Meneveau C. Poinsot T. (1991) Stretching and Quenching of Flamelets in Premixed Turbulent Combustion. *Combustion and Flame* 86:311-332

Rutland C. J. Ferziger J.H. (1990) Unsteady Strained Premixed Laminar Flames. *Cobust. Sci. and Tech.*, vol. 73, pp. 305-326

Zeldovich Ya. et. al. (1985) Mathematical Theory of Combustion and Explosions, Plenum, N.Y.

APPENDIX III

STABILITY ANALYSIS OF DIFFERENTIALLY-HEATED ASYMMETRIC VORTICITY LAYERS

OMAR M. KNIO
Department of Mechanical Engineering
The Johns Hopkins University
Baltimore MD 21218
USA

and

AHMED F. GHONIEM
Department of Mechanical Engineering
Massachusetts Institute of Technology
Cambridge MA 02139
USA

ABSTRACT. The linear instability of a family of inviscid, two-dimensional, variable-density shear layers and wakes is investigated. Vorticity profiles corresponding to a monotonically increasing velocity profile are first examined. A larger family of initial vorticity distributions which model the merger of two unequal vorticity layers of opposite sign is then considered. The latter is obtained by superimposing on the former a wake component, characterized by a spread, δ, and a velocity deficit, W. The initial density distribution resembles a temperature spike and is described by a thickness, σ, and a temperature ratio, T_r. The stability properties of the layers are interpreted in terms of a four-dimensional parameter space (W, δ, T_r, σ). The non-linear evolution of the flowfield is illustrated using the transport element method.

Flowfield stability exhibits strong sensitivity to the details of the density distribution. In the absence of the wake component, the stability properties of the heated layer are divided into three categories according to the thickness of the density profile, σ, and the vorticity thickness, δ_w. For $\sigma \gg \delta_w$, instability of the Kelvin-Helmholtz mode in a uniform-density flow is recovered. When $\sigma \sim \delta_w$, the shear layer mode is inhibited; while this trend persists for $\sigma < \delta_w$, the layer becomes characterized by the appearance of additional short-wavelength unstable modes which become dominant as σ decreases and T_r increases. Addition of a wake component is shown to alter this behavior, and to oppose the stabilizing effects of heat release. In this case, the shear layer mode always dominates the wake mode, and the presence of heated sublayer has a weak effect on the instability of the vorticity layer when δ is large, but may influence the phase speed of unstable waves whenever the zones of high vorticity and high density gradient coincide.

1. Introduction

The evolution of high Reynolds number chemically-reacting free shear flows is governed by a large number of fundamental processes. These processes can be described in terms of the dynamic effects of combustion, which leads to the establishment of

an expansion flowfield and zones of sharp density variation, and in terms of intrinsic instabilities of the underlying shear flow which shape the evolution of the vorticity field. In most cases of practical interest, these effects are closely coupled, as the vorticity-induced convective field governs the molecular mixing processes and hence modulates local reaction rates, while the evolution of the chemical reaction affects the vorticity field through flow divergence field and baroclinic vorticity.

The description of such flows is complicated, due to nonlinear flow-combustion interactions and due to the large number of parameters which govern the relevant molecular and chemical processes. This complexity often necessitates the construction of simplified fundamental models which facilitate the isolation of particular interaction modes, and reduce in the number of governing parameters.

Linear stability theory has proven to be an important tool in theoretical studies of reacting and heterogeneous shear flows [1-12]. In most of these studies, heat release mechanisms associated with the mixing of initially separated reacting species are modelled by corresponding temperature and density profiles which are imposed on an otherwise homogeneous shear flow. Thus, while dynamic effects associated with the presence of an expansion field and the details of the chemical reaction process are omitted, spatial density (and temperature) variation resulting from heat release mechanisms is retained. Using this approach, the essential stability properties of the flowfield have been predicted. In particular, linear stability studies have shown that the presence of two or more zones of different density significantly affects the development of the flow. For instance, it has long been observed that a non-unity density ratio alters the growth of shear flows and influences the entrainment induced by the vortical structures embedded therein [1-4], even when gravity effects are weak [5-6]. In chemically-reacting shear layers, the effects of density variation are equally pronounced; stability results indicate that flowfield stabilization or destabilization may occur, depending on the details of the density and vorticity distributions [7-9]. Furthermore, linear stability results show that the presence of zones of large density variation may also affect the nature of flow instabilities (e.g., by altering the boundaries separating absolute and convective instability modes), and may result in reshaping the global features of the flow [10-12].

Unfortunately, the application of linear stability results to predict the behavior or reacting flows has been complicated due to the large sensitivity of the results to the initial vorticity and density profiles. In this work, this issue is tackled by analyzing the stability of heterogeneous flows for a wide range of initial conditions. Initial density (and temperature) profiles are assumed which model the development of nonpremixed combustion. In addition, initial vorticity profiles corresponding to symmetric and asymmetric shear layers and wakes are considered. A large number of initial conditions is thus constructed, and flowfield stability is examined in a four-dimensional parameter space which models a large family of reacting layers and wakes.

The stability problem is based on linearization of the inviscid heterogeneous flow equations. The formulation of this fluid flow problem is described in Section 2, and computed results are discussed in Section 3. Trends in the behavior of the flow-fields are established and further examined by performing non-linear simulation of selected cases using the transport element method (e.g. [13-14]). Major conclusions

are given in Section 4.

2. Formulation

2.1. THE STABILITY PROBLEM

In a right-handed coordinate system (x, y), the initial flow field is given in terms of the steady flow velocity, $U(y)$, and the imposed density profile, $\varrho(y)$. The flow is assumed two-dimensional and inviscid, and both the perfect gas and the low Mach number approximations of the governing equations are employed [15-16]. The mean density profile is assumed to be the result of heat deposition by the reaction, while diffusion effects are neglected. Under these assumptions, the fluid flow is governed by the momentum and continuity equations, respectively written as:

$$\varrho \frac{D\mathbf{u}}{Dt} = -\nabla p \tag{1}$$

$$\frac{D\varrho}{Dt} = 0 \tag{2}$$

$$\nabla \cdot \mathbf{u} = 0 \tag{3}$$

where $\mathbf{u} = (u, v)$ is the velocity, t is time, $\nabla = (\partial/\partial x, \partial/\partial y)$ is the gradient operator, D/Dt is the material derivative, and p is pressure. The governing equations may be recast in vorticity form by replacing Eqs. (1) and (3) by:

$$\frac{D\omega}{Dt} = \frac{\nabla \varrho}{\varrho^2} \times \nabla p \tag{4}$$

where ω is the vorticity. This formulation will be later used in the simulation of the nonlinear evolution of the flow.

The stability properties of the variable-density shear flow are studied by determining the temporal behavior of small amplitude disturbances imposed on the initial steady flow. These properties are analyzed in terms of the disturbance cross-stream velocity component v_0 which is first written in the form:

$$v_0(y, t) = v(y) \exp(i\alpha(x - ct)) \tag{5}$$

where α is the normalized wavenumber, taken to be real, and $c = c_r + ic_i$ is the complex wave speed. The cross-stream component $v(y)$ obeys the modified Rayleigh equation:

$$v'' = -\frac{\varrho'}{\varrho}v' + \left(\frac{U''}{U - c} + \frac{\varrho' U''}{\varrho(U - c)} + \alpha^2 \right) v \tag{6}$$

with boundary conditions, $v(y \rightarrow +\infty) \sim \exp(-\alpha y)$ and $v(y \rightarrow -\infty) \sim \exp(\alpha y)$. In Eq. (6) and the following, primed quantities indicate differentiation with respect to y.

We are interested in determining whether waves of the form expressed by Eq. (5) are unstable, i.e. whether their growth rate $\alpha c_i > 0$. To this end, the eigenvalue problem is solved using a shooting technique, in which Eq. (6) is integrated from one

344

side of the layer to the other using a fourth-order Runge-Kutta predictor-corrector scheme [17]. We keep iterating in the complex eigenvalue space c using a secant algorithm until the absolute change in c is reduced below 10^{-7}. This procedure yields dispersion relations which relate the growth rate αc_i and the phase speed c_r to the disturbance wavenumber α.

2.2 INITIAL CONDITIONS

The formulation stability of the stability problem is completed by specifying the steady, parallel shear flow velocity and density profiles. A family of shear layers and density profiles is constructed to model the physical processes shown schematically in Fig. 1. We consider chemically-reacting layers formed by merging oxidizer and fuel streams downstream of a thin splitter plate or a bluff body. Immediately following the tip of the plate, the velocity distribution may be modelled as the superposition of two Blasius profiles, starting from a vanishing streamwise velocity and increasing to the free stream velocities $U1$ and $U2$ (Fig. 1b). Further downstream, the velocity profile approaches that of a shear layer, in which the velocity increases monotonically from one side of the splitter plate to the other (Fig. 1a). In the third flow configuration, the incoming streams are separated by a bluff body (Fig. 1c). In this case, the velocity field is regarded as the superposition of two shear layers, each resembling that shown in Fig. 1a. In all cases, the heat deposited by the initial development of the chemical reaction is modelled by a spike in the temperature profile.

In order to model the various flow configuartions anticipated in Fig. 1, we start with the experimentally fitted velocity profile for large distances downstream of the splitter plate,

$$U(y) = U_m + \frac{U_1 - U_2}{2} \tanh\left(\frac{y}{\delta_\omega}\right) \tag{7}$$

where U_m is the mean flow velocity and δ_ω is the local vorticity thickness. The local vorticity thickness is chosen as characteristic length scale, and the velocity is normalized such that the reduced expression,

$$U(y) = \tanh(y) \tag{8}$$

replaces Eq. (7). As suggested by Koch [18], a continuous family of velocity profiles, which approximates all of the distributions shown in Fig. 1, can be obtained by modifying Eq. (9) by letting:

$$U(y) = (1 + W)\tanh(y - \delta) - W\tanh(y + \delta) \tag{9}$$

where W is the wake-deficit, and δ as the displacement of the vorticity layer. In Eq. (10), W and δ are restricted such that $W \leq 0$, and $\delta \geq 0$. When $W = 0$, Eq. (8) is recovered for $\delta = 0$, and increasing the value of $\delta > 0$ results in a pure translation of the $tanh$ profile. On the other hand, when $W < 0$, near wake velocity profiles are approximated for large δ, and the double Blasius profile is imitated when δ is small.

The free stream density and temperature are chosen as a reference density and temperature scales. Accordingly, the normalized initial density profile is taken as

$\delta = 1$	$W = 0.2$	$W = 0.4$	$W = 0.8$	$W = 1.2$
$\delta = 2$	$W = 0.10299$	$W = 0.24709$	$W = 0.55080$	$W = 0.860922$
$\delta = 3$	$W = 0.09261$	$W = 0.22988$	$W = 0.52204$	$W = 0.82119$

TABLE I

a Gaussian profile with standard variation σ, and is expressed in terms of the temperature ratio T_r as follows:

$$\varrho(y) = 1 - \frac{T_r - 1}{T_r} \exp\left(\frac{-y^2}{\sigma^2}\right) \tag{10}$$

In most shear flow applications, including shear layers, the vorticity thickness is usually larger than the product thickness, so that $\sigma < 1$. However, we do not enforce this restriction in order to account for fluid flows characterized by high mass diffusivities, or bluff body flows. When $\delta \simeq \sigma$, the flowfield approximates the merger of two layers of unequal density, a flow configuration that has already been analyzed (see, e.g. [13,19]).

The temporal stability of the family of variable-density layers described above is investigated in the four-dimensional parameter space (W, δ, T_r, σ). We consider four values of the temperature ratio, $T_r = 1, 2, 4,$ and 8.0, i.e. we start with a uniform-density field and then vary the temperature ratio in a range that is representative of most chemically-reacting flows. For each of these cases, the effects of the wake component deficit and thickness are investigated by varying W and δ in such a way as to approximate all the flow configurations shown in Fig. 1. In order to separate the effects of the strength of the wake component, W, from those associated with its thickness, δ, we alter the values of W and δ simultaneously so that velocity profiles having having the same maxima and minima are obtained for all values of δ. In addition to the *tanh* profile having $W = \delta = 0$, we consider 12 (W, d) combinations which are described in Table I. The corresponding velocity profiles are plotted in Fig. 2 for all thirteen cases, the shear layer profile being included with the set of profiles having $\delta = 1$.

Thus, W varies in a wide range of wake deficits, while increasing δ from 1 to 3 represents a migration from an asymmetric shear layer velocity distribution to an asymmetric wake profile, in which vorticity layers are well separated. The stability properties of variable-density layers are first determined assuming equal density and vorticity thicknesses, $\sigma = 1$. The effect of the thickness of the density profile is then investigated by repeating the analysis at $T_r = 4.0$ for four additional σ values. $s = 1.5, 0.75, 0.5,$ and 0.25.

2.3 BRIEF THEORETICAL REVIEW

The linear stability problem of inviscid incompressible parallel shear flow has been studied extensively (e.g [10,20-21]). In this section, we summarize aspects of the theory which directly affect our search for unstable eigenfunctions. We first note that the classical stability results expressed by Rayleigh's theorem [20-21].

346

A necessary condition for instability is that the profile $U(y)$ admits an inflection point

and by Fjortoft s extension.

A necessary condition for instability is that $U'''(U' - U'_s) \leq 0$ somewhere the flow, where U'_s is the velocity at the inflection point

have to be modified when considering a variable density flow. It may easiliy be shown that the appropriate generalizations of the above results may be respectively expressed as:

A necessary condition for instability is that $U''' + (\rho'/\rho)U''$ admits a sign change

and

A necessary condition for instability is that $U''' + (\rho'/\rho)U''(U - U'_s) < 0$ somewhere in the flow.

Thus, in a variable-density field, the behavior of the quantity $U''' + (\rho'/\rho)U''$ replaces that of U'' in the determination of the stability of flow. As indicated in Refs. 1 and 8, this leads us to expect strong interactions between the density variation and the shear flow, whenever zones of high vorticity and density gradient coexist.

The behavior of the curves of $U''' + (\rho'/\rho)U'$ for the flow configurations of Table I is plotted in Fig. 3 for $\delta = 1, \sigma = 1$, and $T_r = 1, 2, 4$, and 8, and in Fig. 4 for $\delta = 1, T_r = 4.0$ and $\sigma = 1.5, 0.75, 0.5$, and 0.25. By the preceding, we are led to expect unstable modes whenever the curves intersect the zero axis. In the uniform-density case, a single intersection point is observed for the $tanh$ profile, and two for the asymmetric layers. This is not surprising, since we expect to be observe one unstable shear layer mode, and one unstable wake mode. However, for large T_r, several intersection points appear for the $tanh$ profile, and may yield additional instability modes. This unexpected result is further investigated in the following section where the behavior of these modes, whose appearance depends on the vorticity-density configuration, is computed.

We conclude this section by extending to variable-density flow the analysis of Drazin and Howard [22] who studied the the long wave behavior of unstable modes, i.e. the limiting behavior of unstable eigenvalues as $\alpha \to 0$. Our analysis is reduced to a form similar to the incompressible case by rewriting the modified Rayleigh equation as:

$$(Z^2 F')' = \alpha^2 Z^2 F \tag{11}$$

where

$$Z^2 \equiv \varrho(U - c)^2 \; ; \; F \equiv \frac{\phi}{U - c} \tag{12}$$

and ϕ is the perturbation potential. Noting that Eq. (12) is identical to Eq. (1.6) of Drazin and Howard [22], we are able to carry out a similar analysis to the one

performed there. (Details will be presented elsewhere). In the limit $\alpha \to 0$, Eq. (14) implies that $Z^2 F'$ is constant and that this constant is zero in order to satisfy the boundary conditions. Hence F is constant in intervals where Z does not vanish, but may have jumps when $Z = 0$. Assuming F has no jumps, a similar argument to that presented in [22] shows that the limiting eigenvalues satisfy:

$$Z_\infty^2 + Z_{-\infty}^2 = 0 \tag{13}$$

For equal free stream densities, Eq. (14) yields the unstable eigenvalue $c = i$ which is recognized as the limiting eigenvalue of the shear layer mode. Density variation does not seem to affect the asymptotic behavior of these long waves.

A similar result is reached if F admits jumps. While the details of the algebraic manipulations are more involved than in the uniform-density case, we are still able to show that if F has a jump at y_0, then $U''(y_0) = 0$. Thus, velocity maxima and minima are expected to represent limiting values of unstable eigenfunctions. For $W < 0$, the profiles considered in this study admit a velocity minimum, which is recognized as the limiting eigenvalue of the (unstable) wake mode.

The long wave approximation estimates are used in the following section to initialize the search for unstable eigenfunctions and to characterize the additional inflection points which appear for the $tanh$ profile at high temperature ratio (Fig. 3). Should these additional inflection points correspond to unstable modes, then the above argument shows that the associated instability mode affects shorter wavelength instability, since the asymptotic behavior of long waves is solely dependent on the details of the velocity profile.

3. Results

3.1. STABILITY OF VARIABLE-DENSITY LAYERS AND WAKES

Stability analysis of the variable-density parallel asymmetric shear flow is first conducted for the velocity profiles of Table I, and density profiles having $\sigma = 1$, and $T_r = 1, 2, 4$, and 8. Since a sharp estimate of an upper bound on unstable wavenumbers was not sought, a complete search for the unstable eigenfunctions over a bounded wavenumber-eigenvalue region cannot be easily conducted. Instead, the search for unstable waves is initiated by concentrating on the behavior of long waves, and extrapolating the asymptotic behavior of unstable shear layer and wake modes, as determined by the theoretical predictions. To this end, the wavenumber is increased incrementally with small step size $\Delta\alpha = 0.01$, until the iterations stop to converge. In all cases, the modified Rayleigh equation is integrated over a mesh of 4000 grid points, equally distributed over the interval $-1 - \delta \leq y \leq 1 + \delta$. Thus, the expected short wave behavior of the additional instability modes is only determined in cases where their instability band extends that of the other modes.

Figures 5-8 show the growth rate and phase speed of unstable modes, computed for $T_r = 1, 2, 4$, and 8, respectively. For brevity, results obtained for the intermediate value $\delta = 2$ are not illustrated. In all cases, the thickness of the heated layer coincides with that of the vorticity layer, $\sigma = 1$. We start with the uniform-density flow (Fig. 5), which is later used as reference to quantify the effects induced by the density variation. Cold flow calculations are summarized as follows:

(1) The growth rate of the shear layer mode increases with increasing wake deficit. This result is expected since higher wake deficits correspond to higher vorticity values.

(2) The highest increase is achieved for the smallest separation distance, $\delta = 1$. This is not surprising and is due to the construction of the family of velocity profiles and the selection of (W, δ) pairs so that the same velocity extrema are obtained for different separation distances. Hence, smaller δ values correspond to higher vorticity concentrations.

(3) The wavenumber of the most unstable shear layer mode exhibits a small increase with increasing wake deficits at $\delta = 1$, but is almost independent of W at higher separation distances. Thus, the wake deficit does not affect the frequency selection of unstable shear layer mode, which is closely approximated by estimates based on the *tanh* profile.

(4) While the growth rate of the most amplified wake mode increases by increasing W, its wavenumber of is almost independent of W. The growth rate maxima for both the shear layer and wake modes are reached for $\alpha \approx 0.6$.

(5) The phase speed of most unstable mode vanishes for the *tanh* hyperbolic velocity profile but increases in the direction of wake deficit with increasing W.

(6) The maximum growth rate of wake mode increases by increasing the separation between the positive and negative vorticity layers. However, in all cases considered, the shear layer mode always dominates the wake mode. This result is best interpreted by focusing on the positive and negative vorticity layers separately, which may be used to distinguish between the symmetric shear layer and asymmetric wake-like profiles. For the latter, the negative vorticity layer, whose inflection point is associated with the unstable shear layer mode, has considerably higher strength and thus dominates wake component.

The impact of heat release on flowfield stability is examined in Figs. 6-8, which show dispersion relations for $T_r = 2, 4$, and 8. The analysis is divided into two sections; results for the symmetric *tanh* profile are discussed first, and then contrasted with corresponding results for the asymmetric layer and wake profiles. As before, dispersion relations for the symmetric *tanh* profile are lumped with those of the asymmetric shear layer mode with $\delta = 1$, and identified by a wake deficit $W = 0$. Examination of the dispersion relations reveals:

(1) By increasing T_r, stabilization of the Kelvin-Helmholtz mode is gradually achieved. As noted by McMurtry et al. [9], who studied the stability of a heated layer idealized by broken-line vorticity and density profiles, heat release inhibits the growth of the most unstable mode, whose amplification rate decreases to a small fraction of the uniform-density maximum as temperature ratio becomes high. The results also indicate that the wavenumbers of the most amplified mode and neutrally stable modes decrease as T_r increases. Thus, the density variation alters the features of the instability in such a way as to stabilize short wavelength disturbances and collapse the instability to a thin band affecting long wave perturbations. On the other hand, the vanishing phase speed property of shear layer mode persists.

(2) The stability properties of the layer are significantly altered for $T_r \geq 4$.

As predicted in the previous section, the computed results show that the flow field now admits three unstable modes. The additional pair of unstable modes are associated with the outer zeros of $(rU'')'$ and are thus called outer modes [8]. Dispersion relations of these modes appear as extensions of that of the Kelvin-Helmholtz mode.

(3) The outer modes have identical growth rates and equal but opposite phase speeds. The phase speeds of the neutrally stable solutions coincide with the flow velocity at the outer inflection points. Meanwhile, at high T_r the outer mode dominates the shear layer mode which is almost stabilized by the density variation. The wavenumber of the most amplified outer modes increases with increasing temperature ratio; thus, the associated mechanism promotes short-wavelength instability.

The stability properties of asymmetric shear layers and wake profiles differ significantly from those of the symmetric *tanh* profile, as the heat release has a less significant impact than in the former case. The stability results for these profiles are divided into two groups, according to the separation distance between the layers of opposite vorticity. For a large separation distance ($\delta = 3$), the amplification curves for the shear layer mode are weakly affected by the presence of a heated region within the vorticity layer. In particular, all of the stability properties of the unstable modes are unaffected, as neither the instability bandwidth nor the wave speed of unstable modes are affected by the temperature ratio. This result is expected, since the density is constant and equal to unity except in the region separating the distinct vorticity layers. In this region, the velocity profile is almost constant, so that $(\rho')'$ is closely approximated by the vorticity derivative U''' in the entire flow. Thus, the vorticity maxima do not lie with regions of high density gradient, and results for uniform-density flow are recovered.

For small separation distances, the presence of a heated fluid layer results in appreciable changes in the stability of the flow, and has a *different* influence on the behavior of the wake and shear layer modes. By increasing the temperature ratio, instability of the wake mode is promoted, as the corresponding amplification curves admit higher maxima. While the phase speeds of the unstable wake modes is weakly affected, the corresponding instability bandwidth is increased, and the wavenumber of the most unstable wake mode favors shorter wavelength instability. This result should be favorably contrasted with the results of Koochesfahani and Frieler who showed that the spatially-developing wake mode may become dominant when the asymmetric vorticity layer is subjected to a severe monotonic density difference [1]. However, in all cases considered in our study, the highest amplification rate of the shear layer mode is always considerably higher than for the corresponding wake mode. Therefore, the effect of heat release is not expected to lead to a qualitative change in the behavior of the perturbed reacting layer, which remains dominated by the growth of unstable shear layer waves.

Shear layer modes exhibit a different response to the imposed density variation. This response resembles the behavior of shear layer modes in heterogeneous layers for which the density increases monotonically from one side of the layer to the other. In both instances, density variation has minimal influence on either the growth rate of unstable Kelvin-Helmholtz modes, or on their stability bandwidth. However, it

significantly affects the phase velocity of the waves. In the heterogeneous shear layer [19], unstable shear layer modes acquire an additional convective velocity component of the same direction as the high density stream. The analogy between the two cases can be established by inspecting the behavior of the density field in the neighborhood of the inflection point of the velocity profile. Here, the "unstable shear layer mode" is associated with the "upper" inflection point of the velocity profile. The density profile has positive derivative in the neighborhood of this inflection point, so that the density increases as we move towards the top free stream. Thus, we are led to expect an increase in the phase velocity of unstable shear layer mode, since the top stream velocity is positive. This expectation is reflected in the stability calculations, which show that the phase velocity of the most unstable shear layer mode increases with increasing temperature ratios and becomes positive for small wake deficits.

3.2. EFFECT OF DENSITY PROFILE THICKNESS

The stability results of the previous section are reexamined for different thicknesses of the density profile. For laminar nonpremixed flames, the thickness of the low-density zone depends on both the thermal and mass diffusivities. Thus, accurate estimates of this thickness relative to the vorticity thickness require the solution of the boundary layer equations for reacting flow, and the results will depend on the Prandtl and Lewis numbers, and on the details of the chemical reaction. In general, the product zone will be embedded within the vorticity layer, since near unity Prandtl and Lewis numbers generally prevail, and initial conditions describe a finite thickness vorticity layer and a sharp interface separating the oxidizer and fuel streams.

In this study, however, such a detailed study is replaced by the simplified approach of considering different values for the density thickness, which are selected in a wide parameter range in order to cover most situations of interest. To this end, the stability of all the velocity profiles of Table I is investigated for a variable density field specified by a fixed temperature ratio $T_r = 4$, which is characteristic of a large number of combustion applications. Meanwhile, the density thickness is gradually varied; the values $\sigma = 1.5, 0.75, 0.5$, and 0.25 are considered. The results of the computations are shown in Figs. 9-12, in terms of the growth rate and phase speed of unstable modes. As before, results for the symmetric *tanh* velocity profile are lumped with those of shear layer modes having $\delta = 1$.

The discussion of the results distinguishes between the stability properties of the shear layer and wake modes, and those obtained for the symmetric *tanh* profile. The latter case is discussed first and is summarized as follows. The behavior of the *tanh* shear layer mode is non-monotonic with respect to variation of the density thickness. The results are best interpreted by first considering the limiting case of very large density thickness. For this density configuration, the vorticity field lies in a zone of almost constant density, so that the uniform-density results are recovered. As σ is decreased and becomes close to the vorticity thickness, stabilization of the shear layer mode is observed. The maximum growth rate, the most amplified wavenumber and the stability bandwidth are all reduced. On the other hand,

the nature of the instability is not altered, as all unstable modes have zero phase velocity. As σ is further decreased, stabilization of the shear layer mode continues but the flow field acquires an additional pair of unstable modes. Due to the symmetry of the density and velocity profile, these additional "outer modes" have identical instability bandwidths and amplification curves, with equal magnitude but opposite-sign phase velocities. In the range of density thicknesses considered, the instability of the additional modes is promoted by decreasing σ, as the corresponding most-amplified modes admit higher growth rates and wavenumbers. This is accompanied by an increase in the stability bandwidth and the phase velocity magnitude. Thus, *tanh* shear layers which accommodate high heat release slow reactions are more susceptible to such short wavelength instabilities. However, we do not expect this mechanism to persist continuously as σ is further decreased, since in the limit $\sigma \downarrow 0$ the deposited energy vanishes so that results for uniform-density flow should be approached.

The effect of the density density thickness is greatly attenuated in the presence of a wake deficit. In all cases, weak variations of the stability properties of the flow are recorded as the value σ is altered. The response of the wake mode to changes in the density thickness σ is extremely weak, as the results exhibit almost insignificant changes in the stability bandwidth, amplification curves, and phase relationships. These changes are of little importance since the shear layer mode dominates the initial evolution of the flow. The latter is weakly affected by changes in the density thickness, which result in small modulation of the phase speed of unstable modes. As previously mentioned, this result is expected, based on the similarity between the behavior of the vorticity and density profiles around the unstable inflection point and that described in monotonic variable-density shear layers [19].

3.3. VISUALIZATION OF UNSTABLE EIGENFUNCTIONS

Finally, the evolution of asymmetric shear layers is numerically computed. Attention is focused on the late stages of flowfield evolution, which witness the formation of vortical structures due to the non-linear breaking of unstable waves. The results are used to examine the validity of extending the trends established in the linear stability analysis. This exercise is limited to a visualization of the effect of these structures on the deformation of the flow and the evolution of the vorticity. A detailed investigation of the dynamics of the flow is not attempted in this work, as detailed reacting flow computations will be discussed in a subsequent study.

Numerical simulation of the variable-density flowfield is performed using the two-dimensional transport element method. The numerical scheme, which belongs to an adaptive class of Lagrangian field methods, is based on the discretization of the vorticity and density gradient fields into a number of transport elements of finite overlapping circular cores. Accordingly, the velocity field is given by a discrete, desingularized convolution over the induced vorticity field of the transport element. A similar convolution yields the density field. Once the velocity field is computed at the element centers, a second-order predictor corrector integration scheme is used to track their motion and to advance the numerical solution. Discrete vorticity and density values evolve according to Eqs. (4) and (2), respectively. Meanwhile, discrete density gradients are updated by relating their evolution to the material

352

TR	σ	W	δ	NR	Core size	Wavenumber	Wavelength	Growth rate
1	-	0	0	11	0.72	0.45	13.9	0.19
1	-	1.2	1	17	0.70	0.57	11	0.40
1	-	.8215	3	25	0.70	0.45	13.9	0.35
4	1	0	0	17	0.35	0.41	15.3	0.06
4	1	1.2	1	23	0.35	0.66	9.52	0.42
4	1	.8215	3	33	0.35	0.47	13.4	0.37
4	0.5	0	0	33	0.175	0.7	8.98	0.13
4	0.5	1.2	1	45	0.175	0.68	9.24	0.44
4	1.5	1.2	1	25	0.35	0.59	10.65	0.37

TABLE II

deformation of the Lagrangian mesh. Details of the formulation and construction of this numerical scheme, which has been extensively employed in the simulation of variable-density and reacting flows, can be found elsewhere [13-14,19]. Thus, only a brief account of the computational parameters used in the calculations is given.

The visualization of unstable modes is performed using the temporal model of the vorticity layers. In this model, the velocity and density fields are spatially periodic in the streamwise direction. The periodicity length, λ, is close to the wavelength of the most unstable mode, as determined above. The region of finite vorticity and density gradient is initially discretized on a square mesh, having NR and NS grid points in the cross-stream and streamwise directions, respectively. The core size of the transport elements, δ, and the discrete values of vorticity and density gradient are found by minimizing the error between the numerical and initial fields [13].

Nine cases of differenitally-heated layers and wakes are numerically investigated. The layers are identified by values of the temperature ratio, the thickness of the density layer, the wake deficit and the displacement of the wake profile, which are listed in Table II alongside the wavenumber, wavelength, and growth rate of the corresponding most unstable mode. Table II also shows the number of computational grids in the cross-stream direction, NR, and the core radius of the transport elements. In all calculations, the time step $\Delta t = 0.02$.

The first three cases correspond to uniform-density flow, and are selected in order to examine the effects of the wake deficit and the displacement of the wake profile. The numerical experiments are repeated by keeping the same (initial) vorticity field parameters and altering the initial density field by letting $T_r = 4$, and $\delta = 1$. Thus, for these initial flow configurations (cases 4-6), the initial vorticity and density thicknesses coincide. Finally, the dependency of the evolution of the flow field on the thickness of the initial density profile is examined in cases 7-9. These cases correspond to vorticity field configurations for which the linear stability analysis predicts a strong (case 7) or weak (cases 8 and 9) response to changes in δ.

The computations are initialized by introducing a perturbation in the flow field using sinewaves having the same periodicity wavelength as the computational domain, λ, and amplitude 0.01λ. The perturbation is applied by displacing the location

of the transport elements in the cross-stream direction according to the sinewaves. The calculations are extended in order to observe the linear amplification of the unstable modes, and the early non-linear stages of their evolution. For cases 1, 4, and 7, this objective is achieved by carrying out the computations until $t = 12$. In the remaining cases, calculations are stopped at $t = 9$. Results of the simulation of the flowfield starting from the flow configurations of cases 1-9 are shown in Figs. 13-21, respectively. The figures are generated by plotting the location and instantaneous position and velocity vector of the transport elements. The development of the vorticity field thus illustrated is discussed below.

Figure 13 shows that the evolution uniform-density shear layer initially described by the symmetric $tanh$ velocity profile does not destroy the symmetry of the vorticity field. The vanishing phase speed of the instability wave, predicted by the linear theory for the linear Kelvin-Helmholtz wave, persists as the waves undergo a non-linear growth regime, and roll to form a concentrated core of vorticity. Detailed computations of similar flow fields have been performed previously [13], and have shown that, when pairing is disabled, the late stages are characterized by a maturation of the vortex cores and the continuous entrainment of the vorticity from the braids into the cores.

The superposition of wake deficit on the symmetric, monotonic layer profile results in a significant departure from the previously discussed behavior. The evolution of the asymmetric layers of Figs. 14 and 15 is characterized by the finite wave speed of the linear instability modes, and by the convective motion of the vortical structures which form following their nonlinear evolution. As previously discussed, the direction of motion of the linear instability waves can be determined from the the linear stability analysis and by inspection of the initial velocity profile. The computations are in agreement with the results of the linear theory, which predicts almost equal phase speeds for the most unstable modes, and a slightly larger growth rate for the layer with the smaller separation distance. Alternatively, this behavior can be qualitatively predicted by considering the contribution of the "weaker" vorticity layer, whose induced flow field leads to the motion of the linear waves and of the vortices.

The consideration of the effects of opposite regions of vorticity is easier for the larger displacement parameter ($\delta = 3$, Fig. 15), since the corresponding vorticity profiles are formed of well-separated strips of opposite sign of vorticity. The computed results indicate that the evolution of the flowfield is dominated by the stronger (negative) vorticity layer. The latter appears to develop independently of the weaker vorticity layer, which does not exhibit significant deformation during the period of the simulation. This assessment no longer holds in the case $\delta = 1$, which shows that both regions of vorticity deform simultaneously (Fig. 14). This results in a greater deformation of the vorticity field and the formation of a substantially larger vortex core.

The impact of the density variation on the development of the flow is illustrated in Figs. 16-18, which show the evolution of shear layers characterized by the same initial vorticity distributions previously considered, and a density profile having $T_r = 4$, and $\sigma = 1$. When starting with the symmetric $tanh$ velocity profile, the growth of Kelvin-Helmholtz waves is significantly suppressed. Moreover, the non-

linear wavebreaking of these modes results in the formation of weak vortex cores which are less coherent than in the uniform-flow case (Fig. 16). These results are in agreement with the predictions of the linear stability theory and with the computations of McMurtry et al. [9] who considered the evolution of symmetric reacting shear layers.

Density variation effects are considerably less pronounced in the presence of a wake component. For large separation distance, $\delta = 3$, comparison of the uniform- and variable-density results (Figs. 15 and 18, respectively) shows that the presence of a heated layer has almost no influence on the development of the flow. These results extend those of the linear stability theory, which predicts little changes in the wavelength, growth rate, and phase speed of the most unstable Kelvin-Helmholtz waves with the variation of the density profile for this initial vorticity configuration. On the other hand, the interactions of the density and vorticity field cannot be neglected for small separation distance, $\delta = 1$. As indicated in Table II, the wavelength of the most-unstable mode is decreased as the temperature ratio is increased to $T_r = 4$. Moreover, while the growth rate of this mode is not significantly altered by the presence of the heated layer, its phase speed is noticeably reduced. This observation also holds when considering the convective motion of the vortices which form following the nonlinear evolution of the unstable waves (Figs. 14 and 17). However, in both cases, the vorticity-density interactions do not suppress linear growth and do not inhibit the formation of large coherent vortex cores.

The sensitivity of the flow-field to the details of the initial density profile is examined in Figs. 19-21. In particular, the stabilization of the symmetric layer by heat release and the weak dependence of the asymmetric layer on the presence of the heated layer is investigated. As previously mentioned, when the regions of high vorticity and density gradient are well separated, the initial development flow is approximated by the uniform-density equations, so that layers characterized by a large separation distance will not be further considered. For the symmetric case, Fig. 19 indicates that by decreasing the thickness of the density profile to $\sigma = 0.5$, the behavior of the shear layer undergoes an additional transition. The results reflect the prediction of the stability theory which indicates that in this regime the most unstable mode consists of a pair of travelling waves of equal growth rates, and equal but opposite phase speeds. These waves amplify as they move away from the middle of the computational domain. The rollup of the waves occurs as the two trains of periodic waves meet at the boundaries of the computational domain, and is followed by the formation of vortices whose cores are smaller and less coherent than their uniform-density counterparts. This mechanism differs significantly from the rollup of the linear Kelvin-Helmholtz waves in uniform-density flow, which, as indicated by the theory, have appreciably larger growth rates. Thus, the stabilizing effects of heat release are expected to persist for this profile, though the details of the density distribution may lead to radical changes in the development of the flow and in the structure of the associated vorticity field.

On the other hand, the addition of a wake deficit greatly diminishes the "stabilizing" impact of the density variation. As predicted by the linear theory and observed in the computations, the early evolution of the asymmetric layer having a large wake deficit is almost insensitive to the presence of the heated layer. For such

initial vorticity configurations, the effects of density variation are limited to a small modulation of the wavelength, growth rate, and phase speed of the most unstable mode. Moreover, as illustrated in Figs. 14, 17, 20 and 21, similar vortical structures are obtained as a result of the non-linear wavebreaking of the unstable modes. This observation holds for all the asymmetric layers considered, despite the fact that the details of the vorticity distribution within the vortex cores and in the braids joining neighboring vortices and the convective motion of the eddies are strongly affected by baroclinic vorticity generation in the later stages of evolution of the flow [13,19].

4. Conclusions

In this work, stability of heterogeneous shear flows is investigated using linear stability analysis and numerical simulations. A large number of initial flow configurations which model the development of nonpremixed reacting shear flow are analyzed. The initial conditions are used to examine the effects of heat release associated with the development of a nonpremixed flame on the stability of asymmetric shear layers and wakes. The latter belong to a continuous family of velocity profiles which is constructed by deforming the symmetric $tanh$ shear layer profile using a wake component characterized by characterized by a spread, δ, and a velocity deficit, W. Density variation is used to model the effects of heat release. The initial density distribution corresponds to a temperature spike and is described by a thickness, σ, and a temperature ratio, T_r. Stability curves are obtained in this four-dimensional parameter space and numerically visualized using the transport element method. The numerical simulations are extended into the nonlinear stages of flowfield evolution in order to examine the validity of extrapolating the linear stability results.

Stability of the $tanh$ reacting shear layer exhibits strong sensitivity to the details of the density distribution. When the density and vorticity thicknesses are close, stabilization of the shear layer occurs as the temperature ratio increases. This effect is manifested by a sharp decrease in the instability growth rate, the nonlinear evolution of unstable eigenfunctions yields weaker less-coherent vortex structures than those observed in uniform-density flow. By decreasing the thickness of the density profile, additional inflection points and instability modes are observed. These instability modes dominate the shear layer mode which is almost stabilized by the heat release. However, while the associated growth rates increase with decreasing density thickness and appear to approach the maximum growth-rate values obtained for uniform-density flow, the nonlinear evolution of these instability modes does not result in the formation of concentrated vortices or in substantial deformation of the flow. Thus, for the $tanh$ profile, heat release tends to stabilize of the flow.

Addition of a wake deficit significantly alters the stability of the flow. In the parameter range considered, two flow configurations are distinguished. When the zones of high density gradients and vorticity magnitude are well separated, heat release and density variation have almost no impact on flowfield stability. In this case, the growth rate and phase speed of unstable waves are weakly affected, and their non-linear evolution results in the formation of large concentrated asymmetric vortices. On the other hand, when regions of high vorticity and density gradients are close or coincide, heat release has a weak effect on the development of the flow. While the growth rates of unstable waves are almost unaffected, their phase speeds

356

depend on the details of the density variation. This mechanism is also observed in the later stages of evolution of the flow, which indicate that the convective motion of the large vortices is modulated in the same manner as the phase velocity of the corresponding linear waves. Thus, heat release is not expected to inhibit the growth of unstable modes in asymmetric layers and wakes, but may however influence the global features of the flow.

The correspondence between computed stability results and initial flow configurations indicates that the effects of heat release may be intuitively predicted by simple examination of the behavior of the density profile in the neighborhood of the inflection point of the velocity profile. If the density profile reaches a minimum in the neighborhood of the inflection point of the velocity profile, stabilization of the corresponding unstable mode is expected. If the density gradient does not vanish in this neighborhood, we expect a minor variation in the growth rate of the unstable mode, and a modulation of its phase speed which depends on the sign of the density gradient. In this case, the results exhibit analogous trends to those established for symmetric shear layers separating streams of unequal density, where unstable waves are observed to acquire a streamwise convection component in the direction of the high-density stream [13].

The large predicted differences in the stability properties for symmetric and asymmetric reacting layers lead us to expect significant sensitivity of developing reacting shear layers to initial disturbances. In particular, if unstable modes are excited at short distances downstream of the splitter plate, i.e. before viscous diffusion leads to the destruction of the wake deficit associated with the merger of the Blasius profiles, significant stabilization by heat release is not expected. Otherwise, a sharp decrease in shear layer growth, mixing and burning efficiency is anticipated.

We finally note that, in the parameter range considered, shear layer modes were always found to dominate the wake modes. Thus, heat release and density variation are not expected to produce a significant change in the shape of instability [8]. Our results should be contrasted with those of Koochesfahani and Frieler [1] who showed that for large wake deficits and density differences, the initial development of the layer can be dominated by the amplification of unstable wake modes. A stability analysis in this flow regime was omitted, since the corresponding flow configurations are not representative of typical reacting shear flow applications. Extension of the parameter range to include these initial conditions is postponed to a subsequent study which will focus on direct simulation of the developing reacting flow.

Acknowledgements

References

[1] Koochesfahani, M.M., and Frieler, C.E., "Instability of Nonuniform Density Free Shear Layers with a Wake Profile," AIAA Journal, Vol. 27, No. 12, 1989, pp. 1735-1740.

[2] Yu, M.-H., and Monkewitz, P.A., "The Effect of Nonuniform Density on the Absolute Instability of Two-Dimensional Inertial Jets and Wakes," Physics of Fluids A, Vol. 2, No. 7, 1990, pp. 1175-1181.

[3] Dimotakis, P.E., "Turbulent free shear layer mixing," AIAA 27th Aerospace Sciences Meeting, AIAA Paper 89-0262, 1989.

[4] Brown, G.L. and Roshko, A., "On Density Effects and Large Structure in Turbulent Mixing Layers," Journal of Fluid Mechanics, Vol. 64, July 1974, pp. 775-816

[5] Maslowe, S.A., and Kelly, R.E., "Inviscid Instability of an Unbounded Heterogeneous Shear Layer," Journal of Fluid Mechanics, Vol. 48, No. 2, 1971, pp. 405-415

[6] Koop, C.G., and Browand, F.K., "Instability and Turbulence in Stratified Fluid with Shear," Journal of Fluid Mechanics, Vol. 93, 1979, pp. 135-159.

[7] Hegde, U.G., and Zinn, B.T., "Vortical Mode Instability of Shear Layers with Temperature and Density Gradients," AIAA Journal, Vol. 28, No. 8, 1990, pp. 1389-1396.

[8] Shin, D.S., and Ferziger, J.H., "Linear Stability of the Reacting Mixing Layer," AIAA Journal, Vol. 29, No. 10, October 1991, pp. 1634-1642.

[9] McMurtry, P.A., Riley, J.J., and Metcalfe, R.W., "Effects of Heat Release on the Large-Scale Structure in Turbulent Mixing Layers," Journal of Fluid Mechanics, Vol. 49, 1989, pp. 291-332

[10] Huerre, P., and Monkewitz, P.A., "Local and Global Instabilities in Spatially Developing Flows," Annual Review of Fluid Mechanics, Vol. 22, 1990, pp. 473-537

[11] Monkewitz, P.A., and Sohn, K.D., "Absolute Instability in Hot Jets," AIAA Journal, Vol. 26, No. 8, 1988, pp. 911-916

[12] Huerre, P., and Monkewitz, P.A., "Absolute and Convective Instabilities in Free Shear Layers," Journal of Fluid Mechanics, Vol. 159, 1985, pp. 151-168.

[13] Krishnan, A., Numerical Study of Vorticity-Combustion Interactions in Shear Flow, Ph.D. thesis, M.I.T., 1989.

[14] Ghoniem, A.F. and Krishnan, A., "Origin and Manifestation of Flow-Combustion Interactions in a Premixed Shear Layer," Twenty-Second Symposium (International) on Combustion, The Combustion Institute, 665, 1988.

[15] Rehm, R.G. and Baum, H.R., "The equations of motion for thermally driven, buoyant flows," J. Res. N.B.S. 83, 297, 1978.

[16] Majda, A. and Sethian, J.A., "The derivation and numerical solution of the equations for zero Mach number combustion," Comb. Sci. Tech. 42, 185, 1987.

[17] Betchov, R., and Criminale, W.O., Stability of Parallel Flows, Academic Press, 1967

[18] Koch, W., "Local Instability Characteristics and Frequency Determination of Self-Excited Wake Flows," Journal of Sound and Vibration, Vol. 99, 1985, pp. 53-83.

[19] Soteriou, M.C., Knio, O.M., and Ghoniem, A.F., "Manipulation of the Growth Rate of a Variable Density, Spatially Developing Mixing Layer via External Modulation," AIAA 29th Aerospace Sciences Meeting, January 7-10, 1991, Reno, Nevada, AIAA Paper 91-0081.

[20] Drazin, P.G., and Howard, L.N., "Hydrodynamic Stability of Parallel Flow of Inviscid Fluid," Advances in Applied Mechanics, Vol. 9, 1966, Academic Press, pp. 1-89

[21] Drazin, P.G., and Reid, W.H., Hydrodynamic Stability, Cambridge University Press, 1981.

[22] Drazin, P.G., and Howard L.N., "The Instability to Long Waves of Unbounded Parallel Inviscid Flow," Journal of Fluid Mechanics, Vol. 14, 1962, pp. 257-283.

358
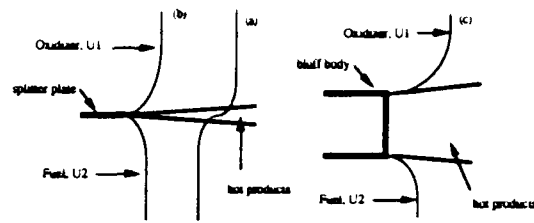
Figure 1. Schematic sketch of a shear layer (left) and a bluff-body wake flow (right)
The self-similar monotonic shear layer profile is shown in curve (a), while curves
(b) and (c) respectively illustrate asymmetric shear layer and wake profiles. The
top (bottom) row corresponds to $\delta = 1$ ($\delta = 3$).
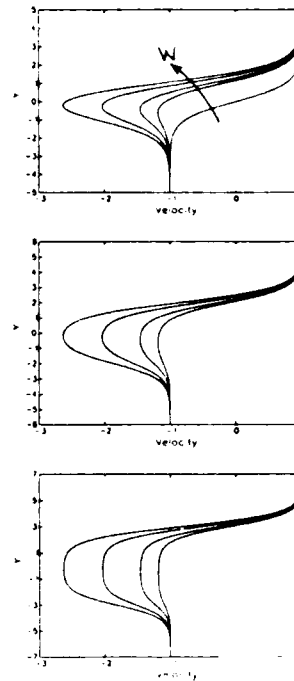
Figure 2. Velocity profiles for the family of shear layers given by Eq. (10), with
(W, d) combinations of Table I. The plots are respectively arranged from top for
increasing wake increasing thickness, $\delta = 1, 2,$ and 3. The $tanh$ profile is shown with
the $\delta = 1$ subcollection. The top (bottom) row corresponds to $\delta = 1$ ($\delta = 3$).
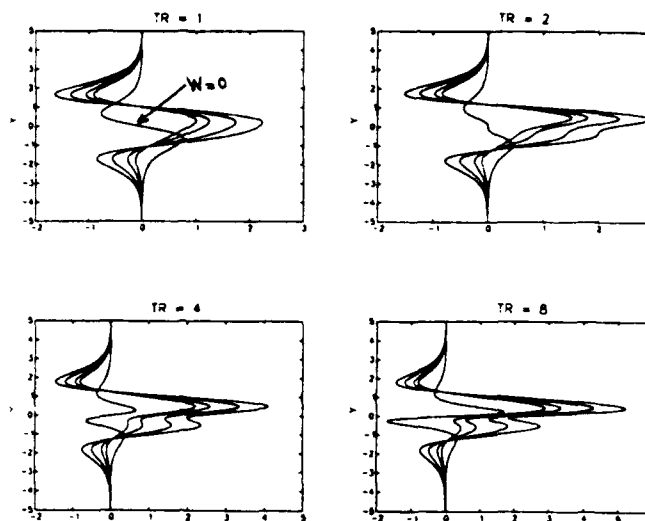
Figure 3. Profiles of $U''' + \rho'U''/\rho$ for layers described by $\sigma = 1$, $\delta = 1$ and (a) $T_r = 1$ (uniform-density flow); (b) $T_r = 2$; (c) $T_r = 4$; and (d) $T_r = 8$. Similar behavior is obtained for the larger separation disctances, $\delta = 2$ and 3. The top (bottom) row corresponds to $\delta = 1$ ($\delta = 3$).
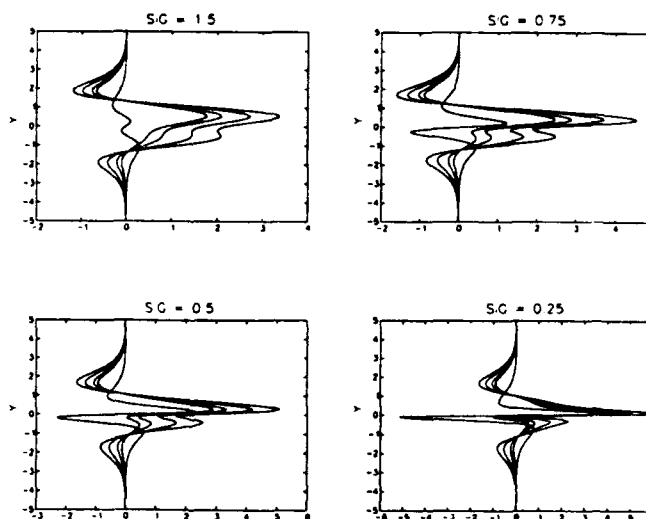
Figure 4. Behavior of $U''' + \rho'U''/\rho$ for the velocity profiles of Fig. 2, with density distribution given by $T_r = 4$, and (a) $\sigma = 1.5$; (b) $\sigma = 0.75$; (c) $\sigma = 0.5$; and (d) $\sigma = 0.25$. The top (bottom) row corresponds to $\delta = 1$ ($\delta = 3$).
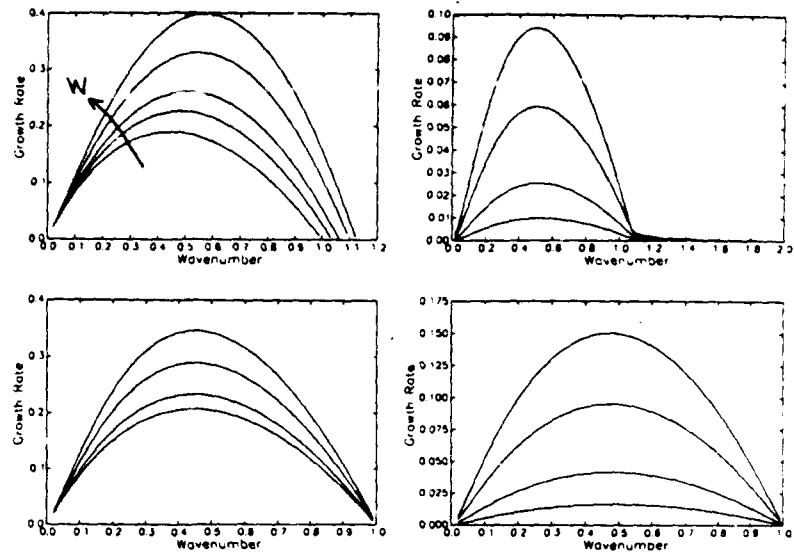
Figure 5a. Growth rate vs. wavenumber of the shear layer (left) and wake (right) modes for the velocity profiles of Fig. 2 and uniform-density profile $T_r = 1$. The top (bottom) row corresponds to $\delta = 1$ ($\delta = 3$).
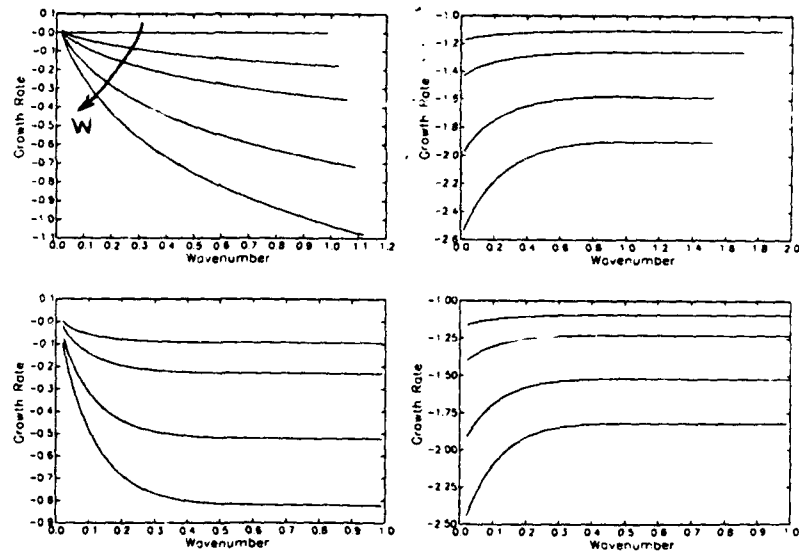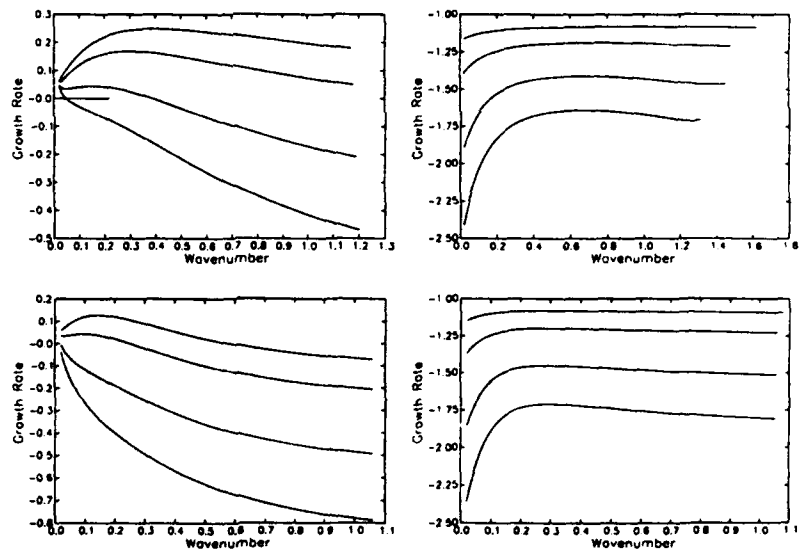

Figure 5b. Phase speed vs. wavenumber for the shear layer (left) and wake (right) modes for the velocity profiles of Fig. 2 and uniform-density profile $T_r = 1$. The top (bottom) row corresponds to $\delta = 1$ ($\delta = 3$).
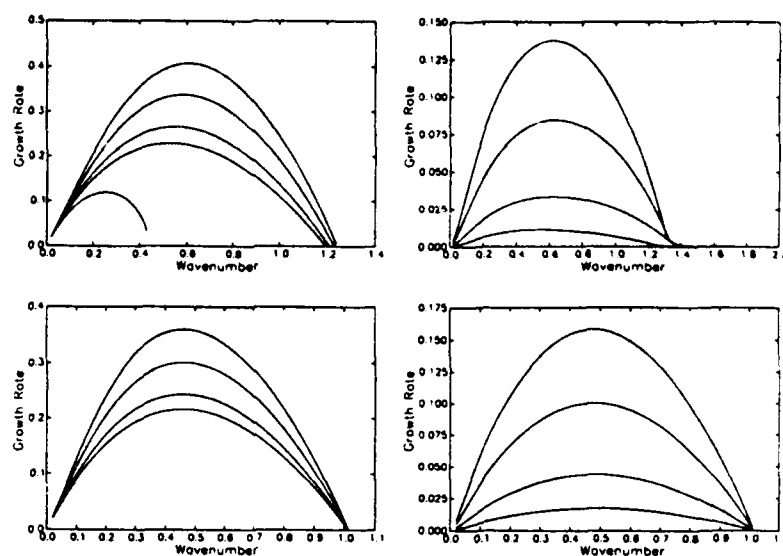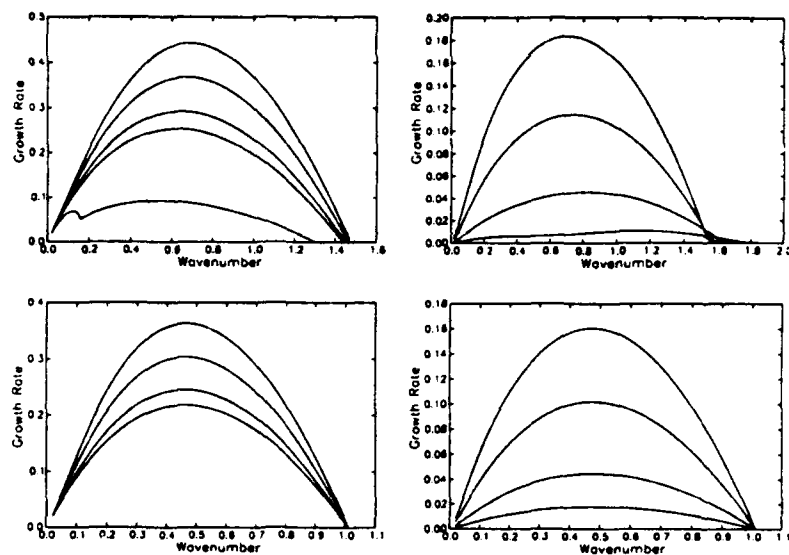
Figure 6a. Growth rate vs. wavenumber of the shear layer (left) and wake (right) modes for the velocity profiles of Fig. 2 and density profile given by $T_r = 2$ and $\sigma = 1$. The top (bottom) row corresponds to $\delta = 1$ ($\delta = 3$).
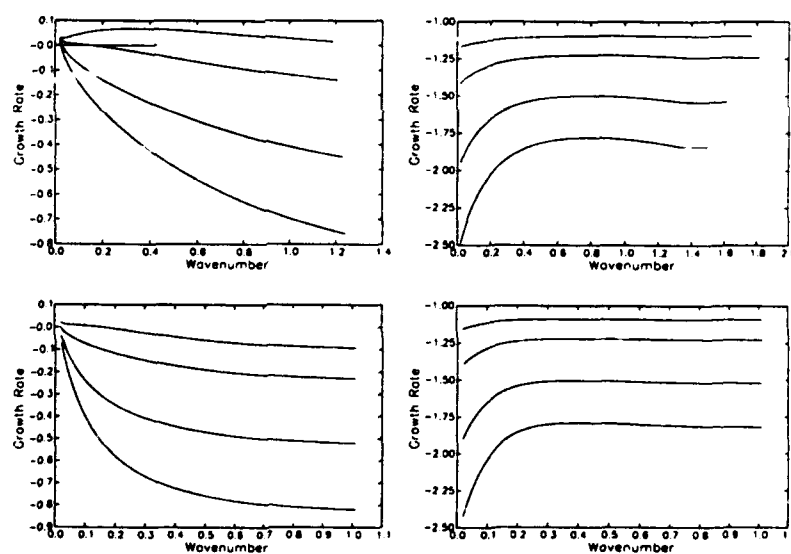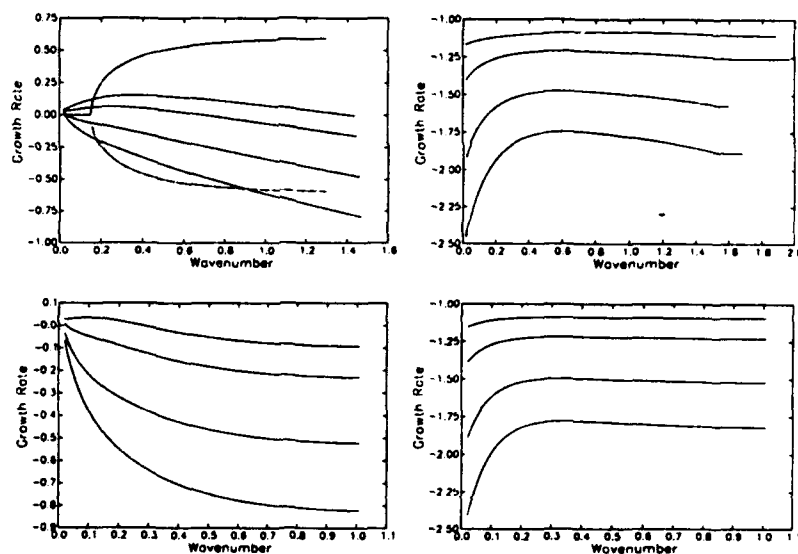

Figure 6b. Phase speed vs. wavenumber of the shear layer (left) and wake (right) modes for the velocity profiles of Fig. 2 and density profile given by $T_r = 2$ and $\sigma = 1$. The top (bottom) row corresponds to $\delta = 1$ ($\delta = 3$).
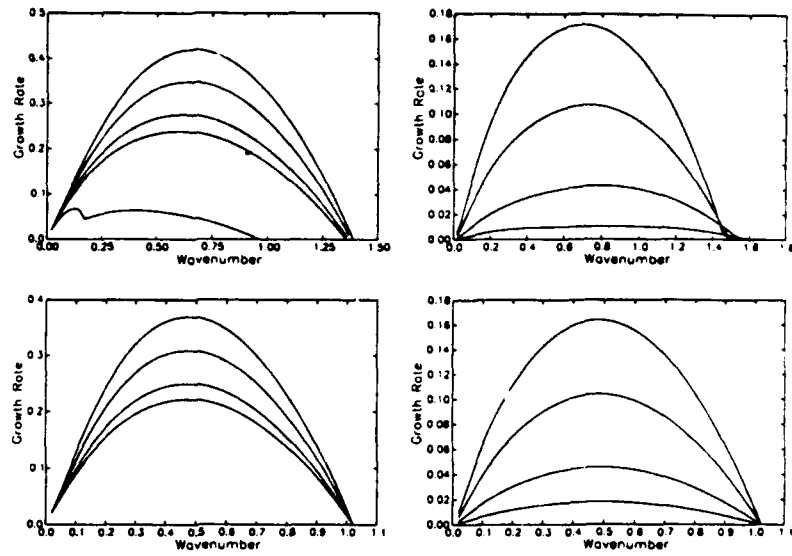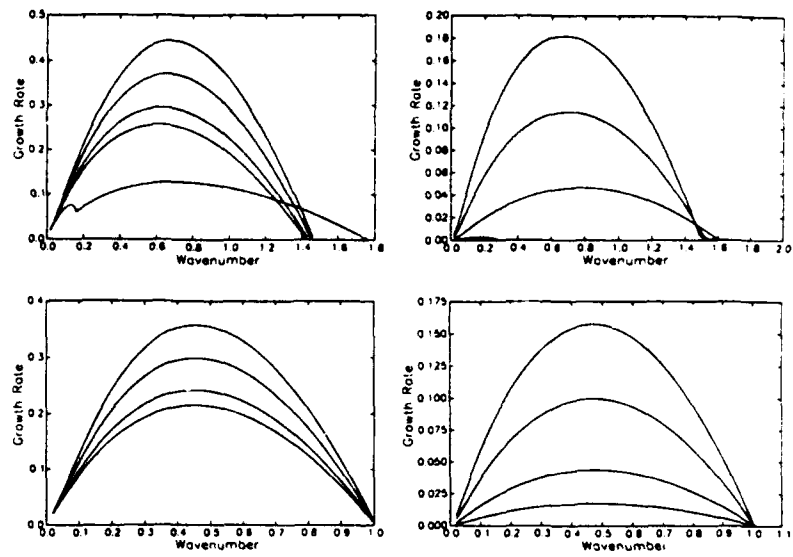
Figure 7a. Growth rate vs. wavenumber of the shear layer (left) and wake (right) modes for the velocity profiles of Fig. 2 and density profile given by $T_r = 4$ and $\sigma = 1$. The top (bottom) row corresponds to $\delta = 1$ ($\delta = 3$).
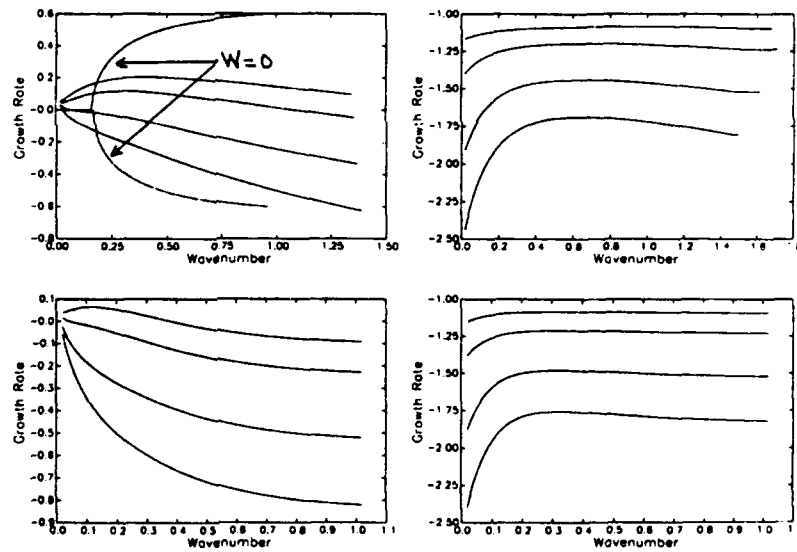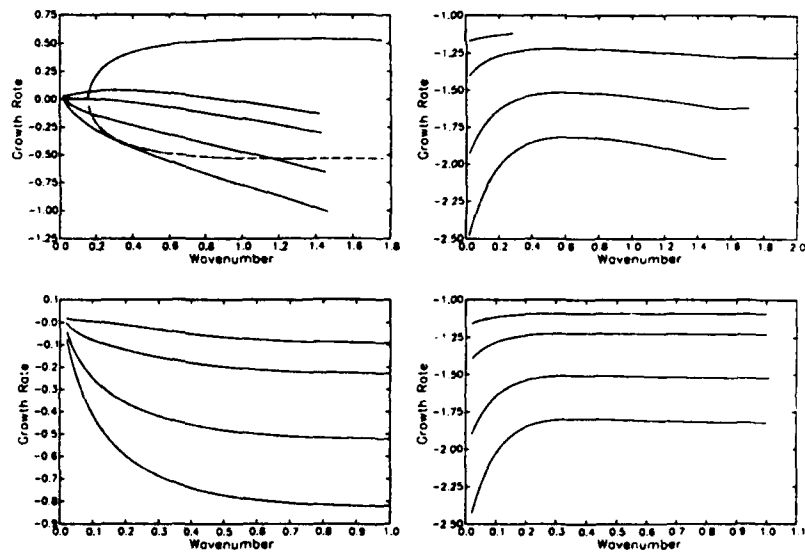

Figure 7b. Phase speed vs. wavenumber of the shear layer (left) and wake (right) modes for the velocity profiles of Fig. 2 and density profile given by $T_r = 4$ and $\sigma = 1$. The top (bottom) row corresponds to $\delta = 1$ ($\delta = 3$).
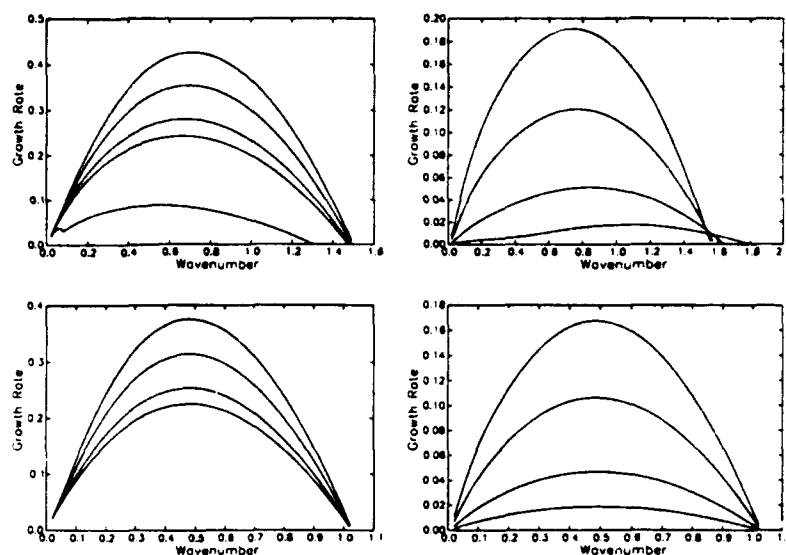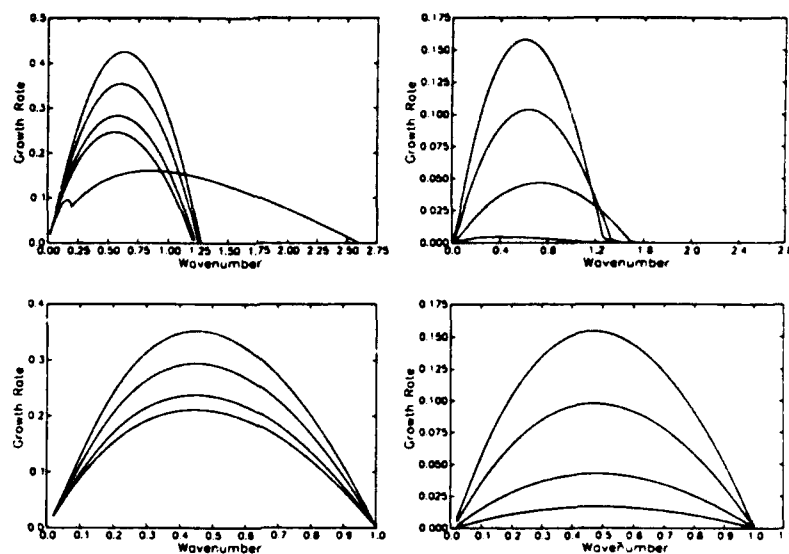
Figure 8a. Growth rate vs. wavenumber of the shear layer (left) and wake (right) modes for the velocity profiles of Fig. 2 and density profile given by $T_r = 8$ and $\sigma = 1$. The top (bottom) row corresponds to $\delta = 1$ ($\delta = 3$).
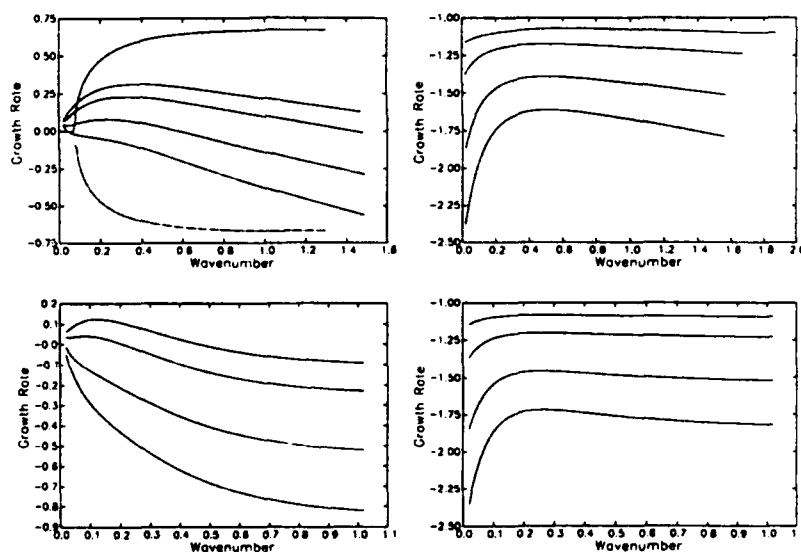
Figure 8b. Phase speed vs. wavenumber of the shear layer (left) and wake (right) modes for the velocity profiles of Fig. 2 and density profile given by $T_r = 8$ and $\sigma = 1$. The top (bottom) row corresponds to $\delta = 1$ ($\delta = 3$).
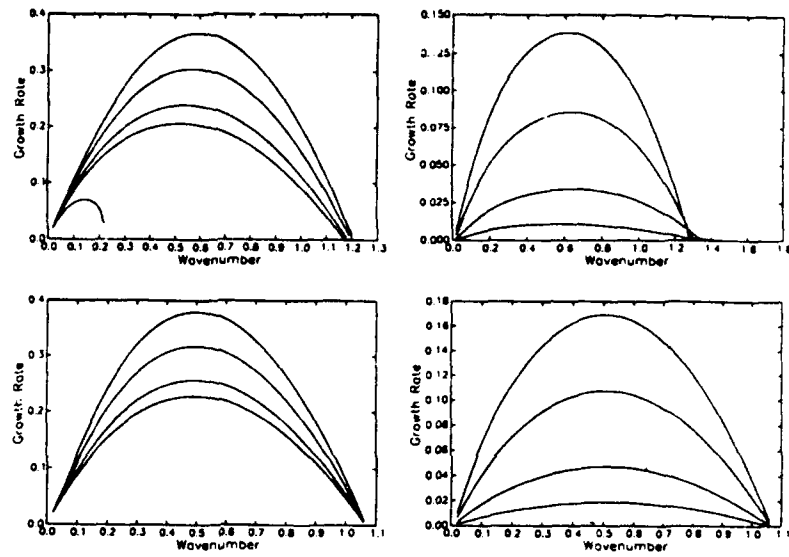
Figure 9a. Growth rate vs. wavenumber of the shear layer (left) and wake (right) modes for the velocity profiles of Fig. 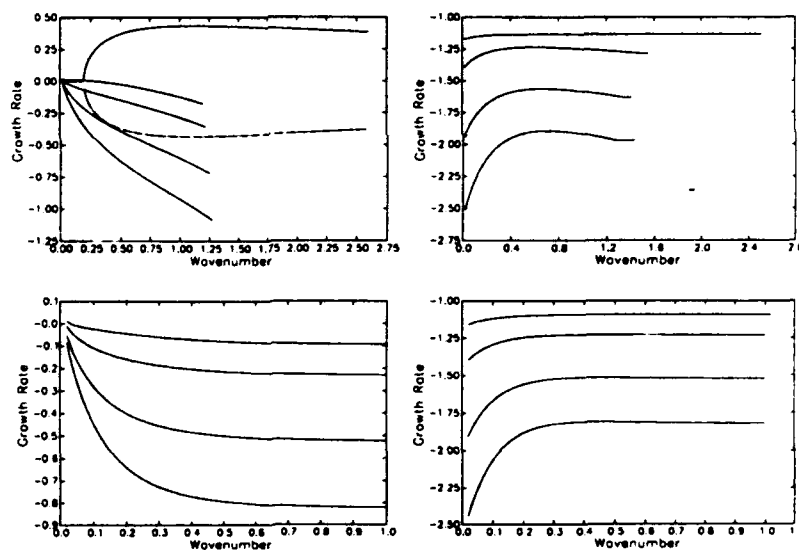2 and density profile given by $T_r = 4$ and $\sigma = 1.5$. The top (bottom) row corresponds to $\delta = 1$ ($\delta = 3$).

Figure 9b. Phase speed vs. wavenumber of the shear layer (left) and wake (right) modes for the velocity profiles of Fig. 2 and density profile given by $T_r = 4$ and $\sigma = 1.5$. The top (bottom) row corresponds to $\delta = 1$ ($\delta = 3$).

Figure 10a. Growth rate vs. wavenumber of the shear layer (left) and wake (right) modes for the velocity profiles of Fig. 2 and density profile given by $T_r = 4$ and $\sigma = 0.75$.

Figure 10b. Phase speed vs. wavenumber of the shear layer (left) and wake (right) modes for the velocity profiles of Fig. 2 and density profile given by $T_r = 4$ and $\sigma = 0.75$.

Figure 11a. Growth rate vs. wavenumber of the shear layer (left) and wake (right) modes for the velocity profiles of Fig. 2 and density profile given by $T_r = 4$ and $\sigma = 0.5$.

Figure 11b. Phase speed vs. wavenumber of the shear layer (left) and wake (right) modes for the velocity profiles of Fig. 2 and density profile given by $T_r = 4$ and $\sigma = 0.5$.

Figure 12a. Growth rate vs. wavenumber of the shear layer (left) and wake (right) modes for the velocity profiles of Fig. 2 and density profile given by $T_r = 4$ and $\sigma = 0.25$.

Figure 12b. Phase speed vs. wavenumber of the shear layer (left) and wake (right) modes for the velocity profiles of Fig. 2 and density profile given by $T_r = 4$ and $\sigma = 0.25$.
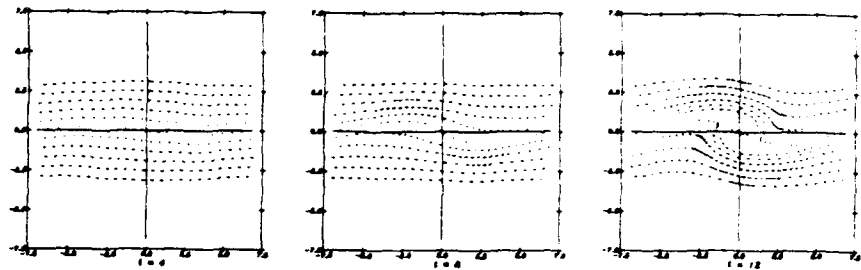
Figure 13. Evolution of the uniform-density shear layer with velocity profile given by $W = \delta = 0$, illustrated in terms of the vortex elements. The plots are generated by drawing the location and instantaneous velocity vector of the elements at $t = 4, 8$, and 12.
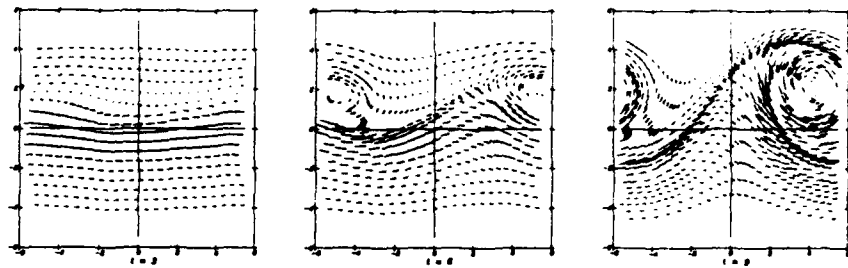
Figure 14. Vortex element representation of the uniform-density shear layer with velocity profile given by $W = 1.2$ and $\delta = 1$, at $t = 3, 6$, and 9. The plots are generated as in Fig. 13.
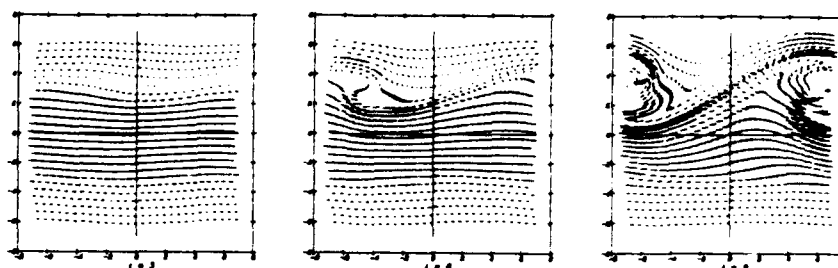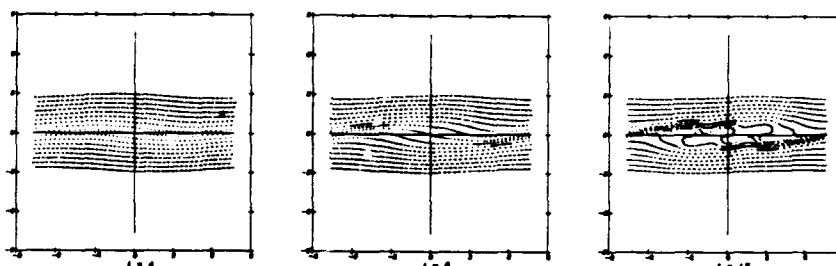
Figure 15. Vortex element representation of the uniform-density shear layer with velocity profile given by $W = 0.82149$ and $\delta = 3$, at $t = 3, 6$, and 9. The plots are generated as in Fig. 13.

Figure 16. Vortex element representation of the shear layer with velocity profile given by $W = \delta = 0$ and density profile having $T_r = 4$ and $\sigma = 1$. The plots are generated as in Fig. 13.
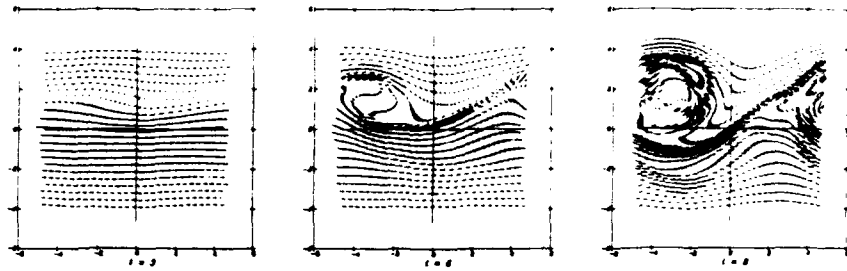
Figure 17. Vortex element representation of the shear layer with velocity profile given by $W = 1.2$ and $\delta = 1$ and density profile having $T_r = 4$ and $\sigma = 1$. The plots are generated as in Fig. 13.
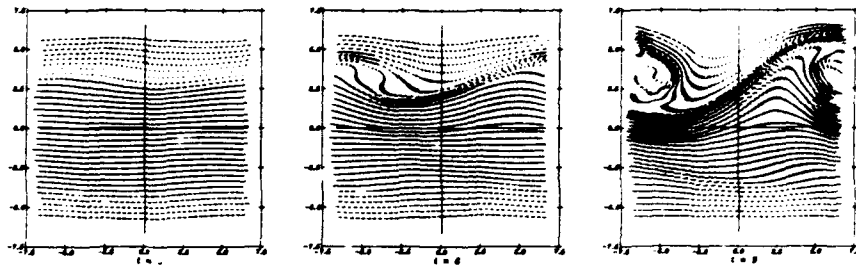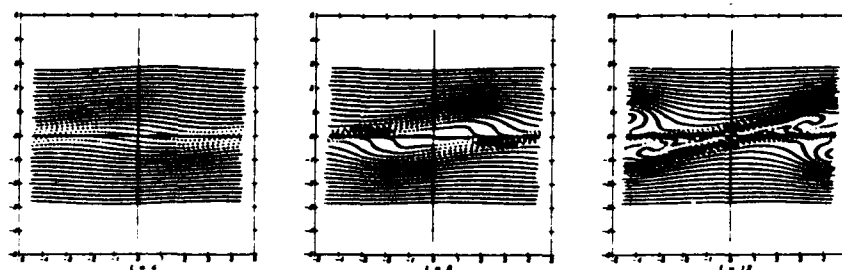

Figure 18. Vortex element representation of the shear layer with velocity profile given by $W = 0.8214$ and $\delta = 3$ and density profile having $T_r = 4$ and $\sigma = 1$. The plots are generated as in Fig. 13.

Figure 19. Vortex element representation of the shear layer with velocity profile given by $W = \delta = 0$ and density profile having $T_r = 4$ and $\sigma = 0.5$. The plots are generated as in Fig. 13.
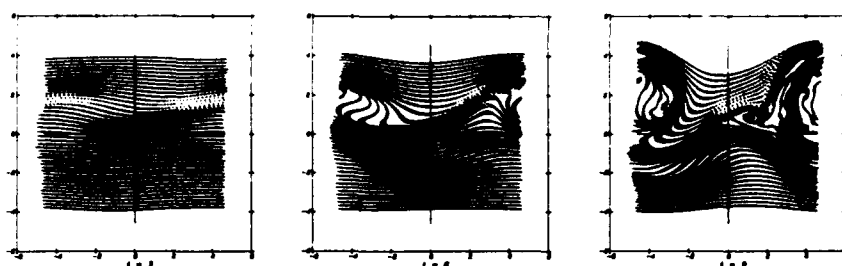

Figure 20. Vortex element representation of the shear layer with velocity profile given by $W = 1.2$ and $\delta = 1$ and density profile having $T_r = 4$ and $\sigma = 0.5$. The plots are generated as in Fig. 13.
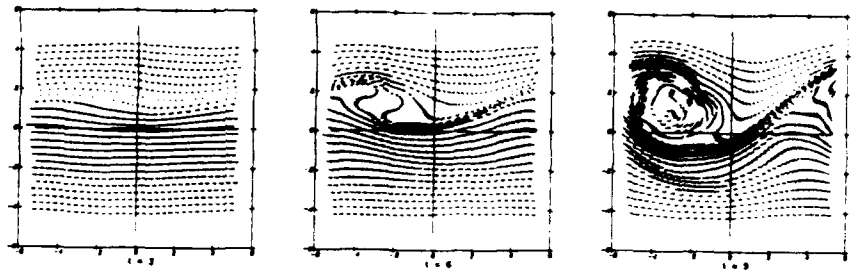
Figure 21. Vortex element representation of the shear layer with velocity profile given by $W = 1.2$ and $\delta = 1$ and density profile having $T_r = 4$ and $\sigma = 1.5$. The plots are generated as in Fig. 13.